Variable-Density Flow in the Subsurface of Oceanic Islands: Physical Experiments and Numerical Modeling

Von der Fakultät für Bauingenieurwesen und Geodäsie

der Gottfried Wilhelm Leibniz Universität Hannover

zur Erlangung des Grades Doktor-Ingenieur

- Dr.-Ing. -

genehmigte Dissertation von

Dipl.-Hydrol. **LEONARD STÖCKL**

geboren am 19.07.1982 in Hamburg

2016

Referent: **Prof. Dr. Thomas Graf**
Korreferentin: **Prof. Dr. Gudrun Massmann**

Tag der Promotion: **11. Mai 2016**

Declaration

I hereby declare that:

- I know the regulations for doctoral candidates at the Faculty of Civil Engineering and Geodetic Science
- I have completed the thesis independently; and any other used materials by others are listed in the references
- I have not paid any monetary benefits for regards to content the dissertation has not been used as a M.Sc. or similar thesis before, and that the thesis or parts of it have not been published before, unless otherwise indicated
- I have not applied before for an exam as doctoral candidate at another academic institution

Hannover, 29.03.2016

Leonard Stöckl

ANICCA*

*Pali language: all of conditioned existence, without exception, is transient, or in a constant state of flux

Acknowledgements

Abstract

Fresh groundwater is a limited and vulnerable resource, but vital for the existence of life. Especially in times of population growth, industrial and agricultural development, and in times of anthropogenic induced climate change, the protection of freshwater resources becomes more and more important. On islands where freshwater is surrounded by saline ocean water, contamination by seawater intrusion, storm surges and anthropogenic overexploitation pose serious hazards. A thorough and holistic understanding of the dynamics of variable-density flow in freshwater lenses is the aim of this study. Only by a proper knowledge of these significant groundwater resources, which in many cases are the only source for drinking water on islands, a sustainable management is possible in the long term.

In this study, physical sand-tank experiments, and numerical, as well as analytical modeling were utilized to study the various aspects of variable-density flow and transport processes in the subsurface of islands. To measure and visualize different groundwater flow dynamics of freshwater lenses, physical experiments on a laboratory scale are most suitable. Especially flow paths, age stratification, and lens formation as well as degradation were investigated here. Using a sand tank, it was possible to physically simulate a cross-section of an infinite strip island: adding different tracer colors with the recharge water made visualization of flow paths as well as the age stratification within the freshwater lens possible. Flow paths in the lens could be demonstrated to remain in contact with the outflow zones at all times during the experiments and age strata became thinner with time and over depth. To validate this approach, model results of the formation and degeneration of the freshwater lens were compared to analytical and numerical results, which were found in good accordance with the experimental findings. Additional experiments show the differences between pumping from a horizontal and a vertical well on the freshwater-saltwater interface. These experiments with identical boundary conditions confirm former presumptions: A horizontal well shows less up-coning of the saltwater-freshwater interface and therefore allows a higher sustainable yield than a vertical well.

Physical, analytical, and numerical modeling was also used to investigate the influence of vertically and horizontally layered aquifers and of variations in recharge on the age stratification, travel times and transient development of freshwater lenses. Four different model cases were examined in detail on a laboratory-scale. Experiments show significant deviations from homogeneous models: The case of a high permeability layer underlying

a layer of lower permeability shows the strongest deviations in the processes investigated here. Water in the more permeable lower layer overtakes water flowing only through the upper layer, causing a bimodal distribution of travel times and a vertical repeating of the age stratification near the coast. The effects of heterogeneities revealed by the physical model experiments are expected to occur also on real islands and have thus to be taken into account when developing conceptual models for the management of their freshwater lenses.

Furthermore, a numerical benchmark for variable-density flow and solute transport in a freshwater lens was developed. This benchmark describes the formation and degradation of a freshwater lens over time, taking the homogeneous sand tank experiment as a basis. An uncertainty analysis yielded the appropriate spatial and temporal discretization. A calibrated parameter set was obtained using the parameter estimation tool PEST. Comparing density-coupled and density-uncoupled results shows that the freshwater-saltwater interface position strongly depends on density differences. Benchmarks adequately representing saltwater intrusion, including realistic features of coastal aquifers or freshwater lenses, are clearly lacking in prevailing literature. A new freshwater lens benchmark was therefore developed, and is demonstrated to be suitable for testing variable-density groundwater models.

The newly developed benchmark of a freshwater lens was subsequently used to conduct a comparison of five different numerical model codes capable of solving the equations for variable-density flow and solute transport. Salinity distributions and directions of groundwater flow are used for comparison in steady-state, as well as the saltwater-freshwater interface propagation and development in transient-state. The results show a high degree of similarity and lie within the accuracy of the previously conducted experimental measurements. However, even though the numerical models are set up using the same conceptual model basis, and are constructed as identical as possible, a direct comparison reveals variations of model outputs resulting from differences in solving methods. Yet, all five numerical model codes are able to adequately reproduce the most relevant variable-density flow processes of the new freshwater lens benchmark.

Keywords: variable-density flow, freshwater lens, physical experiment

Kurzfassung

In Küstengebieten stellt Süßwasser eine limitierte und gefährdete Grundwasserressource dar, die essentiell für die Existenz von Leben ist. Besonders in Zeiten von Bevölkerungswachstum, industrieller und landwirtschaftlicher Entwicklung, sowie in Zeiten des anthropogenen Klimawandels, wird der Schutz von Süßwasserressourcen immer wichtiger. Auf Inseln, wo Süßwasser von salzigem Meerwasser umgeben ist, stellen Kontamination durch Salzwasserintrusion, Überschwemmungen durch Sturmfluten und anthropogene Überbeanspruchung ernst zu nehmende Gefahren dar. Ein gründliches und ganzheitliches Verständnis der Dynamik von dichtegetriebener Strömung in Süßwasserlinsen ist das Ziel dieser Studie. Nur durch die genaue Kenntnis dieser wichtigen Grundwasserressourcen, welche oftmals die einzige Quelle der Trinkwasserversorgung auf Inseln darstellen, ist eine nachhaltige Bewirtschaftung auf lange Sicht möglich.

In dieser Arbeit wurden physikalische Sandtank Experimente sowie numerische und analytische Modelle genutzt, um unterschiedliche Aspekte von Dichteströmungen und Transportprozessen im Untergrund von Inseln zu untersuchen. Um die verschiedenen Grundwasser-Fließdynamiken der Süßwasserlinsen messbar zu machen und zu visualisieren, sind physikalische Experimente im Labormaßstab höchst geeignet. Speziell wurden hier Fließpfade, Altersschichtung sowie Linsenausbildung und Rückbildung untersucht. Mit Hilfe eines Sandkasten-Modells war es möglich den Querschnitt einer idealisierten Insel physikalisch nachzubilden und die Grundwasserfließmuster zu visualisieren: Das Beimischen unterschiedlicher Tracerfarben zum Neubildungswasser ermöglichte die Visualisierung der Fließpfade und der Altersschichtung in der Süßwasserlinse. Es konnte gezeigt werden, dass die Fließpfade in der Linse während der gesamten Experimente in Kontakt mit den Ausflusszonen standen. Die Altersschichtung wurde mit fortschreitender Zeit und über die Tiefe immer dünner. Um diesen Ansatz zu validieren, wurden die Modellergebnisse der Aus- und Rückbildung der Süßwasserlinse mit analytischen und numerischen Ergebnissen verglichen, welche in guter Übereinstimmung mit den experimentellen Ergebnissen standen. Zusätzliche Experimente zeigten Unterschiede zwischen Vertikal- und Horizontalfilterbrunnen beim Pumpen aus einer Süßwasserlinse. Diese Experimente mit identischen Randbedingungen bestätigen frühere Vermutungen: Horizontalfilterbrunnen führen zu einem geringerem Anheben der Salz-Süßwassergrenze und erlauben deshalb eine höhere nachhaltige Entnahme als Vertikalfilterbrunnen.

Physikalische, analytische und numerische Modellierung wurde des Weiteren genutzt, um den Einfluss von vertikal und horizontal geschichteten Aquiferen sowie Variationen

der Grundwasserneubildungsraten auf Altersschichtung, Fließzeiten und transiente Linsenaus- und Rückbildung zu erforschen. Vier unterschiedliche Modellfälle wurden detailliert im Labormaßstab untersucht. Diese Experimente zeigen signifikante Unterschiede zu den homogenen Modellen: Im Fall einer hoch permeablen Schicht unterhalb einer schlechter leitenden Schicht wurden die größten Abweichungen bei den hier untersuchten Prozessen festgestellt. Wasser in der gut leitenden Schicht überholt dabei Wasser, welches nur durch die obere Schicht fließt, was zu einer bimodalen Verteilung der Fließzeiten und einer vertikalen Wiederholung der Altersschichtung in Küstennähe führt. Die im physikalischen Experiment beobachteten Effekte der Heterogenität werden erwartungsgemäß auch auf richtigen Inseln auftreten und müssen daher berücksichtigt werden, wenn Konzeptmodelle für das Management von Süßwasserlinsen erstellt werden.

Des Weiteren wurde ein numerisches Benchmark für variable Dichteströmung und gelösten Stofftransport erstellt. Dieses Benchmark beschreibt die Aus- und Rückbildung einer Süßwasserlinse über die Zeit, wobei das homogene Laborexperiment als Grundlage herangezogen wurde. Mit Hilfe einer Unsicherheitsanalyse wurde eine adäquate räumliche und zeitliche Auflösung ermittelt. Das kalibrierte Parameterset wurde durch Anwendung der Parameter-Schätz Software PEST ermittelt. Der Vergleich von dichtegekoppelten und dichteentkoppelten Modellergebnissen zeigt, dass die Position der Salz-Süßwasser Grenzschicht deutlich von den Dichteunterschieden abhängt. Salzwasserintrusion repräsentierende, vollwertige Benchmarks, welche realistische Eigenschaften von Küstenaquiferen oder Süßwasserlinsen abbilden, fehlen in der vorherrschenden Literatur. Deshalb wurde ein neues Süßwasserlinsen-Benchmark entwickelt bei dem gezeigt wird, dass es geeignet für das Testen von Grundwassermodellen mit variabler Dichteströmung ist.

Dieses neu entwickelte Benchmark wurde anschließend genutzt, um einen Modellvergleich zwischen fünf verschiedenen numerischen Codes durchzuführen, welche alle Gleichungen von variabler Dichte und gelöstem Stofftransport lösen können. Salzverteilungen und Grundwasserfließrichtungen wurden für den Vergleich im stationären, sowie die Ausbreitung und Entwicklung der Salz-Süßwasser Grenzschicht im transienten Zustand herangezogen. Die Ergebnisse zeigen ein hohes Maß an Übereinstimmung und liegen innerhalb der Genauigkeit der zuvor durchgeführten experimentellen Messungen. Obwohl die numerischen Modelle auf gleicher konzeptioneller Basis und so identisch wie möglich konstruiert wurden, zeigt ein direkter Vergleich Unterschiede in den Modellergebnissen, welche durch unterschiedliche Lösungsmethoden entstehen. Dennoch, alle fünf numerischen Modellcodes sind in der Lage, die relevanten Prozesse variabler Dichteströmung des neuen Süßwasserlinsen-Benchmarks adäquat zu reproduzieren.

Schlagworte: dichteabhängige Strömung, Süßwasserlinse, physikalisches Experiment

Contents

List of Figures

List of Tables

Nomenclature

α_l Longitudinal dispersivity [L]

α_t Transverse dispersivity [L]

β Relative densities (or Ghyben-Herzberg factor) [-]

B   Width of the dune belt [L]

c Relative concentration [-]

d   Diameter [L]

D   Hydrodynamic dispersion tensor [L^2T^{-1}]

D_m Molecular diffusion coefficient [L^2T^{-1}]

E Nash-Sutcliff efficiency [-]

f_1 Correction factor for aquifer anisotropy [-]

f_2 Correction factor for numerical model [-]

g Gravitational constant [LT^{-2}]

h Maximum freshwater lens thickness [L]

h_0 Equivalent head [L]

I   Identity matrix [-]

K   Hydraulic conductivity [LT^{-1}]

K_0 Equivalent hydraulic conductivity [LT^{-1}]

L   Half width of island [L]

ne Effective porosity [-]

ρ Fluid density [ML^{-3}]

ρ_0 Reference density [ML^{-3}]

ρ_s Density of saltwater [ML^{-3}]

ρ_f Density of freshwater [ML^{-3}]

$\Delta\rho$ Density difference between salt- and freshwater [ML^{-3}]

p   Fluid pressure [$ML^{-1}T^{-2}$]

q   Darcy flux $[LT^{-1}]$

R   Recharge rate $[LT^{-1}]$

S_s Specific storage $[L^{-1}]$

t   Time $[T]$

τ Tortuosity $[-]$

μ Dynamic viscosity $[ML^{-1}T^{-1}]$

x Horizontal distance from the island center $[L]$

x_i Initial position on the island $[L]$

x_z Final flow path position on the island $[L]$

z   Elevation above datum $[L]$

z_o^t Observed depth $[m]$

z_m^t Modeled or simulated depth $[m]$

$\bar{z}_o$ Mean depth $[m]$.

Z   Depth of the aquifer base $[L]$

Z_t Depth to interface at time $t = t$ $[L]$

Z_∞ Depth to interface at time $t = \infty$ $[L]$

∇ Nabla operator $[L^{-1}]$

1 Introduction

1.1 Motivation

In a globalized and rapidly changing world and by means of ancient wisdom and high-end technology, it becomes more and more apparent that change is the dominant state of nature. This universal law seems to be true on every scale in space and time, e.g. for the macroscopic buildup and melting of glaciers on geological time scales, as well as for the rapid microscopic interchange of protons between water molecules. Groundwater flow is not an exception; this becomes apparent through declining water tables or the salinization of coastal aquifers in many parts of the world today.

In the case of freshwater lenses on islands, however, one may assume for simplicity an equilibrium between the salt- and the freshwater, i.e. a stationary position of the freshwater-saltwater interface, as done by Badon-Ghyben (1888) and Herzberg (1901). This means that under steady-state conditions, a freshwater lens, recharged by infiltrating precipitation, penetrates an island aquifer to a certain depth by displacement of the surrounding saltwater. When taking a closer look on such a system, it becomes clear that the equilibrium between fresh- and saltwater is fragile and dynamically reacts to changes in its boundary conditions. Natural or anthropogenic induced influences will eventually lead to an alteration of the freshwater lens and of the amount of available freshwater, e.g. by climate change or groundwater abstraction.

In the short term, that is in the range of years to decades, management strategies may be applied to optimize freshwater withdrawal and ensure sustainability. As freshwater lenses are in fragile equilibrium with the surrounding saltwater, flow processes of such systems must be well understood in steady-state and eventually in transience, in order to be managed wisely. To analyze, investigate, and predict dynamics of fresh- and saltwater interaction, numerical groundwater models are commonly used. In contrast to analytical models, numerical groundwater models are able to simulate highly complex geometries. An advantage compared to physical model equivalents is a much quicker attainment of results by fast runtimes and the possibility of easily performed model adoptions.

Besides the evident advantages of numerical modeling tools, it is important to note that numerical modeling software is subject to change itself: permanent development and improvement and the implementation of new features is inevitable. Changes in the code, however, might lead to unexpected interdependencies or coding errors, possibly leading to incorrect calculations. It is thus necessary to define test cases, i.e. benchmarks, proving the

reliability of different modeling tools. This becomes especially important for highly complex or unsymmetrical systems, e.g. for variable-density flow and solute transport calculation software.

Awareness raising of the aforementioned changes, as well as the ability to adapt to and deal with the results and challenges of saltwater intrusion are among the most important tasks for an integrated water resource management. Regarding the special cases of freshwater lenses which are vulnerable to saltwater intrusion, an ever-increasing number of publications reflects the importance and increased interest in this field of research (as summarized by e.g. Robins (2013) and Werner et al. (2013) and references therein). Today, around 40% of the world´s population live close to the oceanic coast and around 10% live on islands (Crossland et al., 2005; Crocombe, 2008). Increasing stress on freshwater sources due to population growth as well as climate change, and augmented industrial and agricultural water demand endanger water supply in many parts of the world (e.g. Oude Essink, 1996; Maas, 2007; Oude Essink et al., 2010). On various islands and in coastal zones, excessive abstraction has lead to seawater encroachment and up-coning (White et al., 2007; Mondal et al., 2008; Custodio, 2010). Overuse may provoke intrusion of saltwater and damage freshwater aquifers for decades. This highlights the importance of a wise management of these scarce resources. In fact, freshwater aquifer systems of small oceanic islands are considered to be among the most vulnerable in the world and often are the only resource for drinking water supply (White and Falkland, 2009).

To ensure a sustainable management and to be able to predict the consequences of the previously mentioned changes on freshwater lenses is the motivation for this study. It seems indispensable to develop a holistic process understanding of these limited, but vital freshwater resources. Using physical model experiments and developing and applying new methods for the investigations of variable-density flow and solute transport are performed in this study.

1.2 State of research

1.2.1 Freshwater lens investigations

Literature on the interaction of freshwater and saline water in coastal zones and on oceanic islands is abundant. A good overview can be found e.g. in Cooper et al. (1964), Bear et al. (2010), and Werner et al. (2013). Badon-Ghyben and Herzberg independently from each other developed the so called Ghyben-Herzberg principle back in 1888 resp. 1901. This principle states that the depth of a steady-state freshwater-saltwater interface at a certain location in an aquifer can be calculated by the product of the density-ratio (between fresh- and saltwater)

and the freshwater head at that location (Badon-Ghyben, 1888; Herzberg, 1901). Since then, more and more sophisticated analytical models were, and are still being developed to describe variable-density flow of freshwater lenses (e.g. Fetter, 1972; van der Veer, 1977; Vacher, 1988; Vacher et al., 1990; Stuyfzand and Bruggeman, 1994; Chesnaux and Allen, 2008; Greskowiak et al., 2013; Strack and Ausk, 2015).

During the last decade, a large number of field studies on islands´ freshwater lenses was conducted, reflecting the broad scientific interest in this topic (e.g. Schneider and Kruse, 2005; Hodgkinson et al., 2007; White and Falkland, 2009; Comte et al., 2010; Rozell and Wong, 2010; Terry and Falkland, 2010; Bailey et al., 2012; Röper et al., 2012; Sulzbacher et al., 2012; Ataie-Ashtiani et al., 2013; Mahmoodzadeh et al., 2014; Holding and Allen, 2015b). Groundwater analyses help to understand local groundwater situations in a certain study area. Geophysical methods, mainly geoelectrical and electromagnetic techniques, both airborne and from the ground, allow delineating the distribution of salt- and freshwater and locating the interface that separates both (e.g. Tronicke et al., 1999; Barrett et al., 2002; Siemon et al., 2009). However, most field studies are site-specific and results are thus not easily transferable to different locations.

Synthetic and systematic studies overcome this restriction and were conducted by e.g. Vacher (1988), who analytically demonstrates dependencies of geology and recharge rates on the freshwater-saltwater interface position. Schneider and Kruse (2003) compared different controls (i.e. geology, terrain, and sea level) on freshwater lens morphology. Morgan and Werner (2014) analytically developed seawater intrusion vulnerability indicators for freshwater lenses in head and flux controlled strip islands. Holding and Allen (2015a) studied the responses of freshwater lenses to wave over-wash, representing different hydrogeological settings in their synthetic numerical models. Still, to date no systematic investigation was conducted on the flow processes (e.g. flow paths, travel times, or groundwater ages) within freshwater lenses.

Laboratory experiments offer the advantage of a direct visualization and measurement of processes in a controlled environment, which are not easily observable in nature, e.g. the groundwater flow pattern and exchange processes between fresh- and saltwater. Numerical models can be used to investigate and predict phenomena related to saltwater-freshwater interaction further, supporting or extending the possibilities of physical experiments. This study aims to combine these two approaches with the additional application of existing analytical solutions.

The earliest visualisations using physical experiments date back a hundred years ago, when Pennink (1915) used water and ink to colour flow paths. In the case of variable-density effects, Pennink (1915) simulated groundwater up-coning by using water and milk. Today, physical experiments in groundwater hydrology are still commonly in use to investigate density

dependent flow processes and to benchmark numerical models. Recent physical model experiments investigating variably-density flow in coastal areas were conducted by Goswami and Clement (2007) - sea level rise, Abarca and Clement (2009) - mixing zone, Werner et al. (2009) and Jakovovic et al. (2011) - saltwater up-coning, Luyun et al. (2011) - seawater intrusion barriers, Kuan et al. (2012) - tidal fluctuations, Chang and Clement (2013) - transport processes within a saltwater wedge, Mehdizadeh et al. (2014) - vertical leakage in layered aquifers, Robinson et al. (2015) - mixing zone and wedge-toe length. Until now, freshwater lens dynamics under islands were not investigated using physical experiments.

When pumping water from a freshwater lens, a cone of depression develops and the height of the freshwater column above the interface decreases. This can lead to up-coning and in the worst case to intrusion of saltwater into the well (Dagan and Bear, 1968; Schmork and Mercado, 1969; Gupta and Gaikwad, 1987; Zhou et al., 2005). Horizontal wells (radial collector wells), might distribute the drawdown more evenly and may thus be an alternative to vertical wells. Here, for the first time, a direct comparison of the effects of saltwater up-coning from a horizontal versus a vertical well underneath islands was conducted.

The influence of geological heterogeneity and spatially variable groundwater recharge on the geometry of freshwater lenses has been addressed by, e.g. Vacher (1988), Schneider and Kruse (2003), Bailey et al. (2009), Bailey et al. (2012), Rozell and Wong (2010), and Ketabchi et al. (2014). It is well known that such heterogeneities influence the shape of freshwater lenses. However, little is known about their effects on flow dynamics within the freshwater lenses. The age stratification or vertical distribution of groundwater ages is a very useful tool to obtain recharge rates (Scanlon et al., 2002; Allen et al., 2014; Houben et al., 2014a), which is a fundamental parameter for sustainable water resources management. Ages can also be used for the calibration of groundwater flow models (e.g. Voss and Wood, 1994; Sanford, 2011; Zuber et al., 2011; Post et al., 2013). The few field studies investigating age stratification (e.g. Stuyfzand, 1993; Röper et al., 2012; Houben et al., 2014a), however, show that the homogeneous models mentioned above have problems emulating the age stratification encountered in the field.

How fast freshwater lenses respond to changes in recharge (and groundwater extraction) is a measure of their resilience. The transient interface propagation may be used as a proxy for this. The rationale is that islands with fast lens formation also suffer from fast degradation. Especially shallow and "juvenile" lenses on actively growing or artificial islands are very sensitive to temporal variations of groundwater recharge (Röper et al., 2013 and van Ginkel, 2015). Several studies exist, most of them numerical, which investigate the influence of a changing climate on lens geometry (Maas, 2007; Bailey et al., 2009; Rozell and Wong, 2010; Sulzbacher et al., 2012; Mahmoodzadeh et al., 2014; Holding and Allen, 2015b; Lemieux et

4

al., 2015). In this study, times of lens formation are observed in the controlled environment of physical model experiments, addressing different geometries typical for real world islands.

1.2.2 Numerical variable-density benchmarking

Variations of water density affect groundwater flow and may induce variable-density flow. This is a common phenomenon worldwide and thus of major importance in many different fields of application. Examples include saltwater intrusion, inland salinity, geothermal energy production, and hazardous waste disposal. Density variations have thus to be considered when investigating saltwater intrusion, saltwater up-coning, or the position of the freshwater-saltwater interface of freshwater lenses under islands or in coastal aquifers. Without considering water density variations, sustainable water management as well as reliable predictions about the impacts on freshwater resources are not possible. A review of the importance of variable-density flow and saltwater intrusion is given by Simmons (2005) and Werner et al. (2013).

Complex situations, e.g. non-trivial geometries or heterogeneity of hydro-geological properties may be assessed with the help of groundwater flow and solute transport simulation software. However, these model codes themselves are affected by modifications: permanent development and changes make benchmarks necessary in order to ensure the correct implementation of new features or to test newly developed model codes. In addition, as the development of different model codes are done by different researchers, benchmarks can be used to compare the behaviour of different model codes, thus ensuring comparability among the simulation results.

A broad variety of numerical benchmark definitions for variable-density flow exists (Kolditz et al., 2015). Only the application of benchmarks guarantees that a software adequately reproduces the physics as observed in nature, and that models are capable of reproducing particular real-world problems. However, only a limited number of benchmarks are physically based (e.g. Johannsen et al., 2002; Simmons et al., 2002; Thorenz et al., 2002; Oswald and Kinzelbach, 2004). A valuable benchmark is characterized after Diersch (2014):

- a benchmark should have a real, physically and/or physically relevant background
- it should be mathematically correct, definite and well-posed
- the benchmark solutions should be predictable (non-random), both in a physical and mathematical sense
- ideally the benchmark should have a physical model equivalent, for which qualified laboratory data are available

To date, the Henry (1964b) saltwater intrusion problem in a vertically oriented rectangular domain is the only benchmark problem explicitly dealing with saltwater intrusion. A constant saltwater concentration and constant-head boundary condition at the left boundary (outflow to sea), and a constant freshwater concentration and constant-flux boundary condition at the right boundary (inflow from aquifer) lead to the development of a saltwater wedge that intrudes into the freshwater aquifer. The relatively thick transition zone in the Henry (1964b) problem is simulated using an unrealistically high diffusion coefficient. Alternatively, Abarca et al. (2007) offered a dispersive rather than diffusive Henry problem, which does not have an analytical solution. Goswami and Clement (2007) conducted further physical experiments of variations of the Henry (1964b) problem, introducing the transient behavior between freshwater and saltwater under intruding-wedge and receding-wedge conditions as a new benchmark. Potential vulnerability of coastal freshwater aquifers by seawater intrusion is and remains an important and unresolved issue that still requires further research and understanding (e.g. Miller and Gray, 2002; Morgan et al., 2013; Werner et al., 2013). While some realistic physical features are regarded in the Henry saltwater intrusion problem (e.g. realistic head and concentration difference between the recharging freshwater and the ocean water), others are disregarded (e.g. freshwater recharge, sloping beach face, realistic seepage face generation). More importantly, the Henry problem suffers from some mathematical shortcomings outlined by Simpson and Clement (2003).

Simpson and Clement (2003) questioned the worthiness of the Henry problem. They showed that density-uncoupled and density-coupled solutions of the Henry problem yield similar results. The uncoupled solution neglected density differences in the governing equations, and only accounted for density differences in the constant-head boundary condition. The coupled solution, however, fully accounted for density differences in all governing equations and in the constant-head boundary condition. The highly similar results demonstrated that simulated flow patterns are largely dictated by the applied boundary condition and not by physical density-dependent effects. Simpson and Clement (2004) improved the worthiness of the Henry problem by lowering the recharge rate, therefore increasing the model sensitivity to density effects. However, the improved coupled and uncoupled results by Simpson and Clement (2004) still show a high degree of similarity. More recently, Goswami and Clement (2007) provided experimental data sets of the steady-state and transient intruding and receding saltwater wedge of the Henry problem. It can therefore be concluded that a rigorous benchmark of the flow dynamics in coastal aquifers and under islands is needed. A new numerical benchmark of a freshwater lens is thus developed in this thesis.

In groundwater hydrology, benchmarks are widely applied to test numerical model codes. E.g. Maxwell et al. (2014) conducted a comparison of different codes for the simulation of coupled surface- and groundwater flow. Such comparison help detecting differences, weaknesses and

6

conformities of the different codes and give the user evidence for a proper code selection in respect to a specific topic to be dealt with. No direct comparison of different groundwater flow and solute transport model codes was conducted so far, exploring their specific behaviour to saltwater intrusion based on well defined and physically based freshwater lens benchmark.

1.3 Structure of thesis

The document is divided into two parts:

I   Experimental laboratory work: homogeneous and heterogeneous set-ups

II   Numerical benchmarking and model code comparison

Part one describes the experimental work, where freshwater lenses with homogeneous (Chapter 2) and heterogeneous (Chapter 3) set-ups are investigated in the controlled environment of the laboratory. In part two, the homogeneous experiment is taken as a physical base case for a numerical benchmark definition (Chapter 4). A subsequent model comparison is performed using five different numerical codes capable of solving the fluid and transport equation (Chapter 5).

Peer reviewed journal papers arising from this thesis are as follows:

Stoeckl, L., Houben, G., 2012. 'Flow dynamics and age stratification of freshwater lenses: Experiments and modeling'. In: *Journal of Hydrology*, 458–459(0): 9-15.

Dose, E., Stoeckl, L., Houben, G.J., Vacher, L.H., Vassolo, S., Dietrich, J., Himmelsbach, T., 2014. 'Experiments and modeling of freshwater lenses in layered aquifers: Steady state interface geometry'. In: *Journal of Hydrology*, 509: 621–630.

Stoeckl, L., Houben, G.J., Dose, E.J., 2015. 'Experiments and modeling of flow processes in freshwater lenses in layered island aquifers: Analysis of age stratification, travel times and interface propagation'. In: *Journal of Hydrology*, 529, Part 1: 159-168.

Stoeckl, L., Walther, M., Graf, T. (2016). 'A new numerical benchmark of a freshwater lens'. In: *Water Resources Research* 52(4): 2474–2489.

Stoeckl, L., Walther, M., Schneider, A., Yang, J., Graf, T. (in prep.). 'Numerical code comparison using the new variable-density flow and solute transport benchmark of a freshwater lens'

1.4 Objectives

The objective of this study is to identify and investigate dominant flow processes in the subsurface of oceanic islands, which must be understood for a sustainable management of freshwater lenses. As flow dynamics in real-world freshwater lenses are rarely directly measureable, the objective here is to use model equivalents for visualization, e.g. by physical experiments, and to compare them to analytical and numerical model results.

Except for the case-specific analytical solutions by Vacher et al. (1990) and Chesnaux and Allen (2008), information on internal flow dynamics inside freshwater lenses under islands is scarce. This thesis aims at filling that gap: a series of physical model experiments investigates the time-dependent formation and degradation of freshwater lenses, as well as freshwater flow paths, travel times, and age stratification (Chapter 2, Stoeckl and Houben, 2012). The improved process understanding attained by this study will help to adequately delineate groundwater protection zones on islands, to predict the progression of contaminants along flow paths, to use freshwater lenses as a climate archive (Houben et al., 2014a), and to manage more sustainably groundwater abstraction on islands, where drinking water in general is limited.

The objective of the physical experiments conducted with layered aquifers is to a) validate the analytical approach by Vacher and Ayers (1980) by measuring the steady-state interface position (Appendix, Dose et al., 2014), and b) analyze similarities and deviations of freshwater flow pattern within these differently shaped lenses (Chapter 3, Stoeckl et al., 2015). These experiments bridge the gap between models for homogeneous aquifers, see Vogel (1967) and Stoeckl and Houben (2012), and the complexities of real-world settings, by addressing geological heterogeneity and spatial variation of recharge rates using the mentioned advantages of sand tank experiments. As a result, templates compiled for different island settings can be used in the future to develop conceptual models when conducting field studies on islands, managing their groundwater recourses, or conducting specific numerical model simulations of freshwater lenses (Chapter 3, Stoeckl et al., 2015).

A second major objective of this thesis is the development of a robust and physically based numerical benchmark for variable-density flow and solute transport (Chapter 4, Stoeckl et al., 2016). To make this benchmark useful and applicable, an exact definition is required. Thus, a precise definition as well as an uncertainty study, a convergence study, and a worthiness study are conducted and presented here. This study offers an alternative to the Henry (1964b) saltwater intrusion problem by introducing a new numerical benchmark of a physical freshwater lens experiment of an idealized infinite-strip island conducted by Stoeckl and Houben (2012).

Numerical models capable of simulating groundwater flow and solute transport are widely applied and get constantly improved. To ensure the correct implementation of new features into a code, benchmarks are necessary to ensure correct performance. As mentioned before, the worthiness of the widely used Henry (1964b) saltwater intrusion problem is questionable. A newly developed benchmark can fill this gap by satisfying essential requirements, i.e. demonstrating its worthiness, having a physical model equivalent and a real and relevant background, and being predictable and mathematically correct (Diersch, 2005). Such a benchmark will not only help software developers to ensure that advancements are correctly implemented, but also enable users to compare different numerical codes (Chapter 5, Model Comparison).

The two main working hypotheses discussed by this thesis are:

I   Visualizations and measurements can be conducted by specially designed laboratory experiments, which will improve the general process understanding of the dynamics of variable-density flow and solute transport in the subsurface of oceanic islands.

II   A new numerical benchmark can be developed, which will fill the gap of a missing variable-density flow and solute transport problem representing real world features like freshwater recharge from the top and sloped boundary conditions.

2 Physical experiments on freshwater lens dynamics: the homogeneous case

The work of this chapter has been published as: Stoeckl, L., Houben, G., 2012. 'Flow dynamics and age stratification of freshwater lenses: Experiments and modeling'. In: *Journal of Hydrology*, 458–459(0): 9-15.

2.1 Experimental methods and materials

2.1.1 Physical model

An acrylic glass box of 2.0 m in length, 0.5 m in height and 0.05 m in thickness was used for the for the experiments. A cross section of an infinite strip island was simulated by filling coarse sand into the box, forming a homogeneous sand cone (Figure 2-1). The sand was slightly compacted by palpitation. The grain size distribution (sieve curve) of the filter gravel ($d \approx 0.7$–1.2 mm) used in all experiments was optically determined using a Camsizer by Retsch Technology, Germany, with a measurement range between 30 μm and 30 mm. Hydraulic conductivity was determined applying the empirical formula by Beyer and Schweiger (1969) on the measured sieve curves, assuming medium compaction. Together with additional DARCY conductivity tests, a mean hydraulic conductivity K of 4.5×10^{-3} m s^{-1} was obtained. According to Beyer and Schweiger (1969) total porosity was determined to be 0.39.
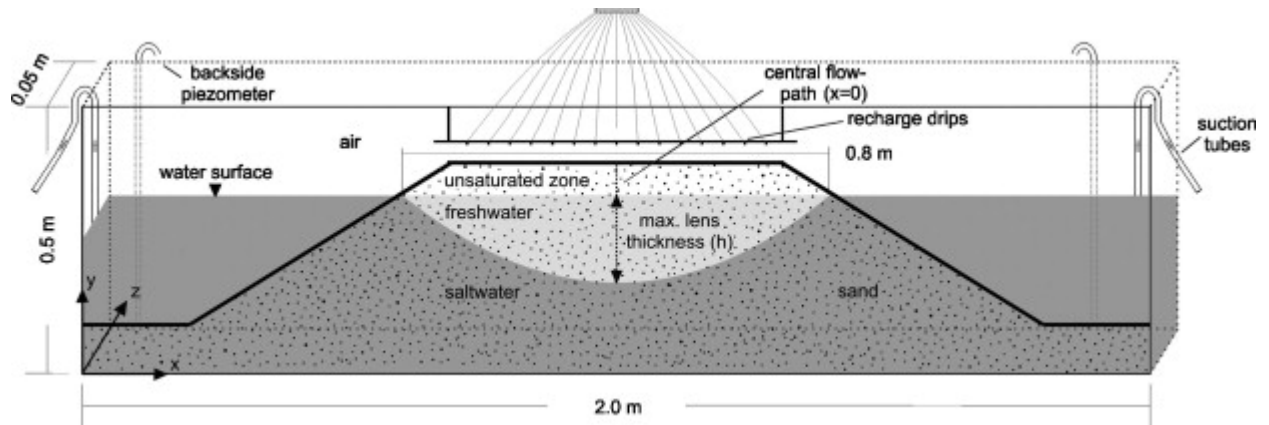
Figure 2-1: Sketch of the sand box model used for the physical experiments.

Density of water was determined using a density meter DMA 38 by Anton Paar, Austria. Freshwater density was determined to be 997.4 kg m^{-3}. Saltwater (uncolored) with a density of 1021.2 kg m^{-3}, simulating ocean water, was injected, saturating the sand from the bottom. Prior to injection, the saltwater was degassed to prevent air from being entrapped in pores. The temperature of the salt and freshwater as well as the air temperature in the laboratory was monitored and kept stable throughout the experiment (23 °C).

To simulate recharge, fifteen individual freshwater drips were installed above the sand cone, connected to a BVP peristaltic pump by Ismatec, Wertheim, Germany (Figure 2-1). For visualization, the tracer dyes uranine (yellow), eosine (red) and indigotine (blue), respectively, were added to the freshwater at a concentration of 0.3 g l^{-1}. It was assumed that effects of the tracers on density and viscosity of the fluid can be neglected.

Freshwater discharging into the "ocean" formed a thin layer on top of the free saltwater surface. It was continuously skimmed from the left and right boundary of the model by a peristaltic pump with a rate equaling total freshwater recharge. This prevents dilution of saltwater and maintains a constant water level. Slight mixing due to diffusion and dispersion was visible. However, by measuring saltwater conductivity it could be shown that this had no significant effect on saltwater densities in the open reservoir. Small fluctuations in the water table did not cause any significant deviations. The skimming might be replaced in future experiments by adding saltwater reservoirs to both sides of the model, similar to the set-up used by Zhang et al. (2002) and Luyun et al. (2011).

The specific electrical conductivity of water pumped from the model wells was continuously measured using a TetraCon DU/T flowthrough conductivity probe and a MultiLine P4 conductivity meter, both by WTW GmbH, Weilheim, Germany. Values were stored (5 s interval) on a laptop using the software MultiLab Pilot (WTW). The electric conductivity of the freshwater (tap water plus tracer) was 590 µS cm^{-1}. For a detailed optical analysis, all experiments were filmed at an interval of one picture per second (Sony XD CAM-EX). The

individual experiments lasted several hours. The films were converted to videos of around 15 or 20 s duration using fast motion mode. Travel times and interface propagation were read off manually from the videos by following the movement of color fronts through the system over time using a centimeter scale placed at the center of the island.

When interpreting the physical models some general restrictions have to be taken into account:

(1) The ratio of the freshwater lens thickness to the width of the island is rather high in the physical model, around 0.15 m/0.8 m ≈ 1:5. Vacher (1988) describes ratios between 1:30 and 1:100 for real lenses. For some of the Friesian Islands off the German North Sea shore, ratios between 1:20 and 1:60 were calculated, using the smallest widths of these elongated barrier islands. Flow processes in the physical model are therefore affected by an at least tenfold vertical exaggeration. The Dupuit assumption of horizontal flow within the lens, as applied in many analytical models, is thus violated to some degree, especially far from the coast.

(2) In the physical model, a capillary fringe inevitably developed above the water level. Such a fringe can also be found in real freshwater lenses but is of much less importance there, as the fringe usually constitutes only a small percentage of the thickness of the unsaturated zone. In the model, the measured fringe thickness covers almost the entire unsaturated zone. Flow in the unsaturated zone was therefore not considered for numerical modeling.

(3) The physical model is not strictly two dimensional because of its thickness of 5 cm. Nevertheless, simulating homogeneous recharge and groundwater flow of such a slice of an infinite strip island is still possible without significant deviations from reality. In the case of a singularity, e.g. a pumping well, flow becomes three-dimensional. In that case, boundary effects of the walls will lead to deviations of the mathematical models from the observed results.

(4) Reading off values from the film recordings of the experiments has an accuracy of about one centimeter due to uneven recharge pattern and dispersion of colors during transport.

2.1.2 Analytical models

The maximum thickness h (L) of an infinite strip oceanic freshwater lens in a single layer aquifer can be calculated using the formula by Fetter (1972):

$$h^2 = \frac{R(L^2 - x^2)}{K(1+\alpha)} \tag{2.1}$$

where R is the recharge rate (L T^{-1}), L the half width of the island (L), x the horizontal distance from the island center (in this case $x = 0$) (L), K the hydraulic conductivity (L T^{-1}) and β the Ghyben-Herzberg factor (Badon-Ghyben, 1888; Herzberg, 1901):

$$\beta = \frac{\rho_f}{\rho_s - \rho_f} \tag{2.2}$$

where ρ_s (M L^{-3}) and ρ_f (M L^{-3}) are the density of salt and freshwater, respectively. Vacher (1988) presented a very similar formula to calculate the maximum thickness h (L) of a freshwater lens:

$$h^2 = \frac{R(\alpha+1)L^2}{K} \tag{2.3}$$

The transient development of the thickness of a freshwater lens can be calculated using the analytical model proposed by Stuyfzand and Bruggeman (1994), based on work by Brakel (1968) and Bakker (1981), both cited in Stuyfzand and Bruggeman (1994).

$$t = \frac{f_1 \cdot f_2}{2} \cdot \sqrt[-2]{\left[\frac{4 \cdot R \cdot K \cdot (\rho_s - \rho_f)}{(n_e \cdot B)^2 \cdot \rho_s}\right]} \cdot ln\left[\frac{1+\frac{Z_t}{Z_\infty}}{1-\frac{Z_t}{Z_\infty}}\right] \tag{2.4}$$

where B is the width of the dune belt (here $B = 2L$) (L), Z_t is the depth to the interface at time $t = t$, Z_∞ is the same at $t = \infty$ (steady state), f_1 is a correction factor to account for aquifer anisotropy, here $f_1 = 1$ (see Stuyfzand and Bruggeman, 1994 for a detailed description), f_2 is a correction factor to improve fit to a numerical model by Bakker (1981, cited in Stuyfzand and Bruggeman, 1994), here $f_2 = 1$.

For infinite strip islands, the formula to calculate travel times t in an unconfined horizontal aquifer as a function of the horizontal location x by Chesnaux and Allen (2008) is:

$$t(x) = n_e \sqrt{\frac{\rho_f + \Delta\rho}{R \cdot K \cdot \Delta\rho}} \cdot \left[\sqrt{L^2 - x^2} - \sqrt{L^2 - x_i^2} - L \cdot ln\left(\frac{L+\sqrt{L^2-x^2}}{L+\sqrt{L^2-x_i^2}} \frac{x_i}{x}\right)\right] \tag{2.5}$$

where n_e is the effective porosity, $\Delta\rho = \rho_s - \rho_f$ and x_i the initial position on the island ($x_i > 0$).

14

2.1.3 Numerical model

For numerical modeling the finite element model Feflow 5.4 was used (Diersch, 2005). A two dimensional model with parameters and boundary conditions based on the setup of the physical model was generated. A trapezoidal mesh with 112,528 elements and 56,791 nodes was used. The grid was refined in the middle of the model at its axis of symmetry and around the wells to avoid numerical dispersion. The upper boundary of the mesh was assigned a Neumann (constant flux) boundary condition, allowing only freshwater to enter the model. An unsaturated zone was not considered for the reasons mentioned above.

The coastal zones were defined as Dirichlet boundaries (constant head) with a saltwater head of 0.3 m (upper model boundary). Considering the cell sizes and the short flow path lengths in the range of a few centimetres, longitudinal and transversal dispersivities were set to 5×10^{-3} m and 5×10^{-4} m, respectively. The molecular diffusion coefficient was set to 10^{-9} m^2 s^{-1}, although the elevated flow velocities in the model render diffusion negligible.

The discretization in time allowed an automatic adaption of the time-step during the model run. Initial time step length was set to 0.864 s, with a maximum ratio for changing the time-step size (new/old) of 1.3 and an upper bound of 8.64 s.

In the case of a pumping well, the model was expanded to a three dimensional model. Six layers with a spacing of 1 cm in the z direction were duplicated from the two dimensional model grid with identical flow and transport parameters.

2.2 Results

2.2.1 Steady state lens thickness as a function of recharge

In the first experiment, the influence of recharge rates on the maximum steady state lens thickness in the middle of the "island" ($x = 0$) was investigated. The physical model results were compared to analytical models by Fetter (1972) and Vacher (1988), as well as to a numerical Feflow model (Figure 2-2).
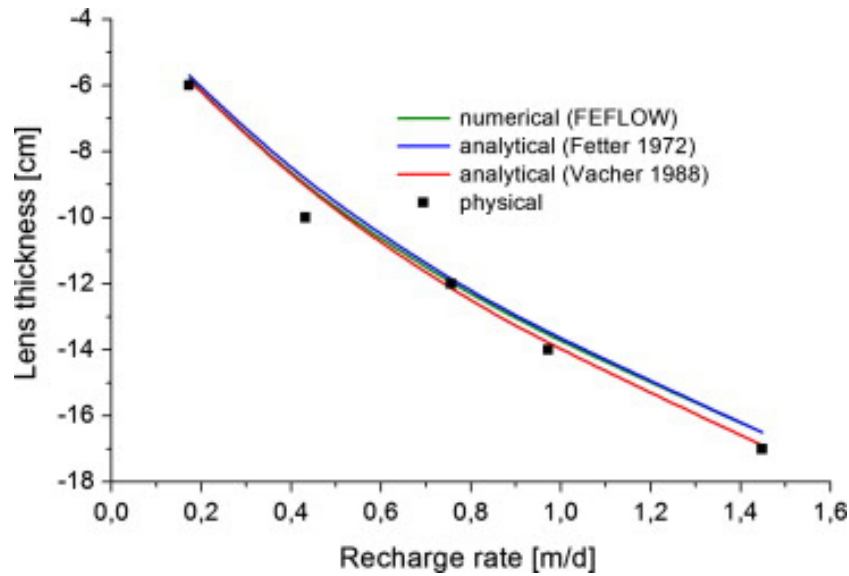
Figure 2-2: Maximum lens thickness at $x = 0$ under steady state conditions as a function of recharge rate from physical, analytical and numerical models.

Both analytical models yield, as expected, almost identical results (Figure 2-2). The numerical calculation is in exact accordance with the solution by (Fetter, 1972). The physical model results match the predicted lens thicknesses well. The slight deviations can be attributed to observational inaccuracies.

The comparison of the Feflow simulations to the analytical models and the results from the sand box experiments show, that the numerical code can successfully simulate the results of the physical models.

2.2.2 Transient lens genesis and degradation

By applying a constant freshwater recharge rate of 0.046 m³ d⁻¹ (1.152 m d⁻¹) to the physical model, a lens developed and reached dynamical equilibrium after around 200 min (Figure 2-3a, see also Video 1, Supplementary material). At this quasi steady state condition, a maximum thickness of 15 cm below the original salt water level was observed. At the end of the first stage of this experiment, recharge was turned off and the degradation of the lens was monitored (Figure 2-3b; Video 2, Supplementary material). To maintain the boundary conditions during this stage, saltwater inflow into the model had to be enabled. This was done with a rate of 0.96 m d⁻¹, through the backside piezometer (Figure 2-1) at the lower right and left corner of the model.
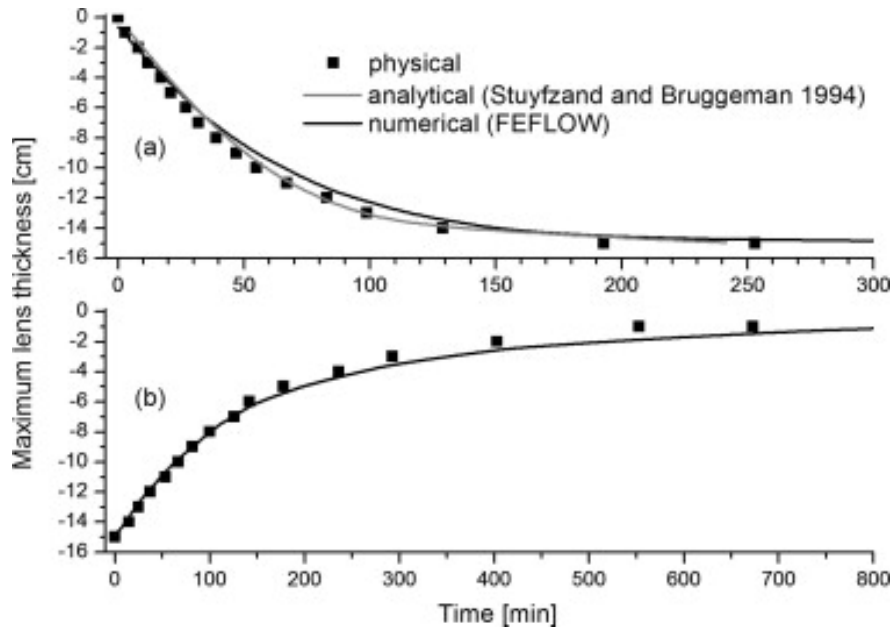
Figure 2-3: Physical, analytical and numerical results of lens thickness at $x = 0$ as a function of time for (a) freshwater lens formation at recharge rate $R = 1.152$ m d^{-1} and (b) freshwater lens degradation after turning off recharge.

Figure 2-3a shows that the transient development of the lens thickness at $x = 0$ is in good accordance to the analytical and numerical simulation results. No calibration of the initial hydraulic parameters was needed. The degradation of the lens, on the other side, could be simulated only by the numerical model, as no analytical model is available. The curve fit is good (Figure 2-3b). It has to be considered, though, that in the physical model, water continues to seep from the unsaturated zone after turning off re-charge for some time, thereby retarding the process of lens degradation.

The two different shapes (velocities) of the generation (Figure 2-3a) and degradation curves (Figure 2-3b) can be explained by differences in the hydraulic driving forces for each phase. The main difference is the active recharge during the formation of the lens while during degradation this force is not active.

2.2.3 Flow paths and travel times

Flow paths coud be visualized within the freshwater lens by switching the color of every second recharge drip point (indigotine/eosine) in periodic intervals, while all other drips remained on uranine. This was done after equilibrium between fresh and saltwater had been established (Video 3, Supplementary material). As shown in Figure 2-4 all flow paths are connected to the discharge zones to the left and right side of the island. Due to the exaggeration of the lens´ thickness in comparison to its width, the vertical flow component is clearly visible.
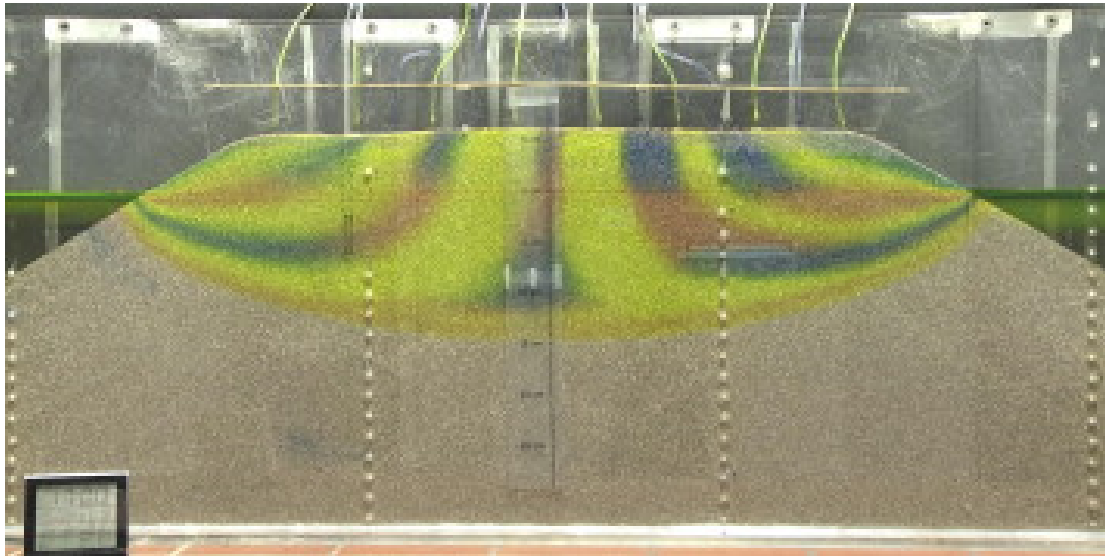
Figure 2-4: Sand-box model visualizing flow paths with color variations of 60 min duration at every second recharge drip (well inactive).

The travel times along the flow paths were measured (Figure 2-4). Results are shown in Figure 2-5 and compared to calculations based on the analytical model (equation 2.5) by Chesnaux and Allen (2008) and numerical simulation results with Feflow.
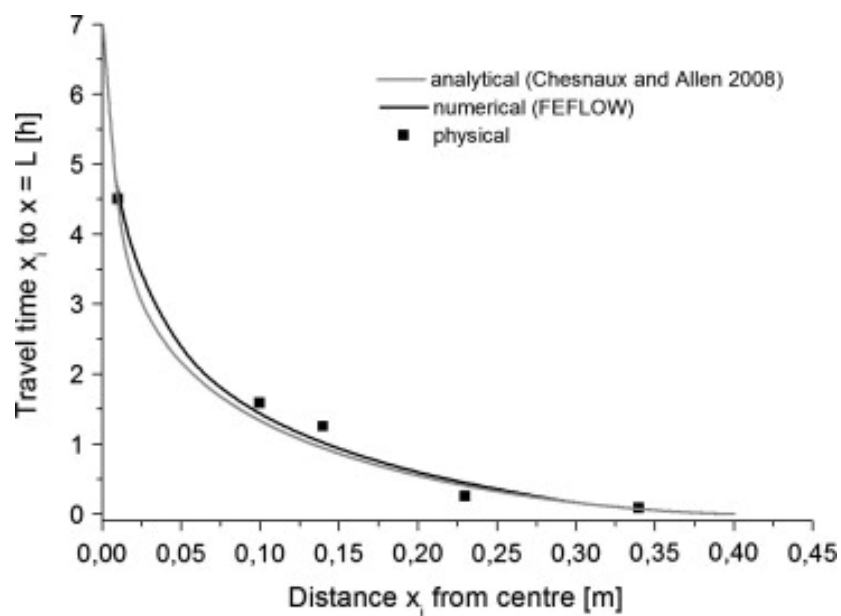
Figure 2-5: Comparison of travel times as a function of distance from the island center from physical, analytical and numerical models.

The differences between the physical data and the curves for the analytical and the numerical models shown in Figure 2-5 are quite minor. They can be attributed to the limited observational accuracy. Even the fact that the analytical model considers only horizontal flow, based on the Dupuit assumption, while in the physical model a vertical flow component is clearly visible, is apparently not of concern.

2.2.4 Age stratification

Age dating of water in subsurface hydrology is used to e.g. calculate mean residence times and available groundwater quantities, the progression of pollutants and to investigate climatic effects. The "age" of groundwater is defined as the period of time between the arrival of seepage water at the groundwater table and the time of sampling.

A visualization of groundwater age in the lens was possible by changing colors of recharge water over time (Video 4, Supplementary material). By simultaneously switching all drips from one color to another, infiltration events (fronts) became visible. The layering visible in Figure 2-6 is a result of a series of subsequent infiltration events. Recharge rate was maintained constant at 1.152 m d^{-1} during the entire experiment. At first, a lens was generated using freshwater with uranine until equilibrium (layer 1, Figure 2-6). Then colors were subsequently switched to:

• Eosine (red) for 120 min (layer 2, Figure 2-6)

• Indigotine (blue) for 100 min (layer 3)

• Uranine (yellow) for 80 min (layer 4)

• Eosine (red) for 60 min (layer 5)

Figure 2-6: Sand-box model visualizing age stratification of five successive infiltration events (well inactive). SSp = saltwater spot, colored.

After the last 60 min of recharge with eosine, the photo shown in Figure 2-6 was taken. An image of the age stratification within the freshwater lens became visible. A very similar pattern could be reproduced using particle tracking in the numerical model (not shown here).

2.2.5 Visualization of saltwater movement

Due to the dispersive entrainment of salt water at the interface, a slow convection cell develops in the saline zone (Cooper, 1959; Reilly and Goodman, 1985; Michael et al., 2005). Small volumes of colored salt water were injected with a syringe into this zone to visualize movement of salt water (Figure 2-6). As expected, movement of saline water is very slow and becomes visible only close to the interface, especially at the discharge zone and around the area of up-coning below a pumping well. In the latter case, the films recorded trace the flow paths of salt water rising up to the well (Video 4, Supplementary material).

2.2.6 Up-coning under vertical and horizontal wells

Two physical experiments to compare the performance of a vertical and a horizontal well were performed. The parameters of the horizontal well was chosen to be as similar as possible to the vertical well to avoid a bias towards the former. With the exception of the screen being vertical or horizontal, respectively, all parameters were equal. The shafts of both wells were installed at the same distance from the "coastline". The pump, simulated by the intake of the

suction tube, was installed at a depth of 2.5 cm below sea level (on top or at the beginning of the screen, respectively). Screen length was 4 cm for both wells. The distance from the bottom of the screen to the undisturbed interface was 10 cm and 6 cm for the horizontal and vertical well, respectively.

The two experiments started with pumping from the vertical well and later, after complete recovery of the lens, from the horizontal well. The initial freshwater lens had a maximum thickness of 15 cm below sea level at $x = 0$. Three different pumping rates were applied for 1.5, 2.5 and 1.5 h, respectively, as indicated by the dashed lines in Figure 2-8. The pumping rates for the horizontal well were 0.8 ml min^{-1} higher (maximum deviation of 6%) for all three steps due to technical reasons.

For the first pumping rate, no rise in electric conductivity was observed in neither the vertical nor the horizontal well. Even though electric conductivity remained at 590 μS cm^{-1} for 1.5 h of pumping, a slight rise of the interface could be visually observed in both cases. Increasing the pumping rate by around 5 ml min^{-1}, electric conductivity differed significantly between both wells. While the horizontal well showed a slightly elevated but almost constant conductivity of 660 μS cm^{-1} after 2.5 h, the vertical well showed beginning salt water intrusion, indicated by a final conductivity of 1600 μS cm^{-1}. For the third pumping rate, both wells showed a clear break-through of saltwater (Figure 2-7). The vertical well, however, shows a much higher proportion of saltwater intake.

The minor fluctuations in the electric conductivity signals shown in Figure 2-7 are triggered by intermittent input of saltwater. These injections were necessary to replace the pumped saltwater volume. The experiments show that a horizontal well can pump at a higher rate than a vertical well without compromising the interface.
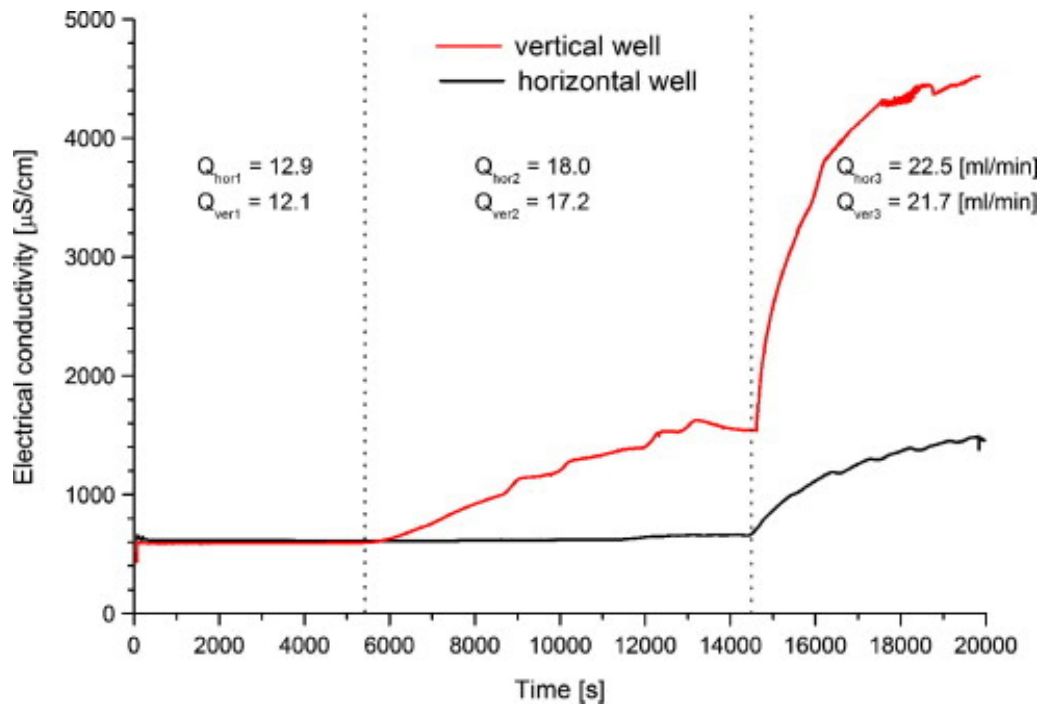
Figure 2-7: Electric conductivity of water pumped from the horizontal (black) and the vertical well (red) showing different reactions to the applied pumping rates (changes in pumping rate indicated by dashed lines). (For interpretation of the references to colour in this figure legend, the reader is referred to the web version of this article.)

The results cannot be transferred directly to real world up-coning due to the boundary conditions of the physical model. However, the boundary effects equally influence the horizontal and the vertical well, and therefore allow a comparison. Yet, in reality, horizontal wells are often installed at more shallow depth and often have several screens and higher pumping rates.

2.3 Discussion

The presented findings, especially the travel times and the age stratification, have some interesting implications for the interpretation of groundwater ages in freshwater lenses, e.g. by isotopic analyses:

(1) A freshwater lens must not be considered a well-mixed reservoir. A non depth-specific sample from a long well screen includes unknown proportions of water of different residence times, yielding a mixed age of no real value, especially if no flow model is available. Two identical wells (same screen depth and length, same pumping rate) may yield completely different residence times depending on their position on the island (wells A and B, Figure 2-8). A well close to the middle may predominantly tap from the thick layer of young water present

there while a well close to the coast may tap various age zones due to the vertical movement close to the discharge zone.
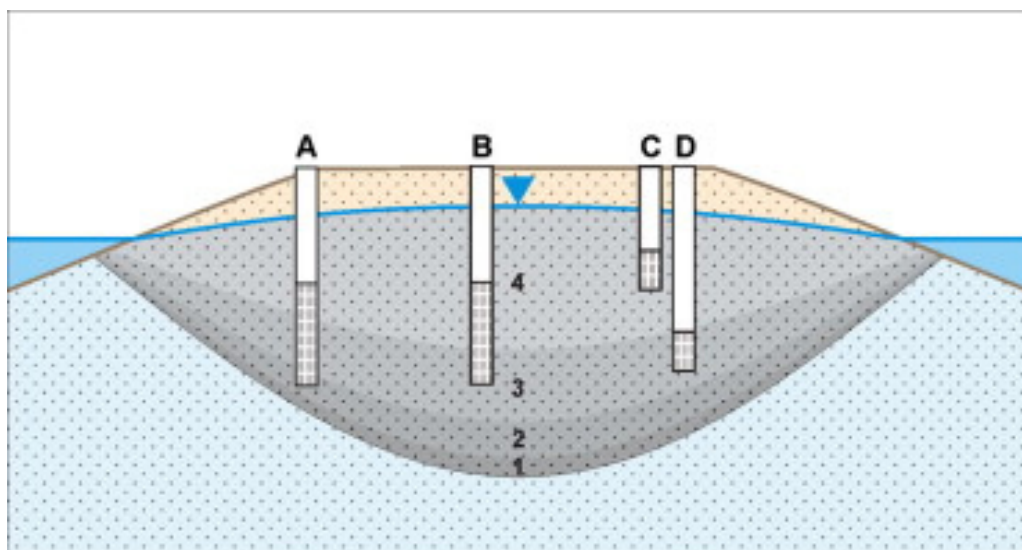
Figure 2-8: Sketch of a freshwater lens with wells tapping groundwater at different distances from the shore (A) and (B), and with different screen depths (C) and (D). Numbers 1–4 denote layers of different times since recharge.

(2) The thickness of the discrete layers (infiltration events), visualized by different tracer colors, decreases over time. The proportion of young water in the water column is higher than that of older water. Wells C and D show the effect on the age of pumped water (Figure 2-8).

(3) All water layers remain in contact with the discharge zone at all times until they are completely squeezed out or mixed away at the interface through dispersion and diffusion. As an example, the thin eosine layer close to the interface (Figure 2-6) was recharged for 120 min, while the eosin layer close to the surface was recharged for only 60 min. The "age" of groundwater at the bottom of the lens gives an estimate of the maximum travel time but not of the age of the formation of the lens itself. Older layers may have been "squeezed out" already.

(4) The proportions of water of different residence times pumped from the screen of a well depend on the depth and length of the screened interval, the hydraulic conductivity of the layers and the position of the pump (e.g. Houben and Hauschild, 2011).

(5) The age stratification of the water column may include layers of different recharge rates or even one or more hiatus, e.g. caused by dry years with low or even no recharge. The duration of the dry period must of course not exceed the time necessary to completely degrade the lens.

(6) The calculation of travel times based on models of the hydraulic flow regime, is a necessary prerequisite to validate groundwater ages derived from radionuclide tracers, such as tritium or radiogenic carbon.

2.4 Conclusions

In the physical experiments time-dependent applications of artificial tracers were used for the first time to visualize internal flow processes, e.g. flow paths and age stratification in a two dimensional cross section of a freshwater lens. The physical model results for steady state lens thickness, formation and degeneration, travel times and age stratification were successfully compared to numerical and, if applicable, analytical model calculations.

Particularly, this study has shown that investigations of groundwater age and residence times within a freshwater lens can only be interpreted with the understanding of the flow regime. This imposes restrictions on the sampling of water for age dating, e.g. samples need to be depth-specific in order to yield useful results.

The flow paths and travel times find their practical application in the delineation of protection zones, e.g. the 50-day zone which is intended to prevent fecal bacteria from entering a well. They can also be used to predict the degradation of pollutants, if kinetic rate laws are known, and the propagation of radionuclide tracers such as tritium.

The presented findings also have some practical implications for sustainable water resource management, e.g. the sustainable pumping rate of wells. By using physical experiments it was shown that a horizontal well with the same screen depth and distance to shore allows a higher sustainable yield than a vertical well.

Anisotropy and geological heterogeneities which were not considered in the experiments may significantly disturb the flow field and will cause deviations from the continuous age stratification. Further investigations will focus on lens dynamics in layered systems, variations of island morphology and artificial groundwater recharge.

3 Physical experiments on freshwater lens dynamics: Heterogeneous Cases

The work of this chapter has been published as: Stoeckl, L., Houben, G.J., Dose, E.J., 2015. 'Experiments and modeling of flow processes in freshwater lenses in layered island aquifers: Analysis of age stratification, travel times and interface propagation'. In: *Journal of Hydrology*, 529, Part 1: 159-168.

3.1 Experimental methods and materials

3.1.1 Case definition

The four model cases studied here (Cases A–D) are described by Vacher (1988) and Dose et al. (2014) comprise idealized, infinite-strip island set-ups (Figure 3-1), which are based on typical features of freshwater lenses common worldwide. The island aquifer in Case A consists of two vertical side-by-side strips of different hydraulic conductivities (K), but with homogeneous recharge. The geological conditions at Bermuda are similar to this case, where two adjacent limestone sequences of different ages and hydraulic conductivity can be found (Vacher, 1978; Vacher and Wallis, 1992). In Case B, different freshwater recharge rates are set for the two halves of the island, whereas the aquifer material is homogeneous. The Hawaiian Islands are an example for this case, where strong contrasts in precipitation and groundwater recharge on the windward and leeward sides occur (Macdonald et al., 1990). A modification of Case B is included in this study, where the recharge in one half of the island is set to zero. The southern Bahamas, e.g. Great Exuma, provide examples for this modified case, where the potential evapotranspiration locally exceeds the amount of rainfall and net recharge may be zero or even negative (Wallis et al., 1991; Vacher and Wallis, 1992). The island aquifer in Case C is layered horizontally, with a highly permeable formation overlain by a less permeable upper formation ($K_1 < K_2$; Fig. 1C). Examples for such a geology can be found among the larger islands of the Bahamas (e.g. Ayers and Vacher, 1986 and Budd and Vacher, 1991). The otherwise homogeneous freshwater lens in Case D is truncated at depth by an impermeable layer. Similar conditions can be found at Shelter Island (USA), the Pingelap Atoll (Micronesia), Kish Island (Iran) and the town of Benjamin Aceval (Paraguay) (Ayers and Vacher, 1986; Rozell and Wong, 2010; Ataie-Ashtiani et al., 2013; Houben et al., 2014b).
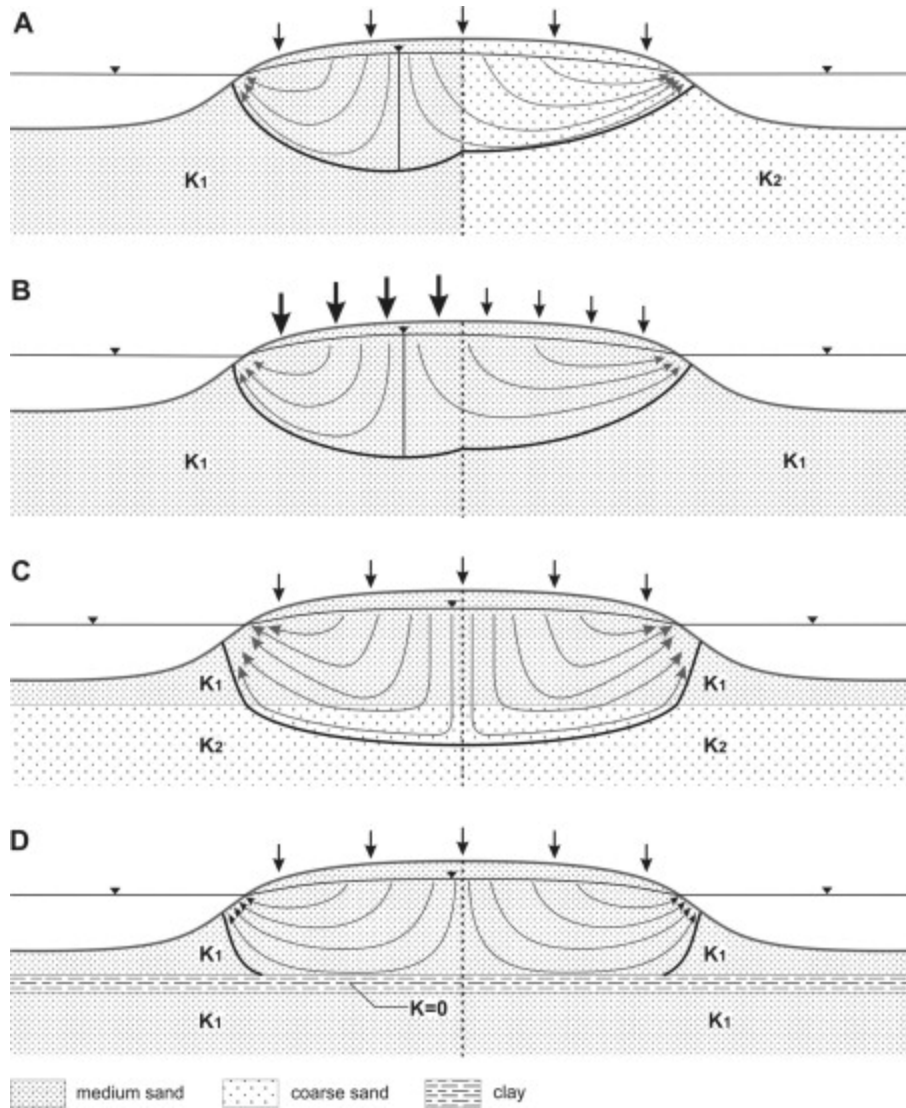
Figure 3-1: Sketch of the four configurations of heterogeneous island freshwater lenses: Case A: lateral variation of hydraulic conductivity ($K_1 < K_2$), Case B: lateral variation of groundwater recharge R ($R_1 > R_2$), Case C: horizontal layering ($K_1 < K_2$), Case D: freshwater lens truncated by an impermeable base. The dotted line indicates the center of the island at $x = 0$ cm (Modified after Vacher, 1988).

A fifth model (Case E) was introduced by Dose et al. (2014) where a low permeable formation is overlain by a higher permeable upper formation (reversed Case C). This case was not included here, because the freshwater barely penetrates into this lower layer. Therefore, flow paths are difficult to visualize and travel times were not measurable.

The definition of groundwater age employed here is the time needed for a package of water to traverse the distance from its recharge location at the water table to a point in the subsurface (Bethke and Johnson, 2008). Travel times are defined as the time a small package of water needs from a position at the surface along a flow path to the outflow zone.

3.1.2 Physical model experiments

The experimental set-up is based on the one used by Stoeckl and Houben (2012). A coarse and a medium filter sand represent different aquifer materials. Their grain size distribution was determined optically using a Camsizer® (Retsch Technology, Germany), which has a measurement range between 30 μm and 30 mm. Using a helium pycnometer by Micromeritics®, Germany, bulk and mineral densities were measured. Uncompacted porosities were then calculated for the coarse and medium sand, which were 0.41 and 0.45, respectively.

The saturated hydraulic conductivity was measured using a constant-head permeameter (Darcy apparatus) by Eijkelkamp Agrisearch (Netherlands). They were also calculated from granulometric data using the empirical methods by Seelheim (1980), Hazen (1892), and Bialas and Kleczkowski (1970). Coarse and medium filter sands showed a ratio in hydraulic conductivity of roughly 10:1. Measurement results for minimum, average, and maximum hydraulic conductivity are shown in Table 3-1. The impermeable material used for Case D was pink plasticine (Play-Doh, Hasbro, USA).

Table 3-1: Measured hydraulic conductivities for medium and coarse sand (in m s^{-1}), obtained from Darcy tests and grain size analyses (adapted from Dose et al., 2014).

	Minimum K	Maximum K	Average K
Medium sand	$7.3 \cdot 10^{-4}$	$2.1 \cdot 10^{-3}$	$1.4 \cdot 10^{-3}$
Coarse sand	$3.9 \cdot 10^{-3}$	$2.3 \cdot 10^{-2}$	$9.7 \cdot 10^{-3}$

The experiments were started by applying freshwater recharge to the island surface (0.04 m^2) from fifteen freshwater drippers, supplied by a multi-channel peristaltic pump (Ismatec BVP, Germany). The recharge rate for Cases A, C and D was set to 1.33 m d^{-1}, equivalent to 2.46 ml min^{-1} per dripper. For Case B and B-modified, the recharge rates were 1.38 m d^{-1} for the left sector, and 0.67 m d^{-1} and 0.0 m d^{-1} for the right sector, respectively.

To visualize flow paths and to measure travel times and age stratification in the physical model, an approach described by Stoeckl and Houben (2012) and Chang and Clement (2013) was applied: The tracer dyes uranine (yellow), eosine (red) and indigotine (blue) were added to the freshwater at a concentration of 0.3 g l^{-1}. Travel times were measured, following a triple point between three different tracer colors along a distinct flow path from its horizontal position x at the water table (around 0.3 m above ground) to the discharge zone (Videos 5–8, Supplementary material). Travel times through the unsaturated zone (around 3 cm thick),

above the saltwater level of 0.3 m, were not considered. For the age stratification, the dyed solutions were injected in the following sequence: (1) yellow, (2) blue, (3) red, and (4) again yellow. The effects of the tracers on density and viscosity of the fluid are negligible at this low concentration.

3.1.3 Numerical model

For numerical modeling, the finite element model Feflow 6.1 was used (Diersch, 2014). A triangular mesh with 18,629 elements and 9580 nodes was generated for Cases A–C. For Case D, a smaller domain with a coarser resolution of 14,106 elements and 7293 nodes was used, representing the aquifer above the impermeable basement. Hydraulic parameters and boundary conditions were based on measurements of the physical properties of the materials as listed above and the setup of the physical models.

The 2D trapezoidal grid was refined at the axis of symmetry of the model and around the layer boundaries. A grid dependency test showed no significant changes in interface position and salt concentration when refining the mesh further. The upper boundary of the domain was assigned a constant flux (Neumann), together with a transport boundary condition, to assure that only freshwater enters the model here. The unsaturated zone was not considered in the numerical models. The good fit of experimental and model data in previous studies with similar set-up (Stoeckl and Houben, 2012; Dose et al., 2014) showed that this is a valid simplification. Coastal zones were defined as constant head boundaries (Dirichlet) with saltwater heads of 0.3 m and a solute concentration of 35 kg m^{-3}. The lower boundaries of the numerical models were defined as no flow boundaries (Neuman), which represent the bottom of the sand box for Cases A–C and the impermeable basement for Case D, respectively.

Minimum and maximum hydraulic conductivities for the coarse and medium sand, determined in the laboratory (Table 3-1), were used to constrain values used for the calibration of the numerical models to the experimental data. The calibration was based on the parameter set used by Dose et al. (2014) for the calculation of the steady-state interface positions. The calibrated values for the different cases are summarized inTable 3-2. The hydraulic conductivity of all layers was assumed to be homogeneous and isotropic. Considering the cell sizes and potential lengths of flow paths, longitudinal dispersivity was set to 5 mm. Transversal dispersivity was always set to a value of one order of magnitude smaller than the respective longitudinal dispersivity.

Table 3-2: Hydraulic conductivities used for numerical modeling (initial).

	Hydraulic conductivity [m s^{-1}]	
Case	K_1	K_2
A	0.0021	0.0230
B	0.0021	$=K_1$
C	0.0021	0.0120
D	0.0023	0.0000

Travel times in the numerical model were calculated using particle tracking along flow paths, starting from the horizontal upper boundary (freshwater recharge) to the outflow zones. Age stratification was visualized in the numerical simulation using discrete temporal markers along the flow path, calculated by particle tracking.

3.1.4 Analytical solutions

For calculating the age stratification of Case D, two analytical models by Vogel (1967), Vogel (1970), and Greskowiak et al. (2013) were applied. For Cases A–C, no such analytical solutions exist to my knowledge. The model by Vogel (1967) and Vogel (1970) calculates the age t [T] of the water over a vertical profile in a non-truncated island by:

$$t = \frac{n_e\, h}{R} \ln \frac{h}{z} \tag{3.1}$$

where n_e [–] is effective porosity, h [L] total depth (thickness) of the lens, R [L T^{-1}] recharge rate and z [L] height above the impermeable bedrock where the age shall be determined.

The two dimensional age distribution for a truncated lens, based on the analytical solution of travel times in an unconfined aquifer by Chesnaux and Allen (2008), was calculated after Greskowiak et al. (2013) using:

$$\Delta t = n_e \sqrt{\frac{1}{R \cdot K}} \times \left[\sqrt{C^2 - x_z{}^2} - \sqrt{C^2 - x_i{}^2} - C \ln\left(\frac{C + \sqrt{C^2 - x_z{}^2}}{C + \sqrt{C^2 - x_i{}^2}} \frac{x_i}{x_z} \right) \right] \tag{3.2}$$

with:

$$C = \sqrt{L^2 + \frac{K}{R}Z^2}$$
(3.3)

where x_i [L] and x_z [L] are initial and final flow path positions on the island, respectively, L [L] being the half width of the island and Z [L] the depth of the aquifer base.

3.2 Results and discussion

3.2.1 Appraisal of deviations between physical and mathematical models

In all experiments presented here, a strong vertical exaggeration was induced by the application of recharge rates, which are very high compared to real-world cases. This exaggeration, however, made it possible to visualize and measure flow processes within the lens, which is the focus of this investigation. Some deviations between the physical and mathematical models were to be expected. They may be attributed to the following features:

1. The arrangement of sand layers and recharge tubes in the physical model experiment deviated slightly from the idealized numerical model.

2. Small temporal fluctuations of recharge rate and the saline water table in the physical model experiment.

3. Unsaturated zone processes were neglected in the numerical modeling.

4. Measurements of travel times have an observational inaccuracy in the range of a centimeter due to the blurring of the colors, especially close to the outflow zones. The number of flow paths in the physical model is limited, from nine to twelve.

5. The plasticine layer used to represent the impermeable basement in Case D had a somewhat uneven surface, probably leading to a reduced horizontal flow component close to its surface and possibly to the entrapment of small residual saltwater pools.

6. All four cases use different spatial arrangements of the sands. The backfilling inevitably led to different degrees of compaction which was found to cause differing porosities and conductivities of the same material going from experiment to experiment.

7. The transition zone between fresh- and saltwater in the small scale experiments is basically a sharp interface. In nature, it can have thicknesses of up to several tens of meters (Stuyfzand and Bruggeman, 1994; Naumann, 2005).

3.2.2 Age stratification at steady-state

Figure 3-2 shows the age stratification at steady-state, obtained by the sequential infiltration of dyed waters. In general, freshwater within the lens becomes older with depth. Compared to the homogeneous freshwater lens studied by Stoeckl and Houben (2012), both the heterogeneity in geology (Case A) and recharge (Case B) leads to a non-axisymmetric shape of the age strata.

In Cases A, the overall lens thickness and the thickness of a single age stratum in the left sector is greater than in the right, more permeable sector (Figure 3-2A). This is due to the higher flow velocities in the more permeable sector, which discharges water more quickly.
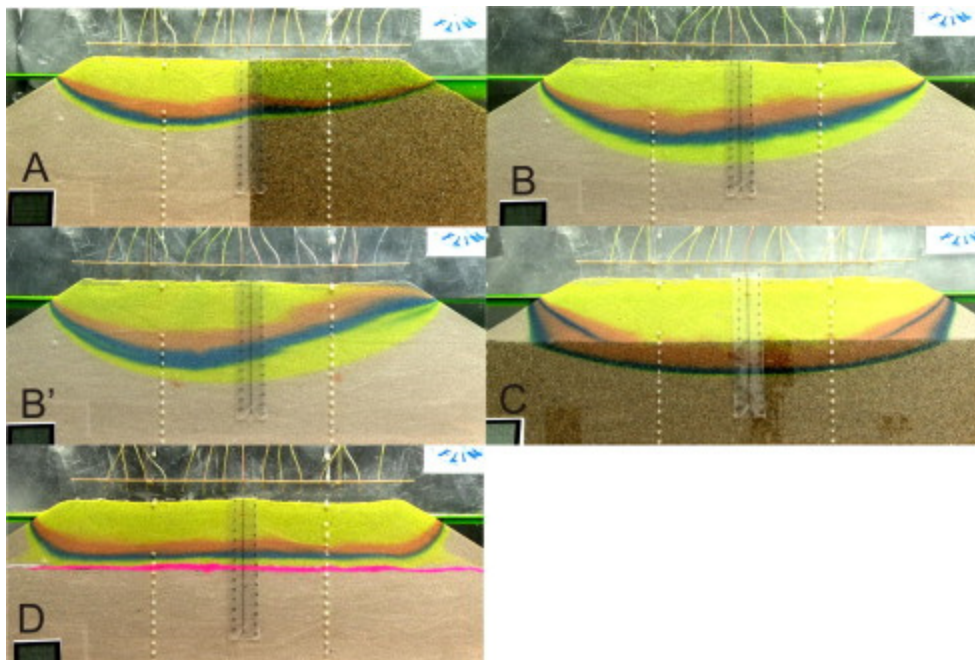
Figure 3-2: Age stratification visualized in physical model by changing tracer colors over time in the following sequence: uranine (yellow), indigotine (blue), eosine (red) and uranine (yellow). The distance from coast to coast is 80 cm.

For the spatially uneven groundwater recharge (Case B), the position of the age strata in the right sector, receiving less recharge, is relatively higher compared to the left sector. This is especially pronounced for Case B-modified (Case B′), where the recharge on the right sector is set to zero (Figure 3-2B and B′). Even here, the freshwater lens thickness is almost equal in

both sectors, due lateral flow from the recharged to the dry sector. The thickness of the age strata is slightly higher on the lower recharge side, reflecting the longer flow paths and the more pronounced horizontal flow component of the lateral flow. Field evidence of such a recharge-dependent age stratification was only recently found on Langeoog Island, Germany (Houben et al., 2014a).

In Case C a vertical "repeating" of the age stratification sequence develops close to the outflow zone. This means that younger water is overlain by older water, visualized by the blue water embedded within the younger red water (Figure 3-2C). In the underlying, more permeable sand layer, groundwater flow velocities are enhanced, leading to the observed vertical inversion of ages. To my knowledge, such an age inversion has not been documented for real-world islands. This would require a depth-specific sampling in the vicinity of the shoreline. Since such island geometries are not uncommon (e.g. Ayers and Vacher, 1986; Budd and Vacher, 1991), these findings are important when interpreting and using real-world age data, for example for the calibration of numerical models.

Only the age stratification for Case D resembles more or less the one for a homogeneous lens (Stoeckl and Houben, 2012), except for having a horizontal bottom (Figure 3-2D). In Figure 3-3, the analytical solutions for Case D are shown and compared to numerical and physical model results. Both analytical solutions (1D by Vogel, 1967 and Vogel, 1970 and 2D by Greskowiak et al., 2013) show very similar results for the vertical age stratification close to the center of the island. On the other hand, vertical flow in the numerical simulation is slightly faster than predicted by the analytical solutions. The physical model results show higher water ages, especially in the deeper part of the lens (6–10 cm below salt water level). At the center of the island, water needs around 250 min to reach the impermeable layer at a depth of -10 cm in the physical model. The explanation for that is twofold: first, the uneven surface of the impermeable layer reduces lateral flow and therefore conserves older water close to that layer. Second, the flow paths start to develop a horizontal flow component already in the unsaturated zone, which is not considered in the numerical or analytical models (compare Video 4, Supplementary material). This might lead to a smaller amount of water actually recharging the lens and therefore to older ages in the physical model. The results show that the analytical solutions by Vogel (1967), Vogel (1970), and Greskowiak et al. (2013) are useful even for the high recharge rates and for the vertically exaggerated scale of the laboratory experiments. The analytical models may thus serve as a first approximation to estimate groundwater ages in such restricted freshwater lenses.
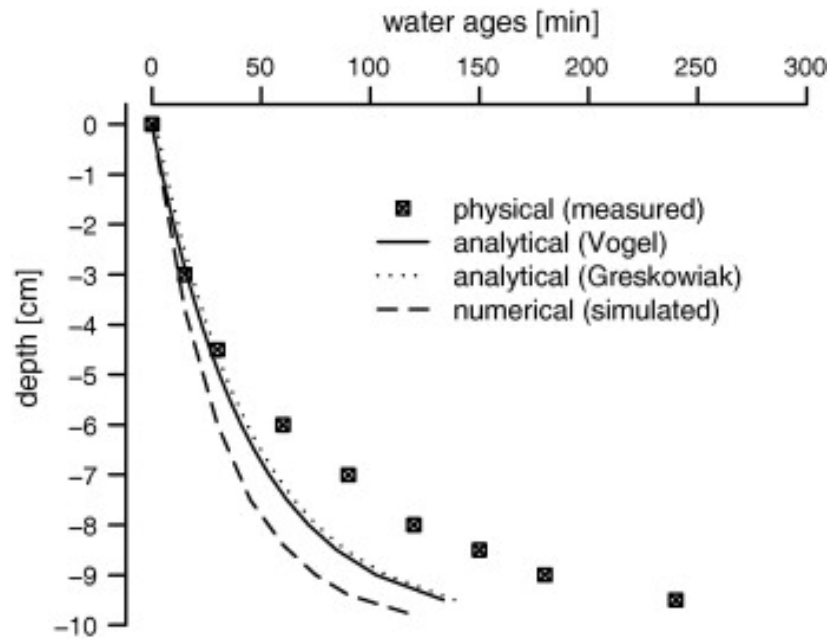
Figure 3-3: Physical, numerical and analytical model results of water ages close to the center of the island as a function of depth [cm] at steady-state for Case D.

3.2.3 Travel times at steady-state

The physical model experiments are analyzed for travel times along distinct freshwater flow paths through the lens. Each flow path is tracked from a recharge position x to one of the two outflow zones at the right or left side of the island. Times were measured from the horizontal position of the water table (around 0.3 m above ground).

Figure 3-4 shows the travel times for Cases A and B as a function of the horizontal position x, with $x = 0$ cm being the center of the island. The analysis for an island with two strips of different hydraulic conductivity (Case A) shows that travel times are longest for flow paths starting in the less permeable sand strip on the left (Figure 3-4a, Video 1, Supplementary material). In the physical model, the flow divide (where the longest travel times occurred) is shifted to the left sector of the island, by approximately 12 cm from the center. The numerical model reproduces the distribution of travel times well, but the modeled water divide was found at a position 17 cm left of the center. Slight inaccuracies in the physical boundary conditions may easily result in a shift of this magnitude.
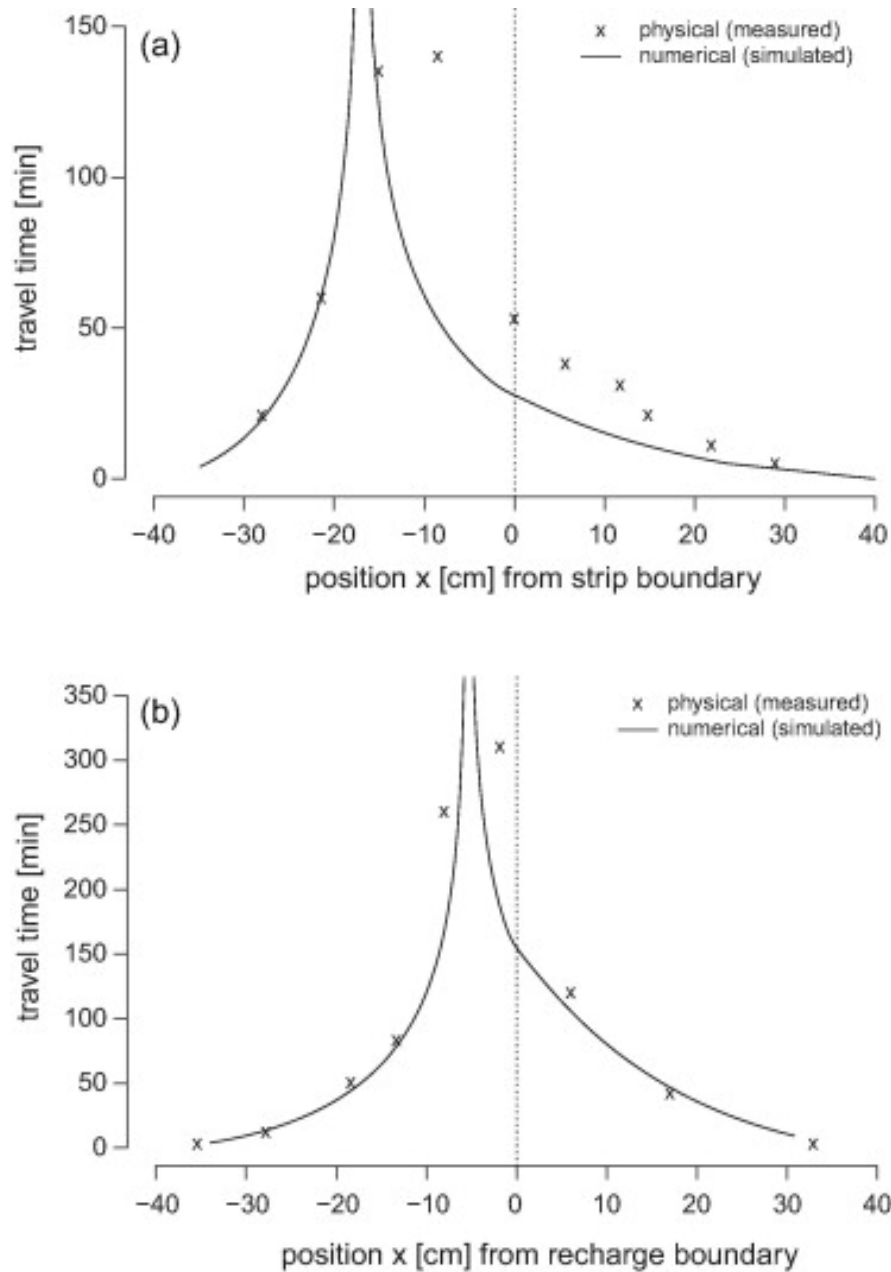
Figure 3-4: Travel times as a function of distance from the center of the island (dotted vertical lines) for (a) the strip boundary in Case A and (b) the recharge boundary in Case B.

For Case B, a similar shift of the flow divide occurs but is less pronounced compared to Case A. It shows a displacement of around 5 cm to the left from the center of the island in the physical model, something which the numerical model is able to recreate well (Figure 3-4b, Video 2), considering the range of observational accuracy. For longer travel times, that is for water starting from close to the water divide, deviations were slightly higher (around 3 cm, equal to a deviation smaller than 4%, compared to the total island length of 80 cm).

For Cases A and B, the distribution of travel times revealed a shift of the groundwater flow divide away from the geological and recharge boundary, respectively. For a real-world

34

situation similar to Case B, with a mountain ridge forming the surface water divide and at the same time the recharge boundary (e.g. due to differences in windward and leeward precipitation), the ridge is not equivalent to the groundwater divide. As expected, the lens is shallower on the lower recharge side of the island, because less water flows in this sector (Case B). Conversely, in Case A, flow volumes on the more permeable side of the island are higher, although the freshwater lens is shallower here. This is due to the higher hydraulic conductivity which causes a more rapid water transport out of the system. This has important implications for groundwater abstraction on islands of type A or B: because of the lower freshwater flux, a pumping-well on the shallow lens side on a Case B island might lead to much faster saltwater up-coning compared to Case A. Thus, not only the depth of the freshwater–saltwater interface but rather the groundwater flux is the measure of the sustainably extractable freshwater volume.

The mirror symmetry of Cases C and D is used to obtain a higher density of measurements from the physical model: measurement points from the left side of the island are mirrored back to the right side, as the mirror symmetry yields similar but not identical results, caused by naturally occurring slight heterogeneities in the physical model.

In Figure 3-5a, the distribution of travel times is shown for Case C from the center of the island ($x = 0$ cm) to the outflow zones ($x = 40$ cm). Here again, travel times show a maximum at the flow divide and decrease towards the outflow zones. However, a secondary maximum of the travel times occurs, approximately 15–20 cm away from the center of the island. This feature is observed in both, the numerical and the physical model. While travel times in Cases A, B and D increase continuously with increasing distance from the outflow zones, a bimodal distribution is thus observed for Case C. This is caused by the two different flow regimes that develop: flow paths originating close to the outflow zone pass through the upper layer of lower hydraulic conductivity only, while those originating closer to the center also penetrate into the deeper, more permeable layer (compare Figure 3-7c). The deviation between the physical and numerical model of around 5 cm (6% of top model width) at the secondary peak may be explained by the fact that travel times are read off from flow paths crossing both layers. This leads to an additional blurring of the tracer front and makes reading off travel times in the physical experiment more difficult.
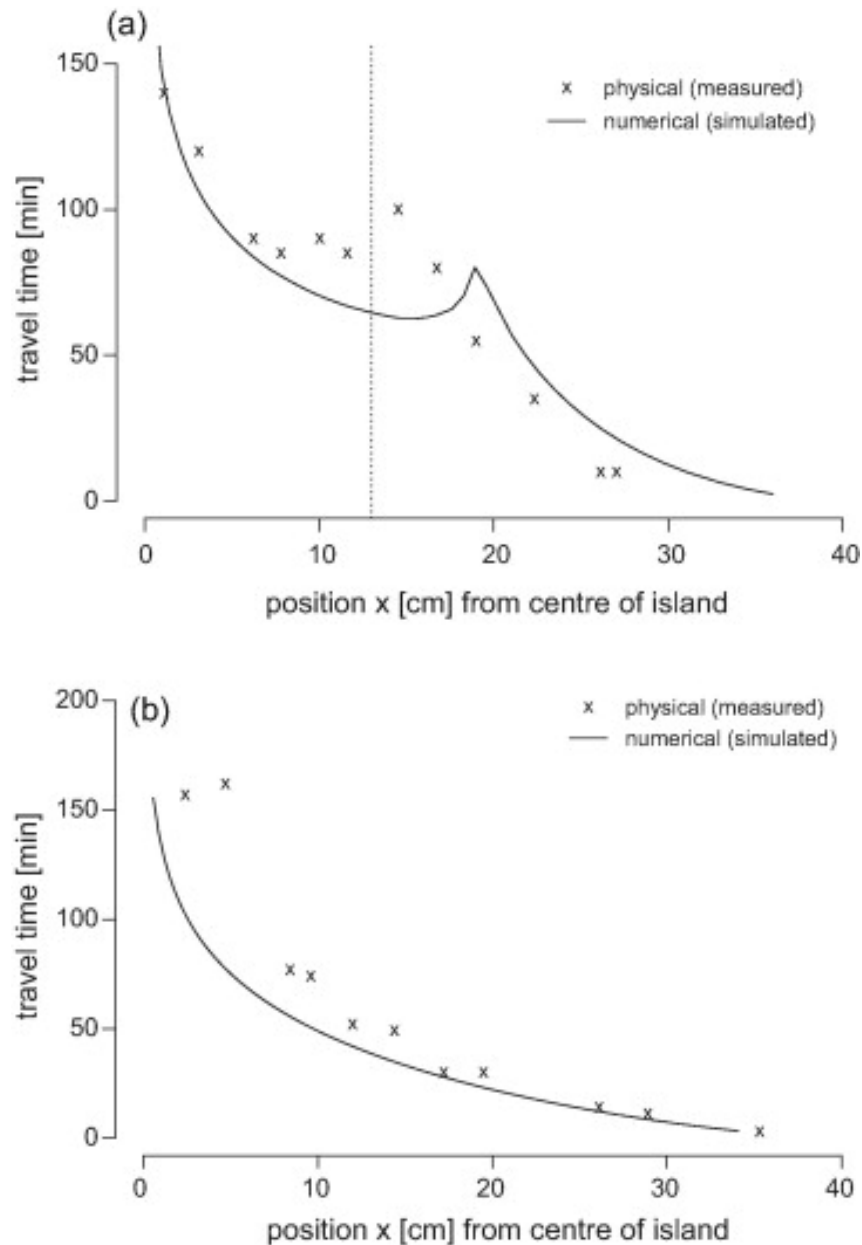
Figure 3-5: Travel time as a function of distance from the center of the island (a) Case C: the dotted vertical line indicates the separation of the two flow regimes visible in the physical model, flow paths left of the line penetrate into the second layer and (b) Case D.

For the delineation of groundwater protection zones, based on subsurface travel times, one can thus not make use of the general assumption that travel times increase with increasing distance from the coast here. The fact, that several equally fast travel times at different distances from the center occur, needs to be taken into account when considering the residence times of contaminants. However, the findings for Case C, cannot be transferred to systems where the lower layer is so strongly karstified that tidally-driven movement of saline water cuts off the freshwater lens from below (Underwood et al., 1992; Bailey et al., 2009; Bailey et al., 2012).

As expected, travel times for Case D are highest near the axis of symmetry (flow divide) at $x = 0$ cm and continuously decrease with decreasing distance to the coast (Figure 3-5b; Video 4). The numerical model is able to reproduce the trend observed in the physical experiment. Only close to the water divide, where flow paths are longest, the numerical model slightly underestimates the travel times observed in the physical experiment (Figure 3-5b). Generally, this case is the one closest to the homogeneous case studied by Stoeckl and Houben (2012).

Using the numerical models, water budgets are calculated for the outflow zones of each case. Volumes are equal for the symmetric Cases C and D (0.55 m^3 d^{-1}) on both sides, but vary for the non-axisymmetric Cases A and B. Outflows for the left and right side are 0.33 m^3 d^{-1} and 0.84 m^3 d^{-1} for Case A. For Case B the respective outflows are 0.48 m^3 d^{-1} and 0.35 m^3 d^{-1}. A comparison of the budgets for the right side of Cases A and B shows that the shallower lens side does not necessarily yield a smaller flux of water, i.e. does not necessarily imply that groundwater abstraction is more restricted here, as one would expect when solely looking at the freshwater lens thickness.

3.2.4 Transient interface propagation

The transient development of the freshwater lens in each physical model is observed by tracking the freshwater–saltwater interface at the center of the island over time (Videos 5–8, Supplementary material). In the numerical model, the movement of the 0.5 isoline, corresponding to 50% of the maximum saltwater concentration of 35 kg m^{-3}, is used.

All four cases show a similar pattern of initial fast growth of the freshwater lens, which slows down over time. Eventually, a steady-state depth of the interface is reached in all cases. In Figure 3-6, the temporal propagation of the interface at the center of the islands is shown for Cases A–D. During lens formation, the interface asymptotically reaches a final depth in Cases A and B, while the propagation is stopped by the impermeable layer in Case D. Times to reach steady-state position are around 150 min in all other cases, except Case B, which shows much longer times of around 450 min. Both, the numerical and physical models, yield similar results for the transient development and the steady-state interface position for all cases except for Case C. Generally speaking, the curve shapes of Cases A, B and D (Figure 3-6) resemble the one for a homogeneous lens obtained by Stoeckl and Houben (2012).
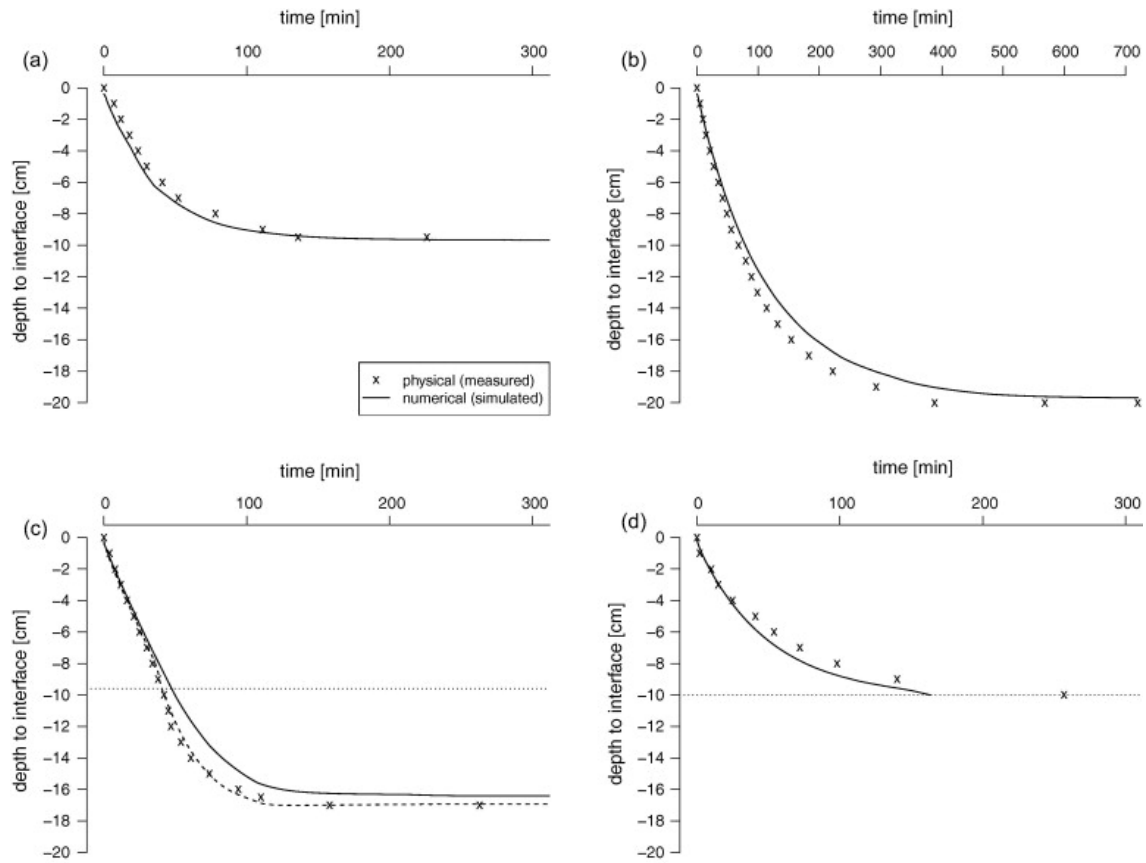
Figure 3-6: Interface position at the center of the island over time: experimental data (crosses) and numerically modeled 0.5 isoline position with the initial parameter set (solid line). (A–D) refer to the Cases A–D, respectively. The dashed line in (C) represents a numerical simulation with an adapted parameter set, while the dotted horizontal lines in (C and D) represent the layer boundaries. Note that the abscissa for Case B is scaled differently.

For Case C, Dose et al. (2014) showed that only flow paths emerging close to the center of the island penetrate into the lower layer. The new transient experimental data of Case C presented here (Video 7, Supplementary material), demonstrate that the interface accelerates when reaching the second, more permeable layer: In the first stage, the lens development proceeds similar to a homogeneous lens, although displacement of saline water through the second layer might affect the interface movement (Figure 3-7a). In the second stage, freshwater penetrates into the more permeable base layer and horizontally overtakes water flowing through the upper layer. The lens temporarily develops a "moustache" of protruding freshwater (Figure 3-7b). At the same time, the vertical propagation velocity of the interface increases due to the higher hydraulic conductivity of the base layer (compare Video 7, Supplementary material). Finally, at steady-state, an inflection point of the interface is established at the layer boundary (Figure 3-7c).
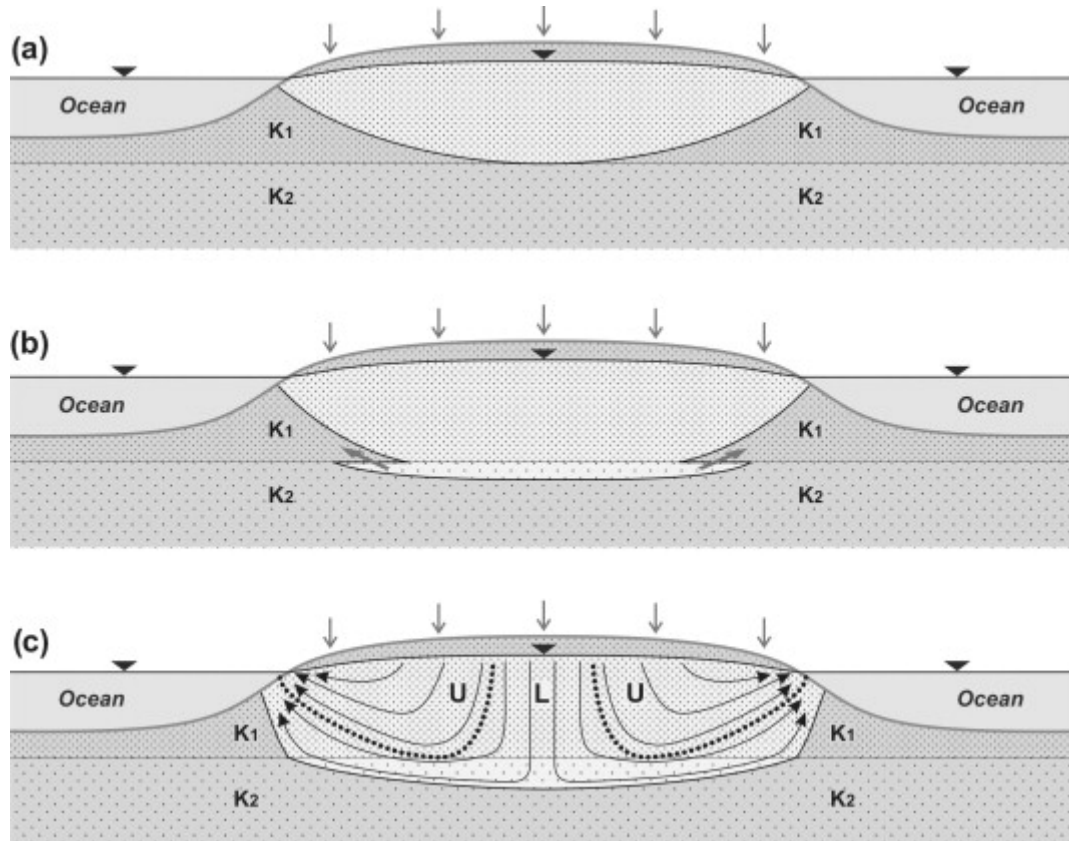
Figure 3-7: Sketch of the transient development of a freshwater lens in a horizontally layered aquifer (Case C, $K_1 < K_2$): (a) lens development in upper layer, (b) interface reaches second, more permeable layer (acceleration), (c) steady-state situation. Dotted lines in (c) separate zones of flow through the upper layer only (U) and both the upper and lower layer (L).

Table 3-3 summarizes the measurements for the four different cases and quantifies variations between the physical and numerical model results. For Case C, the variance between the experiment and the simulation is the highest. The acceleration of the interface when reaching the second layer is not reflected in the numerical simulation using the original parameter set by Dose et al. (2014), obtained from a calibration for steady-state. A mesh refinement at the layer boundary does not improve the fit. Thus, the influence of individual parameters on the transient interface propagation is tested. Compared to the original parameter set, lowering or raising the hydraulic conductivity in one of both layers results in a deeper or shallower penetration of the interface at steady-state, respectively. Still, the acceleration at the boundary between the first and the second layer cannot be reproduced. Changes in dispersivities influence the interface propagation velocity but equally result in different interface depths at steady-state. Keeping the porosity in the upper layer constant, a smaller porosity for the lower layer causes an acceleration of the interface in the second layer but does not influence the final interface depth. A "best fit" simulation of Case C is achieved only by a combination of the changes described above, with dispersivities and porosity for the lower layer having the greatest influence (Table 3-4, Figure 3-6c).

Table 3-3: Comparative quantitative measures of physical and numerical models.

	Unit	Case A	Case B	Case C	Case D
Time to equilibrium (physical) ±10	(min)	136	388	158	257
Maximum depth (physical) ±0.5	(cm)	9.5	20.0	17.0	10.0
Maximum depth (numerical)	(cm)	9.7	19.7	16.4	10.0
Average deviation in final depth (phys.-num.)	(cm)	0.2	0.3	0.6	0.0
Maximum deviation (phys.-num.)	(cm)	0.8	1.5	2.5	0.8
Variance (phys.-num.)	(–)	0.29	0.94	1.58	0.35

Table 3-4: Parameter set of initial and "best fit" model for Case C.

	Initial	Best fit	Unit	Best fit/initial
K_1	0.0018	0.0021	(m s^{-1})	1.17
K_2	0.012	0.012	(m s^{-1})	1
ne_1	0.45	0.45	(–)	1
ne_2	0.41	0.3	(–)	0.73
α_{l1}	0.005	0.01	(m)	2
α_{l2}	0.005	0.001	(m)	0.2
Variance	1.58	0.12	(–)	0.076

Now, both the inflection at the layer boundary and the final depth at steady-state are matched well. A significantly lower variance of 0.12 instead of 1.58 is achieved between the new numerical model and the physical measurement. The adapted lower porosity of the underlying layer can be justified by the additional compaction caused by the backfilling of the overlying sand. This new parameter set, however, might not be unique, as there may be other existing parameter combinations leading to a similar fit.

The steep gradient at the layer boundary in Case C (Figure 3-6c) shows that significant changes in lens thickness can occur over relatively short time spans. The response time of deep permeable layers to changes in recharge is thus small. When taking the propagation velocity

as a proxy, the lower layer dominates the resilience of the system because freshwater stored here is quickly lost.

3.3 Conclusions

The experiments on heterogeneous hydrogeological set-ups for freshwater lenses investigated here show significant deviations from homogeneous models. In both Cases A and B, significant lateral flow and redistribution of water (and contaminants) occurs. These cases also show that on real islands, groundwater divides may not coincide with above-surface geological and hydrological boundaries. At least under the parameters studied here, variations in lateral hydraulic conductivity (Case A) show stronger effects on the flow dynamics (e.g. travel times, shift of water divide and age distribution) than spatial variations in recharge (Case B). An uneven distribution in recharge cannot produce the same difference in freshwater lens thickness as geological variations. A zone of no recharge will receive lateral flow from the recharged zone, but an impermeable layer will obviously prevent lens formation. This has to be considered not only for the delineation of protection zones but also for the allocation of water extraction.

As Cases A and C show, the presence of a layer with high hydraulic conductivity negatively effects the resilience, as these layers lower the overall freshwater lens thickness and respond quicker to changes in recharge. In Case D, the impermeable layer provides a certain protection from up-coning from below since saltwater intrusion may only occur from the sides (provided the freshwater lens has reached the impermeable layer).

The strongest deviations from the homogeneous case of Stoeckl and Houben (2012) were noted for Case C. As configurations like Case C are common in nature, this is important for water management on such islands. Depth specific age dating on coastal zones of these islands may lead to the (at first) puzzling result of younger underlying older water. When interpreting age data obtained from the field, such a heterogeneity in geology and hydrology (i.e. recharge) has to be taken into account (Figure 3-2). For islands, this is the first time that an inversion of the age stratification is postulated. However, field evidence of such a situation has not been documented yet. This also means, that for cases with two layers with highly contrasting hydraulic conductivity, pollutants may be "stuck" in the low conductivity layer while they have been already washed out from the high conductivity layer. The acceleration of the interface upon entering the second, more permeable layer is a feature observed in the physical model, but was initially not reproduced by the numerical simulation with a parameter set that was successfully used for steady-state models. Clearly, without the physical model this would have gone unnoticed. This underlines the importance of physical model experiments for the

investigation of density-driven flow in porous media and the quality control of numerical models. Case D is the closest to the homogeneous case and even the simple analytical models may be used as a first approximation.

Since field cases often show similar heterogeneities as investigated here, both in geological structure and groundwater recharge distribution, homogeneous models (as most analytical models are) are often not sufficient approximations. Numerical models could theoretically address almost any heterogeneity but often the necessary data are not available. Although this study is based on sandtank experiments, its results improve general process understanding. Some of the features which were found through by using physical experiments, e.g. the recharge-dependent age stratification (Case B), have been documented in field studies (e.g. Houben et al., 2014a; Houben et al., 2014b). Others, e.g. the age inversion of Case C, have not been found yet but should be expected due to the commonness of this island geometry. The here presented cases thus provide adequate templates for the definition of conceptual models for heterogeneous real-world island aquifers. A good conceptual model is an indispensable prerequisite for numerical models and for any water resources management strategy.

4 A new numerical benchmark of a freshwater lens

The work of this chapter has been published as: Stoeckl, L., Walther, M., Graf, T. (2016). 'A new numerical benchmark of a freshwater lens'. In: *Water Resources Research* 52(4): 2474–2489.

4.1 Overview of existing variable-density benchmarks

Numerical modeling is a state-of-the-art method to investigate variable-density flow. For model testing, several benchmarks have been developed and are widely used. It is important to note that different benchmarks test different physical aspects of variable-density flow as shown in Table 4-1 (Diersch and Kolditz, 2002). Additionally, Kolditz et al. (2015) have very recently emphasized that benchmarking has become popular to guarantee continuous model quality and ensure correct implementation of new features because model code development is usually spread among many programmers who may be working on different subjects. An overview of benchmarks relevant to variable-density flow in porous media is given below.

Elder (1967) physically and mathematically benchmarked free thermal convection within a closed rectangular box with the dimensions of 0.2 m × 0.05 m. The physical experiment was conducted in a Hele-Shaw cell with a spacing of 4 mm. In this classic Elder problem, a temperature gradient was induced by heating the Hele-Shaw cell from below. The resulting density difference caused a complex pattern of thermal fingering in the aqueous medium. Voss and Souza (1987) defined a solute analogue of the classic thermal Elder problem using the new dimensions of 600 m × 150 m. The assigned constant-concentration boundary conditions induced fluid density differences between 1200 kg m^{-3} (assigned to the center top boundary) and 1000 kg m^{-3} (assigned to the entire bottom boundary), which lead to transient variable-density flow and to solute convection.

Schincariol and Schwartz (1990) physically investigated variable-density flow and mixing in homogeneous and heterogeneous porous media. A tank with the dimensions 1168 mm × 710 mm × 50 mm was used and filled with five different grain sizes to set up experiments in layered, lenticular, and homogeneous media. The inflow of saline water with a higher density (1066.2 kg m^{-3}) than the ambient freshwater (998.3 kg m^{-3}) was applied to the left boundary. Density effects became noticeable when saltwater concentrations exceeded 999.0 kg·m^{-3} in the homogeneous medium. This lead to unstable convective flow patterns and, depending on heterogeneity, resulted in different degrees of dispersion. Schincariol et al. (1994) defined the corresponding numerical benchmark.

Wooding et al. (1997a; 1997b) conducted physical experiments using a Hele-Shaw cell to simulate an evaporating salt lake. The dimensions of the model were 75 mm × 150 mm × 2 mm, with an open left third of the top boundary to enable evaporation. This led to an accumulation of solute and to the formation of dense brine overlying less dense water. The resulting unstable convection was then measured by tracing the development and propagation of salt plumes over time. Simmons et al. (1999) defined the numerical benchmark and numerically simulated the evaporating salt lake experiment by Wooding et al. (1997a; 1997b).

Thorenz et al. (2002) benchmarked saltwater movement in saturated-unsaturated systems. They conducted both, physical experiments and numerical simulations visualizing and investigating density-driven lateral flow patterns above and below a water table. A flow cell with the dimensions 478 mm × 865 mm × 105 mm was filled with sand (with grain diameter between 0.25 mm and 0.50 mm) that was partially saturated with freshwater. Three different cases were considered by varying the heads of the adjacent fresh- and saltwater chambers, so that a saltwater wedge developed different stages of saltwater intrusion. The physical model was equipped with 16 equally spaced ports to allow for tracer injection and sample extraction. The movement of a tracer showed that lateral flow and coupled variable-density flow effects take also place in the partially saturated region above the water table as well as at the interface between the saturated and partially saturated zones. These results were compared to numerical modeling simulations.

Laboratory experiments of variable-density saturated-unsaturated flow and salt transport in a 2D vertical sand tank were conducted by Simmons et al. (2002). Lateral water flow was not considered, and the focus was put on variable-density free convective flow including the generation of dense salt fingers. For visualization, the dense plume was stained with calcium chloride. Cremer and Graf (2015) numerically simulated the saturated experiments with a special focus on finger generation. The unsaturated/saturated experiments by Simmons et al. (2002) are being numerically benchmarked in an ongoing study (Guevara Morel and Graf, submitted).

Oswald (1998) conducted experiments of his so-called 3D saltpool problem, which was further outlined by Oswald and Kinzelbach (2004). The domain of that problem was a fully saturated cube with edge lengths of 20 cm. The initially stable situation was a 6 cm thick saltwater layer overlain by freshwater. Inflow of freshwater and outflow of mixed water at opposite top corners caused a time-dependent up-coning of the saltwater. The gradual dilution of the saltwater layer led to a well-defined breakthrough curve in the discharge water at the outlet of the tank. The experiment was conducted with different initial salt mass fractions in the saltwater layer of 1% and 10%, respectively, demonstrating the effect of density contrasts on the up-coning of the saltwater. Johannsen et al. (2002) numerically benchmarked the 3D

saltpool problem, including a grid convergence study, parameter assessment, and error estimation.

The most applied, but at the same time most controversially discussed benchmark for variable-density flow is the Henry (1964b) problem (Voss and Souza, 1987; Segol, 1994; Buès and Oltean, 2000; Abarca et al., 2007). Simpson and Clement (2003, 2004) clearly showed, that the worthiness of the Henry (1964b) problem is questionable (see Chapter 1.2.2). In addition to the benchmarks listed above, a large number of semi-analytical solutions and numerical simulations describe variable-density flow in porous media (e.g. Weatherill et al., 2004; Voss et al., 2010; Graf and Boufadel, 2011; Fahs et al., 2014). These solutions, however, are not benchmark problems because they are not supported by laboratory experiments.

Freshwater lenses, which are often utilized for drinking water supply, naturally occur under islands worldwide (Vandenbohede and Lebbe, 2002; Bailey et al., 2012; Igel et al., 2013; Röper et al., 2013; Holding and Allen, 2015b). To the authors´ knowledge, no numerical benchmark exists so far accounting for the very unique flow dynamics and mass transport within freshwater lenses. A unique characteristic is the development of a freshwater discharge zone at an inclined beach face rather than a simplified vertical boundary. Also, freshwater recharge from the top (representing rainwater infiltration by a constant-flux boundary condition) is a new feature initially leading to vertical flow dynamics within the freshwater lens rather than a horizontal through-flow as was assumed by Henry (1964b).

Table 4-1: Properties of available physical and associated numerical benchmarks

Physical benchmark	-	Elder (1967)	Elder (1967)	Schincariol and Schwartz (1990)	Wooding et al. (1997a; 1997b)[a]	Simmons et al. (2002)	Thorenz et al. (2002)	Oswald and Kinzelbach (2004)	Stoeckl and Houben (2012)
Numerical benchmark	Henry (1964b)	Elder (1967)	Voss and Souza (1987)	Schincariol et al. (1994)	Simmons et al. (1999)	Guevara Morel and Graf (submitted)	Thorenz et al. (2002)	Johannsen et al. (2002)	**present study**
Dimension L × H × W [m]	60.96 × 30.48 × unity	0.2 × 0.05 × 0.0004	600 × 150 × unity	1.168 × 0.71 × 0.05	0.15 × 0.075 × 0.0002	1200 × 1200 × 0.053	0.865 × 0.478 × 0.105	0.2 × 0.2 × 0.2[b]	0.9 × 0.3 × 0.05
Homogeneous	✓	✓[a]	✓	-	✓	✓	✓	✓	✓
Heterogeneous	-	-	-	✓	-	-	-	-	-
Haline	✓	-	✓	✓	✓	✓	✓	✓	✓
Thermal	-	✓	-	-	-	-	-	-	-
Partially saturated	-	-	-	-	-	✓	✓	-	-
Fingering	-	✓	✓	✓	✓	✓	-	✓	-
Surface-subsurface interaction	-	-	-	-	✓[c]	✓[d]	-	-	✓[e]
Flow dynamics in freshwater lens	-	-	-	-	-	-	-	-	✓
Realistic (sloped) boundary condition	-	-	-	-	-	-	-	-	✓

(a) aqueous medium; **(b)** three-dimensional benchmark; **(c)** evaporation; **(d)** drainage ports; **(e)** recharge and seepage face

4.2 Physical benchmark

Physical experiments of laboratory-scale freshwater lenses were conducted by Stoeckl and Houben (2012). The physical properties and parameters are listed in Table 4-2. Equivalent freshwater conductivity of $K_0 = 4.5 \cdot 10^{-3}$ m s^{-1} was determined by Stoeckl and Houben (2012) using the empirical formula by Beyer and Schweiger (1969) based on a sieve curve analysis and additional Darcy conductivity tests. Following Beyer and Schweiger (1969), total porosity was $n_e = 0.39$. A density meter DMA 38 by Anton Paar, Austria was used by Stoeckl and Houben (2012) to measure the freshwater and saltwater densities of $\rho_0 = 997$ kg m^{-3} and $\rho_s = 1021$ kg m^{-3}, respectively.

Stoeckl and Houben (2012) used an acrylic tank to investigate the formation and degradation of a freshwater lens. The trapezoidal cross-section of an infinite-strip island consisting of sand was initially saturated with saltwater. By recharging freshwater from the top, saltwater was continuously displaced, developing a freshwater lens. To visualize the freshwater lens, fluorescent tracer dyes were added to color the freshwater (Figure 4-1). After around 3.5 h of freshwater recharge, a steady-state flow field established. This steady state was taken as the initial condition for a subsequent experiment, where freshwater recharge was ceased and where the degradation of the lens was observed.
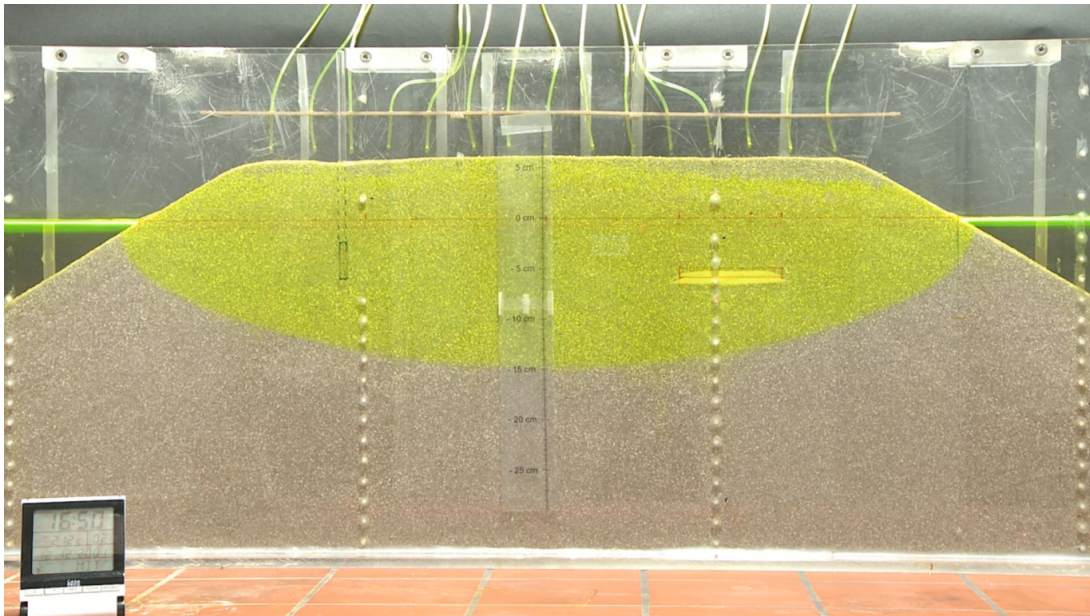
Figure 4-1: Physical experiment of a cross-section of an infinite strip island. Freshwater recharge from the top is colored with the yellow tracer dye Uranine. The colored freshwater lens is surrounded by uncolored saltwater (Stoeckl and Houben, 2012).

Table 4-2: Physical model geometry and uncalibrated parameter set (after Stoeckl and Houben, 2012)

	symbol	value	unit
Model geometry			
Island half width (top)	L	0.4	m
Island half width (bottom)	B	0.9	m
Island height	H	0.3	m
Parameters			
Equivalent freshwater conductivity	K_0	$4.5 \cdot 10^{-3}$	m s^{-1}
Porosity	n_e	0.39	-
Saltwater density	ρ_s	1021	kg m^{-3}
Freshwater density	ρ_0	997	kg m^{-3}
Relative density	β	0.02407**	-
(Relative) salt concentration	c	1*	-
Freshwater recharge rate	R	$1.333 \cdot 10^{-5}$	m s^{-1}

*corresponds to an absolute saltwater concentration of 35 g l^{-1}

**see equation (7) for the definition of relative density β

4.3 Numerical model

4.3.1 Governing Equations

Variable-density flow and transport are simulated using equations (1) to (6) given in Bear (1972). The fluid mass balance for variable-density flow is:

$$\frac{\partial(\rho n_e)}{\partial t} = -\boldsymbol{\nabla} \cdot (\rho \mathbf{q}) \qquad (4.1)$$

where ρ [M L^{-3}] is fluid density, n_e [-] is porosity, t [T] is time, $\boldsymbol{\nabla}$ [L^{-1}] is nabla operator, and $\mathbf{q}$ [L T^{-1}] is Darcy flux calculated by:

$$q = - K_0 I \left(\nabla h_0 + \frac{\rho - \rho_0}{\rho_0} \nabla z \right) \qquad (4.2)$$

where K_0 [L T^{-1}] is equivalent freshwater conductivity, I [-] is the identity matrix, ρ_0 [M L^{-3}] is reference density, z [L] is elevation above datum, and h_0 [L] is equivalent head defined as:

$$h_0 = z + \frac{p}{\rho_0 g} \qquad (4.3)$$

where p [M L^{-1} T^{-2}] is fluid pressure, and g [L T^{-2}] is the gravitational constant. The advective-dispersive transport equation is:

$$\frac{\partial(c n_e)}{\partial t} = - \nabla \cdot (q c) + \nabla \cdot (n_e D \nabla c) \qquad (4.4)$$

where c [-] is relative concentration varying from 0 (freshwater) to 1 (saltwater), and D [L^2 T^{-1}] is the hydrodynamic dispersion tensor defined as (Scheidegger, 1961):

$$n_e D = n_e \tau D_m I + \alpha_t |q| I + (\alpha_l - \alpha_t) \frac{q \cdot q^T}{|q|} \qquad (4.5)$$

where τ [-] is tortuosity, D_m [L^2 T^{-1}] is molecular diffusion coefficient, and α_l [L] and α_t [L] are longitudinal and transverse dispersivity, respectively. A linear relationship between water density ρ [M L^{-3}] and relative concentration c [-] is used:

$$\rho = \rho_0 (1 + \frac{\rho - \rho_0}{\rho_0} c) \qquad (4.6)$$

For the sensitivity study performed later, the relative density β [-] is defined as:

$$\beta = \frac{\rho - \rho_0}{\rho_0} \qquad (4.7)$$

4.3.2 Conceptual model setup

Due to the axially symmetric shape, and to reduce computational cost, half of the laboratory experimental domain is represented in the numerical model. The geometry of the model setup is shown in Figure 4-2, and it has a total height of H = 0.3 m. The extension of the half-island top and bottom are 0.4 m and 0.9 m, respectively. All concentrations are normalized to $0 \le c \le 1$, where c = 0 is freshwater with a salt concentration of 0 g l^{-1} and a density of 997 kg m^{-3}, and c = 1 is saltwater with a concentration of 35 g l^{-1} and a density of 1021 kg m^{-3}. Dispersivity is a scale-dependent

parameter and was adapted according to literature values (Rausch et al., 2005; Rolle et al., 2009; Cupola et al., 2015). Transversal dispersivity is assumed to be in the order of 10% of the longitudinal dispersivity, which is common practice in contaminant hydrogeology.

recharge: $c = 0, q_z = R$ $\forall$ $0 \leq t < T_0$
no recharge: $\partial c / \partial z = 0$, $q_z = 0$ $\forall$ $t \geq T_0$

0.01 m

$h_0 = \frac{\rho}{\rho_0} H - \left(\frac{\rho - \rho_0}{\rho_0}\right) z$ h_s
$c = 1$

$\partial c / \partial x = 0$
$q_x = 0$

$\partial c / \partial z = 0$
$q_z = 0$

$H = 0.3$ m

0.5 m   0.4 m
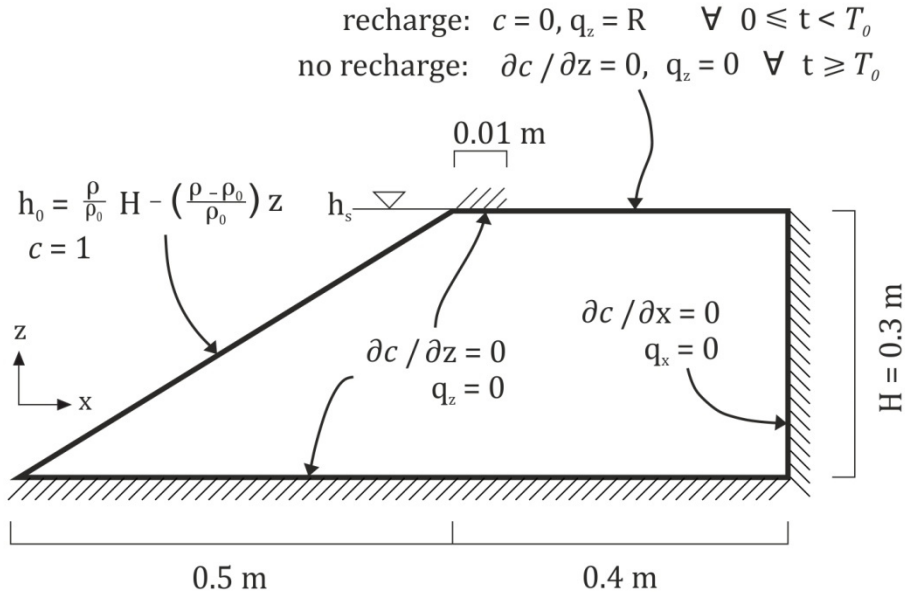
Figure 4-2: Conceptual model and boundary conditions used for the numerical benchmark problem of the freshwater lens.

The boundary conditions (BCs) are shown in Figure 4-2 and are defined as follows: The vertical right boundary (center of the island) and the horizontal bottom boundary are assigned no-flow (Neumann) BCs. The horizontal top boundary is a constant-flow (Neumann) BC for $0 \leq t < T_0$, where T_0 [T] is the time when freshwater recharge is ceased and the second phase (lens degradation) begins.

The constant-concentration (Dirichlet) BC of $c = 0$ is applied to the horizontal top boundary to ensure freshwater recharge into the model. For $t \geq T_0$, this transport BC is modified to a zero-dispersive transport (Neumann) BC. The slope at the left side of the model represents the ocean, which is simulated by a constant-head (Dirichlet) BC for flow together with a constant-concentration (Dirichlet) BC for transport of $c = 1$.

The first six nodes adjacent to the upper left corner of the horizontal boundary (a stretch of around 1 cm) are set to no-flow and zero-dispersive transport (Neumann) BCs at all times. This corresponds to the experimental set-up, where freshwater recharge drippers are not placed directly at the shore-line. As flow velocities and concentration gradients are large in the outflow zone, the 1 cm stretch also prevents numerical instabilities by

50

separating the constant transport BC of c = 1 from the constant transport BC of c = 0, as well as the Dirichlet flow BC and the Neumann flow BC at the slope and the top, respectively. The initial condition for the simulation is a fully saturated domain with the saltwater concentration of c = 1.

The finite element model Feflow Diersch (2014) was used for the numerical simulations. The solver type for inverting the discretized flow (symmetric) and transport (asymmetric) equations were the biconjugate gradient stabilized method (BiCGStab) and the preconditioned conjugate gradient method (PCG), respectively. A linearly convergent algorithm (Picard iteration scheme) was used to linearize the non-linear problem. The temporal weighting scheme was chosen to be fully implicit. The result is post-processed using the visualization software ParaView (Henderson, 2007), which is an open-source, scientific visualization toolbox.

4.4 Uncertainty analysis

A grid convergence study and error analysis similar to (Graf and Degener, 2011) was carried out in order to determine the necessary discretization level in space and time.

4.4.1 Spatial discretization

A uniform triangular grid was constructed using the mesh generator Triangle[©] (Shewchuk, 1996). The coarsest grid level $\sigma = 0$ is defined by dividing the model domain into 3 elements with an average element size of around 512 mm. Increasing the spatial discretization level σ ($\sigma = 0,1,\ldots,9$) corresponds to dividing the average element size by two, such that the element size at level σ is given by:

$$\Delta x(\sigma) = \frac{512}{2^\sigma} \text{ mm} \tag{4.8}$$

4.4.2 Temporal discretization

A uniform time-stepping scheme was used for the discretization in time. Similar to the spatial discretization level, an incrementally increasing of the temporal discretization level θ ($\theta = 0,1,\ldots,4$) corresponds to dividing the time-step size by two, given by:

$$\Delta t(\theta) = \frac{138.24}{2^\theta} \text{ s} \tag{4.9}$$

where a time-step size of 138.24 s is defined at the temporal discretization level $\theta = 0$.

4.4.3 Convergence test

Simulations with increasing spatial and temporal discretization levels were carried out. To verify convergence, the time-dependent depth of the 0.5 concentration contour at the right vertical boundary (center of the island) was used as the representative quantity because it was measured in the physical experiment. The 0.5 concentration contour depths $f_{\sigma,\theta}$ (normalized to the maximum contour depth of $\frac{H}{2} = 150$ mm) is denoted using the first 15 values at equally spaced time intervals of $\Delta t = 864$ s (until steady-state) at 864 s, 2·864 s, ..., 15·864 s by $f_{\sigma,\theta}^{864}, f_{\sigma,\theta}^{2\cdot864}, \dots, f_{\sigma,\theta}^{15\cdot864}$, and define:

$$f_{\sigma,\theta} := 864 \begin{Bmatrix} f_{\sigma,\theta} \\ f_{\sigma,\theta}^{2\cdot} \\ \vdots \\ f_{\sigma,\theta}^{15\cdot} \end{Bmatrix} \in \mathbb{R}^{15} \tag{4.10}$$

The L_2-norm is used to estimate the dimensionless relative spatial and temporal discretization errors $r_{\sigma+1/2,\theta}$ and $r_{\sigma,\theta+1/2}$ between solutions corresponding to increasing spatial and temporal discretization levels, respectively (Johannsen et al., 2002):

$$r_{\sigma+1/2,\theta} = \frac{||f_{\sigma+1,\theta} - f_{\sigma,\theta}||_2}{||f_{\sigma,\theta}||_2} \tag{4.11}$$

$$r_{\sigma,\theta+1/2} = \frac{||f_{\sigma,\theta+1} - f_{\sigma,\theta}||_2}{||f_{\sigma,\theta}||_2} \tag{4.12}$$

Convergence in space and time is defined to be reached if the relative errors drop below 0.001 (1‰), similar to Graf and Degener (2011).

Figure 4-3 shows the spatial and temporal discretization errors, indicating that errors are not oscillating and that an increasing discretization level in both, space (σ) and time (θ), leads to decreasing discretization errors. Grid convergence is achieved for the spatial discretization level $\sigma = 9$ and the temporal disretization level $\theta = 4$.

Figure 4-3: Evaluation of the sensitivity of spatial and temporal discretization in the L_2-norm. Errors between spatial (aligned horizontally) and temporal (aligned vertically) discretization levels are calculated with Eq. (11) and Eq. (12), respectively. The grid used for $f_{9,4}$ is the spatial and temporal discretization level, for which convergence is reached (underlined).

The grid of $f_{9,4}$ consists of 241,400 elements and 212,362 nodes with an average triangular element size of 1 mm. Uniform time-step size is 8.64 s. The grid Peclet number Pe_g (grid spacing/dispersivity) is 0.2, using the value of 5 mm for the longitudinal dispersivity (Table 4-2). This satisfies the widely accepted criterion for neglecting numerical dispersion as well as oscillations, $Pe_g \leq 2$ (Kinzelbach and Rausch, 1995). Under- or overshooting of concentrations within the model domain get smaller with higher discretization level. They are negligible for the selected grid $f_{9,4}$ (in the range of 1% of the initial concentrations). The overall model performance is observed to be stable.

The goodness of fit between the observed and measured position of the 0.5 concentration contour over time at the vertical boundary is expressed by the Nash-Sutcliffe efficiency E. This efficiency can vary between $-\infty$ and 1, where 1 indicates exact accordance (Nash and Sutcliffe, 1970). With the uncalibrated parameter set from Table 4-2, an efficiency of 0.98 was achieved between the numerical simulation and the observation in the physical experiment, indicating a high degree of matching.

4.4.4 Sensitivity analysis

A sensitivity analysis is conducted here in order to identify a) the influence of parameter uncertainty on the simulation results and b) to figure out which parameters need to be subject to a subsequent parameter estimation using PEST (see Chapter 4.5 Parameter fitting). This was done by varying the value of a selected parameter by ±20% while keeping all other parameters unchanged (Table 4-3).

Table 4-3: Parameter variations for the sensitivity analysis

	-20%	original	+20%
Porosity n_e [-]	0.312	0.390	0.468
Hydraulic conductivity K_0 [m s^{-1}]	0.0036	0.0045	0.0054
Relative density β [-]	0.01926	0.02407	0.02888
Longitudinal dispersivity α_l [m]	$4 \cdot 10^{-4}$	$5 \cdot 10^{-4}$	$6 \cdot 10^{-4}$
Molecular diffusion D_m [m² s^{-1}]	$8.0 \cdot 10^{-10}$	$1.0 \cdot 10^{-9}$	$1.2 \cdot 10^{-9}$
Specific storage S_s [m^{-1}]	$8.0 \cdot 10^{-5}$	$1.0 \cdot 10^{-4}$	$1.2 \cdot 10^{-4}$

Sensitivities are visualized in Figure 4-4 by comparing the propagation of the 0.5 concentration contour at the vertical (right) boundary with parameters varied by ±20%. Variations in the porosity affect flow velocities, with lower porosity values resulting in larger velocities and a faster downwards movement of the contour as shown in Figure 4-4. The steady-state depth of the 0.5 concentration contour at the end of the recharge phase is unaffected by porosity uncertainty. Hydraulic conductivity leads to a vertical displacement of the interface position, indicating a lower penetration depth of the 0.5 concentration contour for higher K_0 values during both the formation and the degradation phase. At steady-state, the saltwater-freshwater interface position is determined by the freshwater head above sea level (Herzberg, 1901), which depends on the hydraulic conductivity as described in Henry (1964a) and Fetter (1972). The freshwater lens thickness is therefore larger for smaller hydraulic conductivities as shown before (Vacher, 1988) and as indicated in Figure 4-4. Similar to porosity and hydraulic conductivity, the relative density β was found to be a sensitive parameter. A larger relative density leads to a shallower lens at steady-state, because a greater equivalent freshwater volume (driven by freshwater recharge in this case), would be necessary to displace the same amount of saltwater, following the principle of Badon-Ghyben (1888) and Herzberg (1901).

Therefore, freshwater is displaced faster when a higher relative density is applied as shown in Figure 4-4.

Uncertainty of dispersivity and molecular diffusion hardly show any effect on the modeling results because these parameters influence the width of the mixing zone rather than the position of the 0.5 concentration contour. Uncertainty of specific storage does not affect variable-density flow if the specific storage value is smaller than 10^{-3} m^{-1} (Xie et al., 2014).
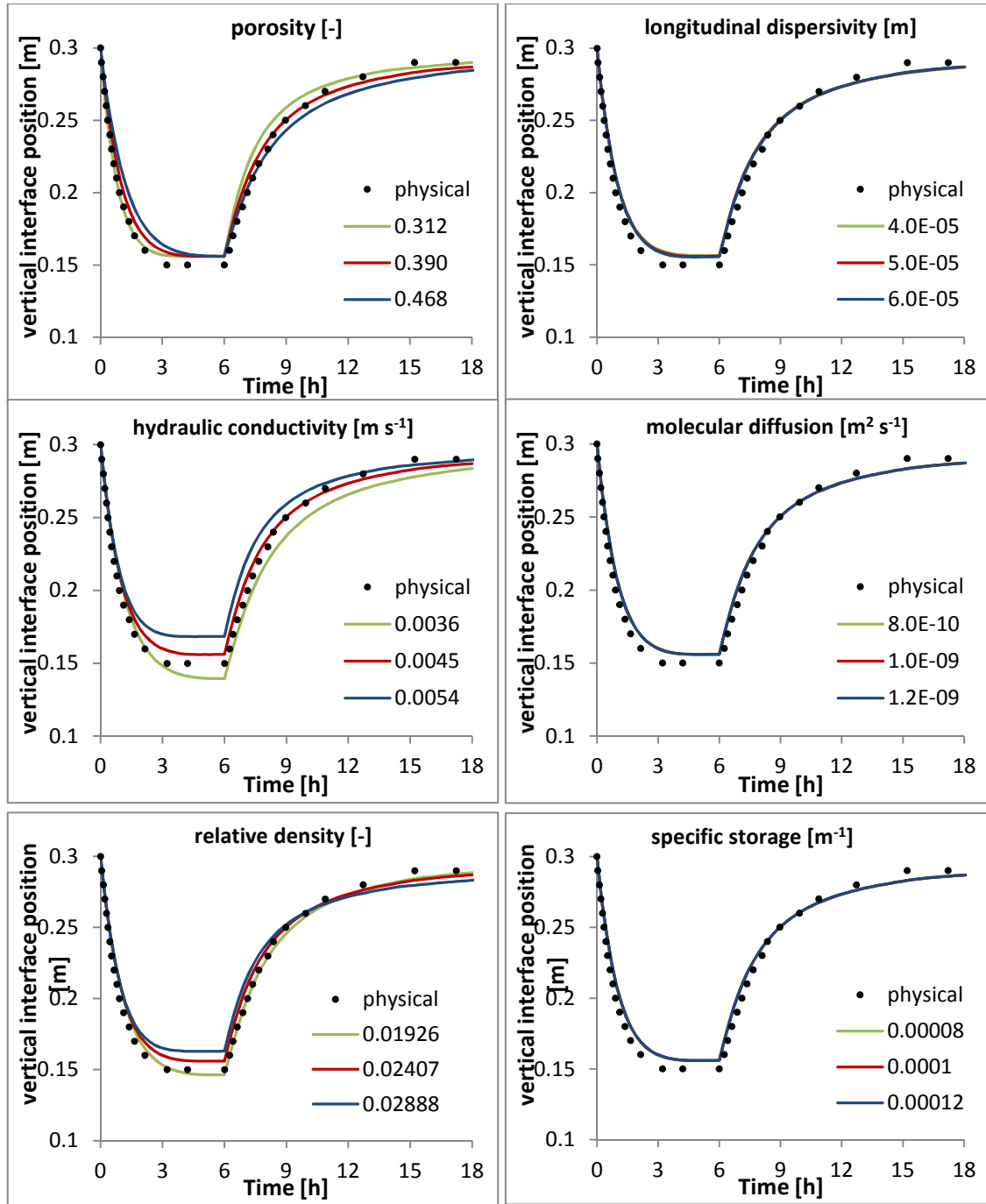
Figure 4-4: Effects of parameter uncertainty on the formation and degradation of a freshwater lens.

4.4.5 Parameter fitting

A nonlinear parameter estimation was conducted using the software PEST (Doherty et al., 1994) in order to find the optimal set of parameters to fit the physical results of the 0.5 concentration contour over time at the vertical boundary. PEST determines the optimal parameter values, such that the numerical simulation result best represents

experimental observations. Porosity, hydraulic conductivity and relative density were considered for the fitting, as they were determined to be the most sensitive controls of variable-density flow in a freshwater lens. A maximum allowed variations of ±10% for hydraulic conductivity and porosity, and ±5% for the relative density were defined with respect to the original values determined by Stoeckl and Houben (2012). This is in agreement with Stoeckl and Houben (2012), because density could be measured more accurately in the laboratory than hydraulic conductivity and porosity.

According to the measurements of the 0.5 concentration contour depth by Stoeckl and Houben (2012), 15 calibration points at elevations of 0.29 m, 0.28 m, …, 0.15 m were defined along the right vertical boundary. One additional calibration point was defined at an elevation of 0.12 m, which was observed to contain saltwater throughout the entire experiment. All time-depth specific measurements of the 0.5 concentration contour by Stoeckl and Houben (2012) were included in the PEST calibration, as well as 11 additional measurements of relative concentrations of 0 and 1, which could clearly be determined to be freshwater and saltwater, respectively. In total, 41 measurements at the 16 observation points were used for calibration. Because the majority of measurements are available during lens formation and degradation, measurements at steady-state are underrepresented. Therefore, two observations of the 0.5 concentration contour (at the end of the formation phase and degradation phase, respectively) were given a weight five times higher in order to more realistically represent the steady-state.

The optimal parameter set determined by PEST slightly differs from the uncalibrated values given in Table 4-2. Calibrated parameter values and their corresponding limits of the 95% confidence intervals are: hydraulic conductivity = $4.17 \cdot 10^{-3}$ m s^{-1} ($\pm 0.16 \cdot 10^{-3}$ m s^{-1}), porosity = 0.35 (± 0.02), and relative density = 0.02287 (± 0.00167). Figure 4-5 compares the physical results by Stoeckl and Houben (2012) with the numerically simulated results using the uncalibrated and the calibrated parameter sets. Results clearly show that the uncalibrated model simulates the experimental results within the given errors, and that the calibrated model is in excellent agreement with the experimental results.
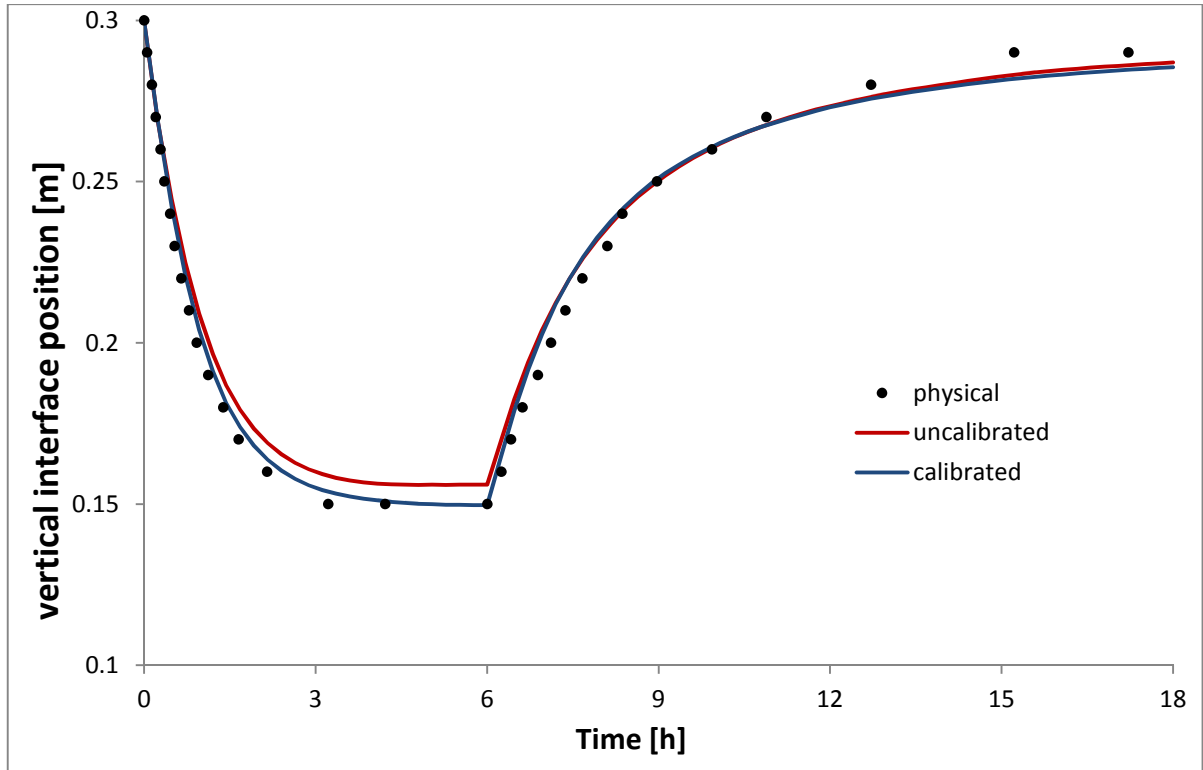
Figure 4-5: Results of the parameter fitting with PEST. Black dots represent physical measurements while the red and blue line show the numerical simulation results using the uncalibrated parameter set and the parameter set determined by the PEST calibration, respectively.

4.4.6 Worthiness of the new benchmark

The worthiness of the freshwater lens benchmark newly introduced here was tested by comparing a density-coupled with a density-uncoupled model using Feflow. As described by Simpson and Clement (2003), density uncoupling was achieved by setting the relative density β to zero. The 1st type constant-head BCs remain unchanged, i.e. the same equivalent freshwater heads representing a saltwater column are applied. Thus, as the defined piezometric head at this boundary increases with depth, salt water enters the model domain from the lower part of the sloping boundary and forces the discharging freshwater to move upwards. This can be observed in both, the Henry problem (Simpson and Clement, 2003) and in the present freshwater lens benchmark (Figure 4-6).

Figure 4-6 compares concentration contours of the density-coupled with those of the density-uncoupled modeling results at steady state. The positions of the contours very clearly change from an overall horizontal (density-coupled) to overall vertical (density-uncoupled) orientation. Interestingly, the position of the freshwater-saltwater interface close to the outflow zone as well as the width of the outflow zone at the beach remain unchanged because the BC remains unchanged here. The substantial difference in the

contour orientation clearly indicates that density-coupling has a very significant influence on the simulation results, and that the new benchmark presented here is worthy to adequately describe island flow physics largely controlled by density effects. The results presented in Figure 4-6 also demonstrate that the variable-density flow physics of the new freshwater lens benchmark is not controlled by applied BCs (as is the case in the Henry problem) but by the naturally occurring physical flow dynamics of the freshwater lens.
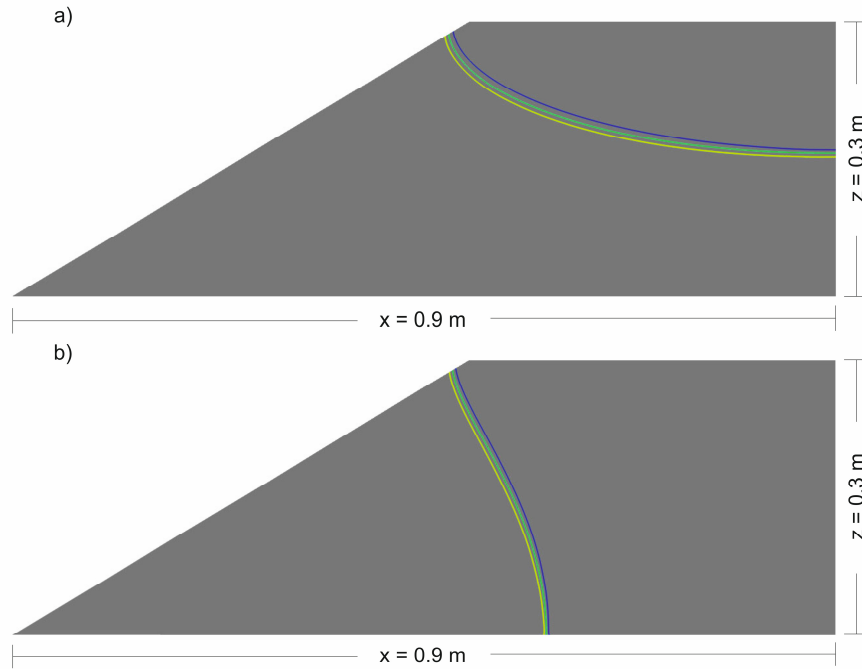
Figure 4-6: Model results of the freshwater lens benchmark at steady-state: (a) density-coupled versus (b) density-uncoupled scenarios. The freshwater-saltwater interface is displayed by the yellow, green, and blue lines representing relative saltwater concentrations of 0.75, 0.5, and 0.25, respectively.

4.5 Definition and phenomena of the new numerical benchmark

4.5.1 Steady-state phenomena

In Figure 4-7, the salinity distribution are shown at full steady-state development of the freshwater lens for the physical (top) and numerical (bottom) simulation, using the calibrated parameter set. The numerical results show the salinity distribution between freshwater and saltwater. The freshwater-saltwater interface (white zone of the numerically simulated salt distribution) is small compared to the areas of the freshwater

above and of the saltwater below it and displays the interface in the physical model. It can be noticed that the width of the freshwater-saltwater interface is very small, similar to the experimental observation. The freshwater outflow zone at steady-state is also accurately represented by the numerical model: The distance between the left upper corner of the model and the 0.5 concentration isoline intersecting the sloping boundary is 2.9 cm.
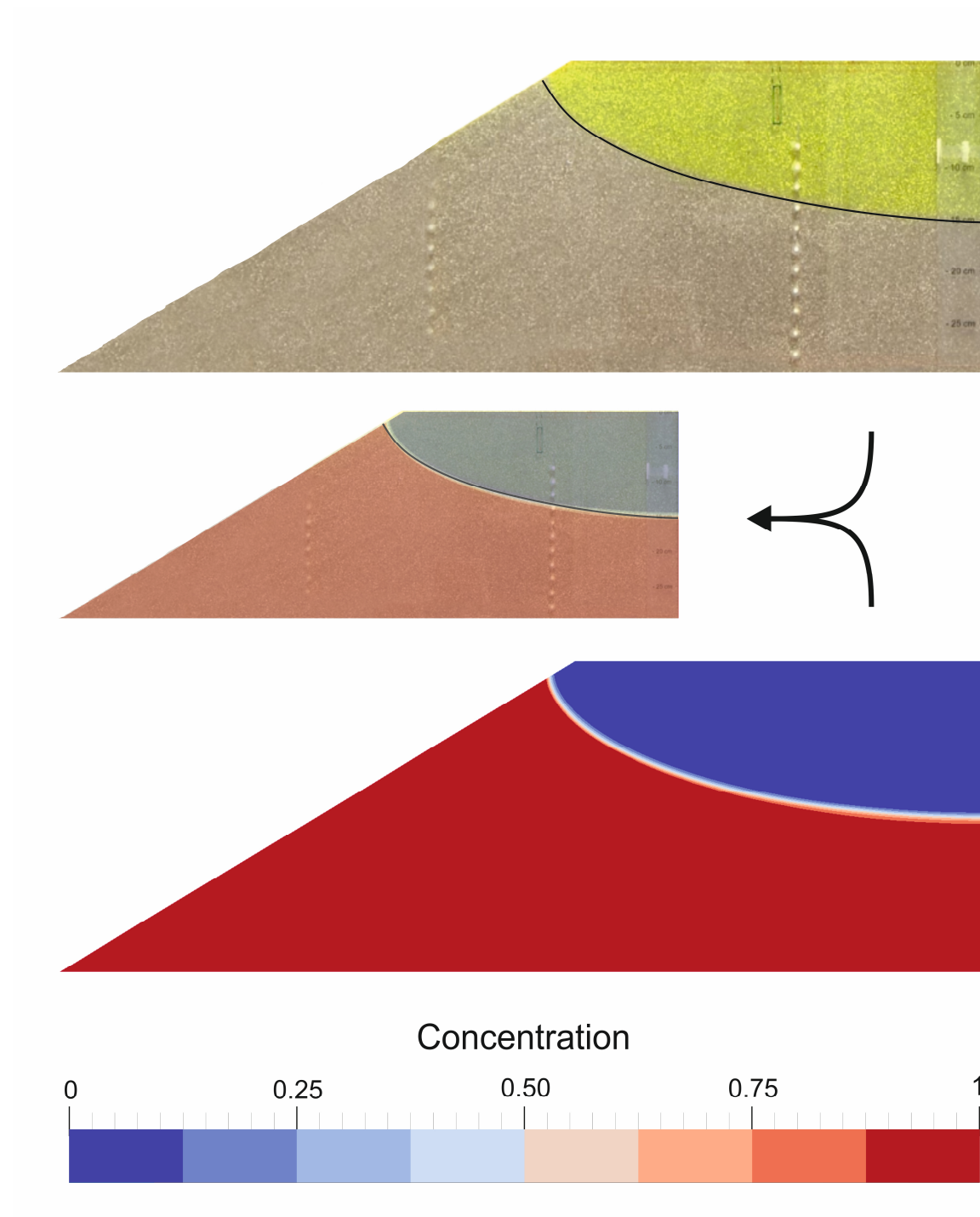
Figure 4-7: Physical experiment (top) and numerical simulation (bottom) showing the fully developed freshwater lens at steady-state. The small inlet figure is an overlay of both results. In the physical model,

freshwater is yellow while saltwater remained uncolored (Stoeckl and Houben, 2012). The numerical simulation shows the salinity distribution between freshwater (blue, c = 0) and saltwater (red, c = 1).

In Figure 4-8, flow directions are shown at steady-state by areas of similar flow angles γ against the negative x-axis. The black lines in Figure 4-8 represent the 0.1, 0.5, and 0.9 concentration contours from top to bottom. Within the lens, flow directions are predominantly horizontal, indicating flow from the right (vertical boundary) to the left (outflow zone), as visualized by the yellow color. Similarly, saltwater enters the domain through the inclined boundary at the left side with an angle of γ ≈ 240° (dark blue color). That saltwater flow then turns to horizontal flow (γ ≈ 180°, purple/violet), bends upwards and eventually converges with the freshwater recharge from the top (γ ≈ 100°, red/orange). In Figure 4-8 this is further illustrated by the gray streamlines for fresh- and saltwater flow, starting from the top and inclined boundary, respectively. After the fluxes of fresh- and saltwater have unified, flow directions turn towards the outflow zone with an angle of 350° < γ < 10° (yellow area between the black concentration contours). Below the 0.9 concentration contour, the color changes from orange/red to yellow, indicating an abrupt shift in flow directions. This change in flow direction is thus directly related to the salinity and reveals a new finding: As soon as saltwater gets diluted by a small fraction of freshwater, flow directions are altered and turn towards the outflow zone. This mechanism determines the freshwater-saltwater interface position, caused by the differences in buoyancy between fresh- and saltwater. At the outflow zones, discharge is forced to bend upwards γ < 90° indicated by the orange color.
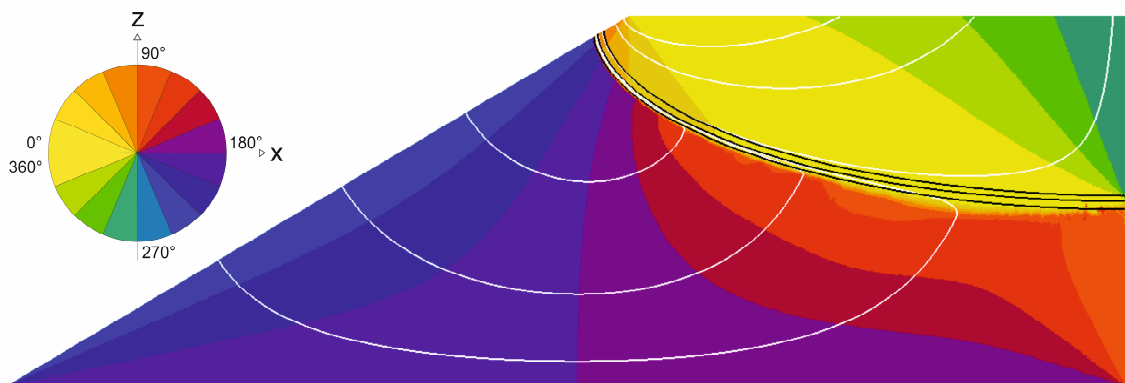
Figure 4-8: Numerically simulated angles of flow direction at steady-state with respect to the horizontal direction from right to left (0°). The black lines represent the 0.1, 0.5, 0.9 concentration contour from top to bottom, while streamlines are illustrated in gray.

4.5.2 Transient phenomena

The 0.5 concentration contour at the vertical boundary was measured during the formation phase I (with freshwater recharge) and the degradation phase II (no freshwater recharge) of the freshwater lens. The transient interface propagation over time in the physical experiment from Stoeckl and Houben (2012) and numerical simulation results with the calibrated parameter set described above are displayed in Figure 4-5. It is shown that the formation of the lens takes around 4 h to reach equilibrium with a maximum interface position of around 15 cm. The degradation phase starts after 6 h. After around 18 h, the freshwater is displaced by the saltwater, and the interface almost reached the top of the island.

The development of the interface width during freshwater lens formation and degradation is shown in Figure 4-9. The interface width is defined as the distance between the freshwater concentration contour c = 0.1 and the saltwater concentration contour c = 0.9 along the vertical right boundary of the model. During freshwater lens formation, the fast widening of the interface is followed by a decrease of interface width until steady-state is reached after 12 h. This process of attaining steady-state takes much longer for the width of the interface than for the position of the 0.5 concentration contour (Figure 4-5). The degradation phase was initiated by turning off freshwater recharge at $T_o = 12$ h and is characterized by a second widening of the freshwater-saltwater interface with a subsequent decrease of the interface width. This second peak visualized in Figure 4-9 shows a greater interface width of 6.7 cm compared to the first peak of 5.7 cm during lens formation. However, the second peak is sharper than the first one when considering the steady-state interface width of 1.6 cm. This behavior can be explained by smaller flow velocities after freshwater recharge was ceased. Measurements were stopped after around 22 h, when the 0.1 concentration contour disappeared and the remaining water had a concentration of $c \geq 0.1$.
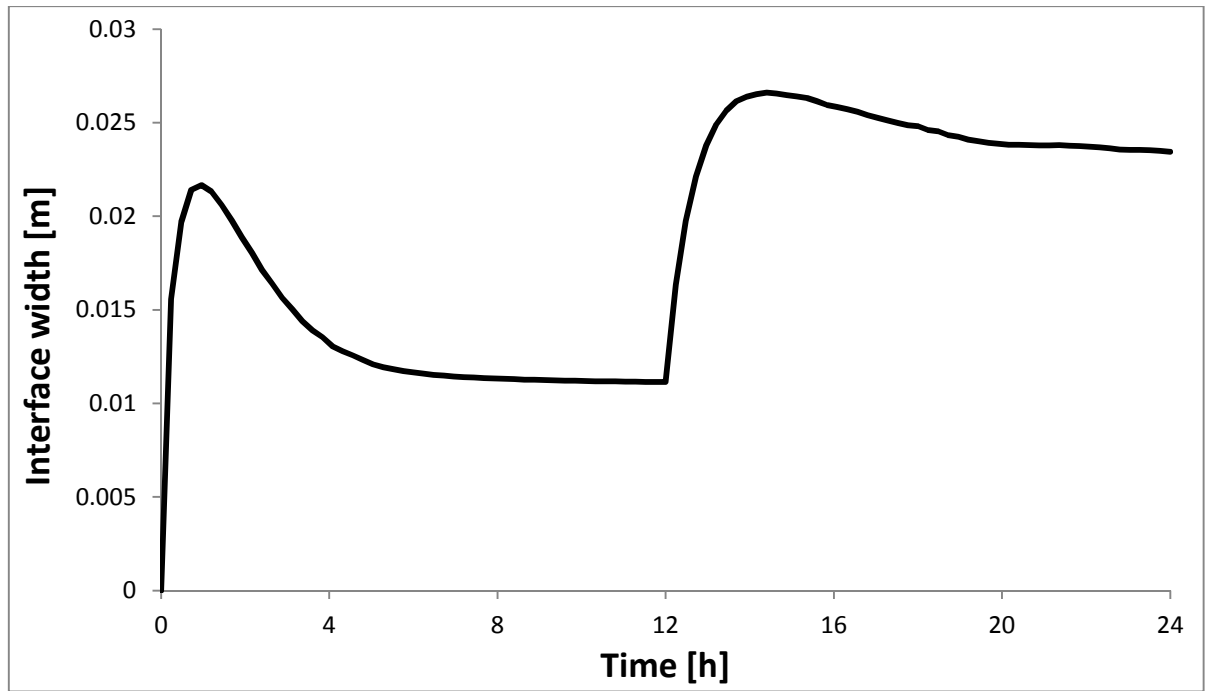
Figure 4-9: Development of the interface width during freshwater lens formation and degradation

4.5.3 Definition of the new freshwater lens benchmark

The complete definition of the new numerical freshwater lens benchmark is given in order to enable future code testing for freshwater lens investigations. A clear progress in benchmarking compared to previous existing studies is the presentation of both, steady-state and transient density dependent results. This new benchmark of freshwater lens flow dynamics is therefore defined by:

- The model geometry displayed in Figure 4-2.
- The spatial grid with 241,400 triangular elements and 121,362 nodes (Section 4.2). The lens.vtu file with the detailed mesh geometry is available as supplementary material.
- The constant time-step size of 8.64 s.
- The complete parameter set shown in Table 4-4, which are a) adapted from Stoeckl and Houben (2012) b) determined by the PEST calibration, and c) derived from the literature.

Table 4-4: Complete parameter set of the new freshwater lens benchmark

Parameters	source*	symbol	value	unit
Freshwater recharge rate	a	R	$1.333 \cdot 10^{-5}$	m s^{-1}
Freshwater density	a	ρ_0	997	kg m^{-3}
Relative densities	b	β	0. 02287	-
Equivalent freshwater conductivity	b	K_0	$4.1 \cdot 10^{-3}$	m s^{-1}
Porosity	b	n_e	0.35	-
Longitudinal dispersivity	c	α_l	$5 \cdot 10^{-4}$	m
Transversal dispersivity	c	α_t	$5 \cdot 10^{-5}$	m
Molecular diffusion coefficient	c	D_m	10^{-9}	m² s^{-1}
Specific storage (compressibility)	c	S_s	$8 \cdot 10^{-5}$	m^{-1}
Gravitational acceleration	c	g	9.81	m s^{-2}
Dynamic viscosity	c	μ	$1 \cdot 10^{-3}$	kg m^{-1} s^{-1}

*a) from Stoeckl and Houben (2012); b) from the PEST calibration; c) from literature

The model output for benchmarking is therefore defined by:

- The salinity distribution inside the domain when the freshwater lens is at steady-state after recharge is established (Figure 4-7).
- The flow directions of velocity vectors at steady-state, visualized by angles γ in respect to the horizontal vector from right to left (Figure 4-8).
- The propagation of the 0.5 concentration contour along the vertical (right) boundary over time (Figure 4-5).
- The development of the interface width during freshwater lens formation and degradation (Figure 4-9).

The steady-state results are provided as supplementary material to support independent benchmarking activities (see file "lens.vtu"). The data format of the supplementary material follows the framework of the open-source Visualization ToolKit (VTK, http://www.vtk.org/Wiki/VTK), which is standard in visualization science (Bilke et al., 2014; Fischer et al., 2015). Since VTK is a standard ASCII format, it can be read by the open-source software ParaView (Henderson, 2007), or by employing individual

implementations of the rich processing filters of the well-documented VTK data format framework.

4.6 Summary and conclusion

A new numerical benchmark of a developing and degrading freshwater lens is introduced here. This benchmark is based on physical measurements (Stoeckl and Houben, 2012) and represents an alternative to the well-known and widely applied Henry (1964b) saltwater intrusion problem. The Henry problem was so far the only benchmark explicitly dealing with saltwater intrusion, but as shown earlier, its worthiness regarding the representation of density effects is questionable (Simpson and Clement, 2003, 2004).

The worthiness of the new freshwater lens benchmark was shown by comparing density-coupled and density-uncoupled model results. Results show significant differences leading to the conclusion that density variations are important for correctly simulating this benchmark. A grid convergence study was carried out in order to determine the required spatial and temporal discretization for the numerical simulations. A threshold discretization error of 1‰ was reached using an average cell size of 1 mm and a discrete time-step size of 8.64 s. Parameter sensitivities were determined by varying single parameters. Sensitive parameters are the hydraulic conductivity, porosity, and relative density. Variations in dispersivity, molecular diffusion, and specific storage coefficient do not affect the flow dynamics in a freshwater lens.

The numerical benchmark of variable-density flow in a freshwater lens is defined, and a calibrated parameter set was determined using the PEST software package for model calibration. Numerically determined salinity distributions at steady-state as well as the transient propagation of the 0.5 concentration contour at the vertical boundary are identical with the results from the physical benchmark by Stoeckl and Houben (2012). The distribution of angles of flow directions at steady-state as well as the transient development of the interface width along the vertical boundary are additional quantities for code comparison. Even though these quantities are not physically measurable, they are valuable information for interpreting flow physics of a freshwater lens and for identifying changes between different codes. Thus, a great variety of model output in steady-state and transience is now available for benchmarking variable-density flow and solute transport of a freshwater lens in order to ensure the correct implementation of variable-density flow equations and to validate different numerical codes that simulate flow in a freshwater lens. A comparison of four additional numerical model codes to the freshwater lens benchmark calculations with Feflow is part of a subsequent study,

intended to be published in the near future. This future model comparison will a) give a stronger basis for the results that cannot directly be compared to the physical experiment, and b) will explore the range of deviations that have to be expected when using state-of-the-art codes for modeling variable-density flow and solute transport processes.

5 Application of the freshwater lens benchmark to five different numerical model codes

The work of this chapter is in preparation for being submitted as: Stoeckl, L., Walther, M., Schneider, A., Yang, J., Graf, T. (in prep.). 'Numerical code comparison using the new variable-density flow and solute transport benchmark of a freshwater lens'.

5.1 Methodology

A great variety of modeling software is available nowadays, capable of solving differential equations of groundwater flow and processes of solute transport. Open source or commercial packages, elaborated by individual researchers or a group of developers including finite difference, finite element, and finite volume methods can be encountered. Benchmarks are a common way to ensure correct implementation of the relevant processes. Furthermore, from the diversity of the various available tools, the accuracy of modeling results should be compared: different initiatives (Kolditz et al., 2015) benchmarking subsurface flow with focus on reactive transport processes) work on comparing certain codes, setting up standards for the future use of benchmarks. However, some benchmark set-ups are not available for recalculations and to compare other codes with (e.g. Maxwell et al. (2014) benchmarking coupled surface- and groundwater flow), whereas other benchmarks can not sufficiently be parameterized with only one code (e.g. Stoeckl et al., 2016 using Feflow to benchmark a variable-density flow and solute transport processes of a freshwater lens). Regarding variable-density flow and solute transport, only a limited number of benchmarks is available at the moment. Additionally, many benchmarks lack physical model equivalents (Stoeckl et al., 2016). To show the applicability and advantages of the physically based freshwater lens benchmark, a comparison of five different models is performed here, providing additional insight into model codes, as well as an overview of the diversity, i.e. numerically caused deviations and accordance in model results.

The five different numerical model codes used for this work are: Distributed Density Driven Flow (d³f, Fein and Schneider, 1999), Feflow (Diersch, 2014), HydroGeoSphere (HGS, Therrien, 2007), OpenGeoSys (OGS, Kolditz et al., 2015), and Spring (König et al., 2012). All codes have proven their capabilities to simulate variable-density flow and have been utilized in various studies on different scales (e.g. Beinhorn et al., 2005;

Shankar et al., 2009; Flügge, 2013; Yang et al., 2013; Dose et al., 2014; Walther M., 2014).

The freshwater lens benchmark used for comparison is described in detail in Stoeckl et al. (2016). The conceptual model reflects half a freshwater lens in a saline aquifer (Figure 4-2). As to reveal even small variations in the different model codes, initial and boundary conditions as well as geometric parameters, and material constants were kept identical or as similar as possible: the same mesh was imported by all modeling software (mesh.msh available as supplementary material). The same parameters set was applied to every model (Table 5-1), which slightly deviates from the parameter set listed in Stoeckl at al. (2016) because the numerical benchmark by Stoeckl at al. (2016) was slightly modified after the comparison had been elaborated. E.g. the values for longitudinal and transversal dispersivity were deliberately chosen one order of magnitude greater than the respective parameter-set obtained by the Pest calibration. This resulted in a broader interface and more pronounced deviations in the output of the different models which are of major interest here.

To exclude deviations resulting from insufficient spatial or temporal discretization, a constant time stepping scheme of 8.64 s was used as identified to be suitable and within an error tolerance of 0.01 defined in Stoeckl et al. (2016). Consistency in post-processing software using ParaView (Henderson, 2007) ensures maximum comparability by preventing deviations from rounding errors.

Table 5-1: Complete parameter set of the new freshwater lens benchmark

Parameters	symbol	value	unit
Freshwater recharge rate	R	$1.333 \cdot 10^{-5}$	m s^{-1}
Freshwater density	ρ_0	997	kg m^{-3}
Relative densities	β	0. 02407	-
Equivalnt hydraulic conductivity	K_0	$4.5 \cdot 10^{-3}$	m s^{-1}
Effective Porosity	n_e	0.35	-
Longitudinal dispersivity	α_l	$5 \cdot 10^{-3}$	m
Transversal dispersivity	α_t	$5 \cdot 10^{-4}$	m
Molecular diffusion coefficient	D_m	10^{-9}	m² s^{-1}
Specific storage (compressibility)	S_s	$1 \cdot 10^{-4}$	m^{-1}
Gravitational acceleration	g	9.81	m s^{-2}
Dynamic viscosity	μ	$1 \cdot 10^{-3}$	kg m^{-1} s^{-1}

5.2 Results

Firstly, steady-state results of salinity distributions and flow directions for the different modeling tools are shown. Secondly, transient propagation of concentration contours and saltwater-freshwater interface properties during lens formation and degradation are compared to physical experimental results by Stoeckl and Houben (2012).

5.2.1 Steady-state salinity distributions

Figure 5-1 shows the salinity distribution of the physical and the five numerical models at steady-state. Results of all numerical models indicate a high similarity to results of the physical model, i.e. the orientation of the freshwater-saltwater interface and the amount of freshwater versus saltwater in the model. More subtle, the different models also show minor deviations in the saltwater-freshwater transition zone. This zone is defined as the width of the saltwater-freshwater interface between salinities $0.1 < c < 0.9$. In the physical model, a rather sharp interface is observed, similar to the benchmark given in

Stoeckl et al. (2016). Here, a broader interface and thus a greater observational accuracy is obtained by choosing greater values for longitudinal and transversal dispersivity, as mentioned before.

The interfaces in the simulations by d^3f, Feflow and Spring are generally narrow (around 1.6 cm at the vertical boundary). Simulation results by OGS show a thicker interface, especially at the vertical no-flow BC. Salinity distributions obtained by HGS indicate a thicker interface close to the outflow zone compared to the other simulations. The models by d^3f and Feflow are able to properly represent the transport BC by the implementation of a "constraint". The constraint was also implemented into and HGS and OGS during this study. In Spring, the transport BC is not converted when water leaves the model domain, which causes the interface to bend upwards at the outflow zone. However, this only leads to small deviations in the vicinity of the outflow zone, while salinity distributions elsewhere equal those of Feflow and d^3f.
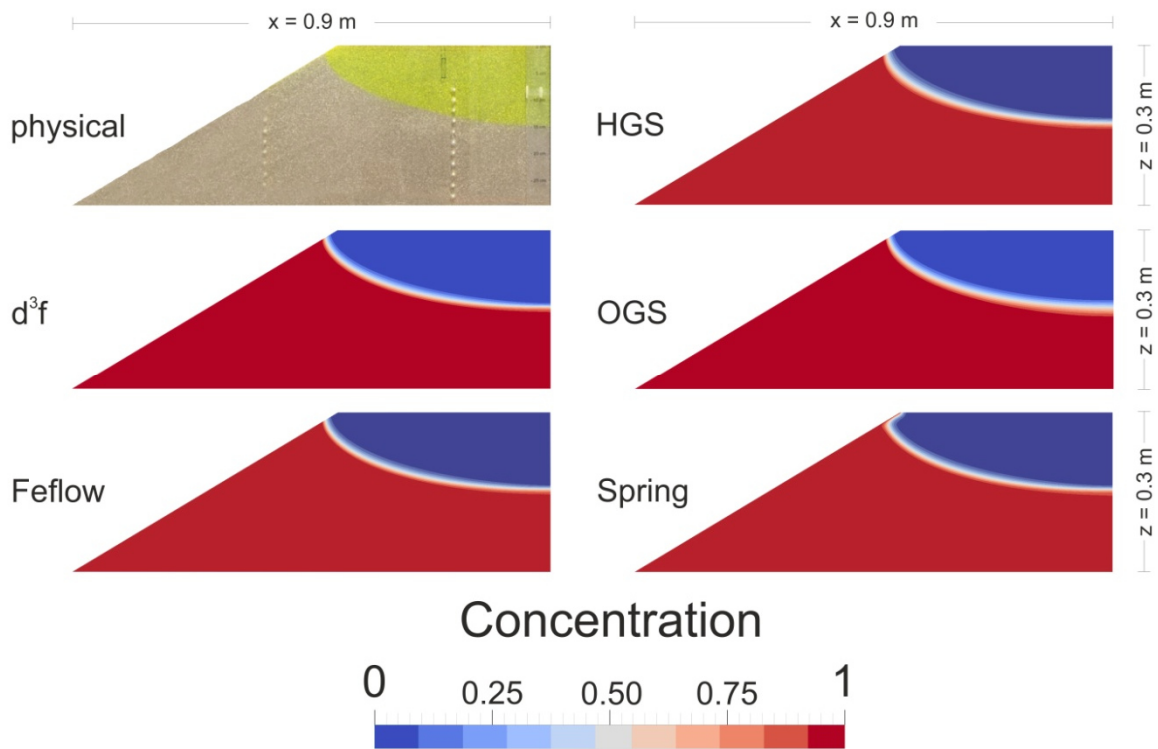
Figure 5-1: Physical model (top left) and numerical simulation results of salinity distribution between freshwater (c=0) and saltwater (c=1) at steady-state.

5.2.2 Steady-state flow directions

Numerical simulation results of angles of flow direction at steady-state are displayed in Figure 5-2. All models show a similar arrangement of the contours of flow directions in the fresh- as well as in the saltwater zone: The flow in the freshwater is dominantly from left to right, indicated by the yellow colour. Flow directions in the saltwater also show a similar pattern, except at the location where the interface intersects the right vertical model boundary. On the right hand side in Figure 5-2, an enlarged view of the area at the right boundary close to the position of the interface is displayed. The model d^3f shows clear transitions and no fluctuations of flow directions. In Spring, and more apparent in Feflow, small deviations are visible by irregularities among the colors (orange, red and blue) at the vertical no-flow boundary. The larger orange/red colored areas within the yellow zone obtained by HGS indicate upward flow. In OGS, vectors tend to jump between opposite flow directions from one cell to the next in this area of low flow velocities, visualized by alternating yellow, red, purple and blue colors.
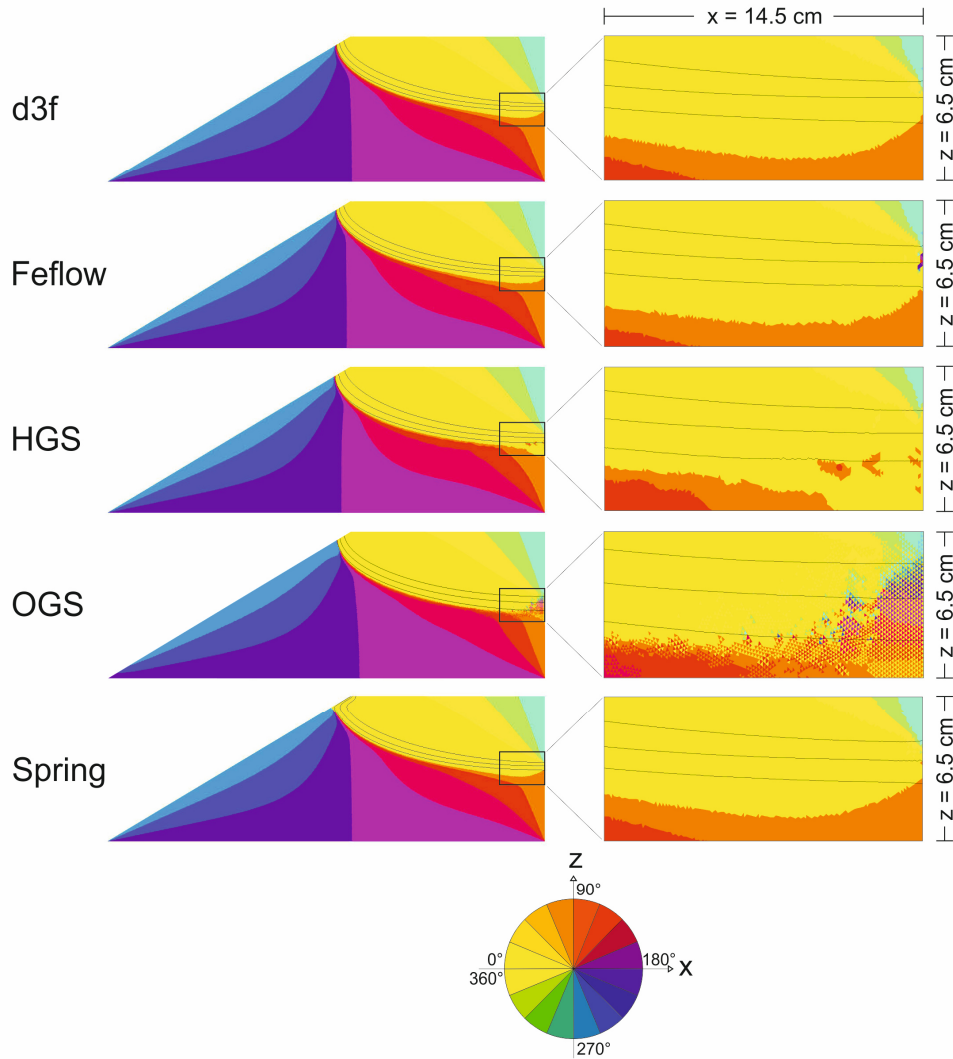
Figure 5-2: Numerical simulation results of angles of flow direction at steady-state in respect to the horizontal vector from right to left (0°). The black lines represent the 0.1, 0.5, 0.9 concentration contours from top to bottom, respectively. On the right hand, an enlarged view of the transition zone at the vertical boundary is shown for each model.

5.2.3 Propagation of the 0.5 concentration contour at the vertical boundary

In the numerical simulations, the transient interface propagation was recorded by tracking the 0.5 concentration contour at the vertical boundary (right side of the model) over time. The recordings of the 0.5 concentration contour propagation in all five numerical models and the physical experiment is displayed in Figure 5-3. The development and degradation of the freshwater lens are almost identical throughout all times of measurement and deviate only slightly in respect to the physical measurements resulting in a Nash-Sutcliff coefficient of $0.97 < E < 0.98$ for all numerical models (equation 5.1). This parameter is determined by

$$E = 1 - \frac{\sum_{t=1}^{T}\left(z_o^t - z_m^t\right)^2}{\sum_{T=1}^{t}\left(z_o^t - \bar{z}_o\right)^2},$$ (5.1)

where z_o^t is the observed depth [m] at time t, z_m^t the modeled or simulated depth [m] at time t and $\bar{z}_o$ the mean depth [m]. E may vary between $-\infty$ and 1, where 1 indicates exact accordance between observed and simulated results, and vice-versa.
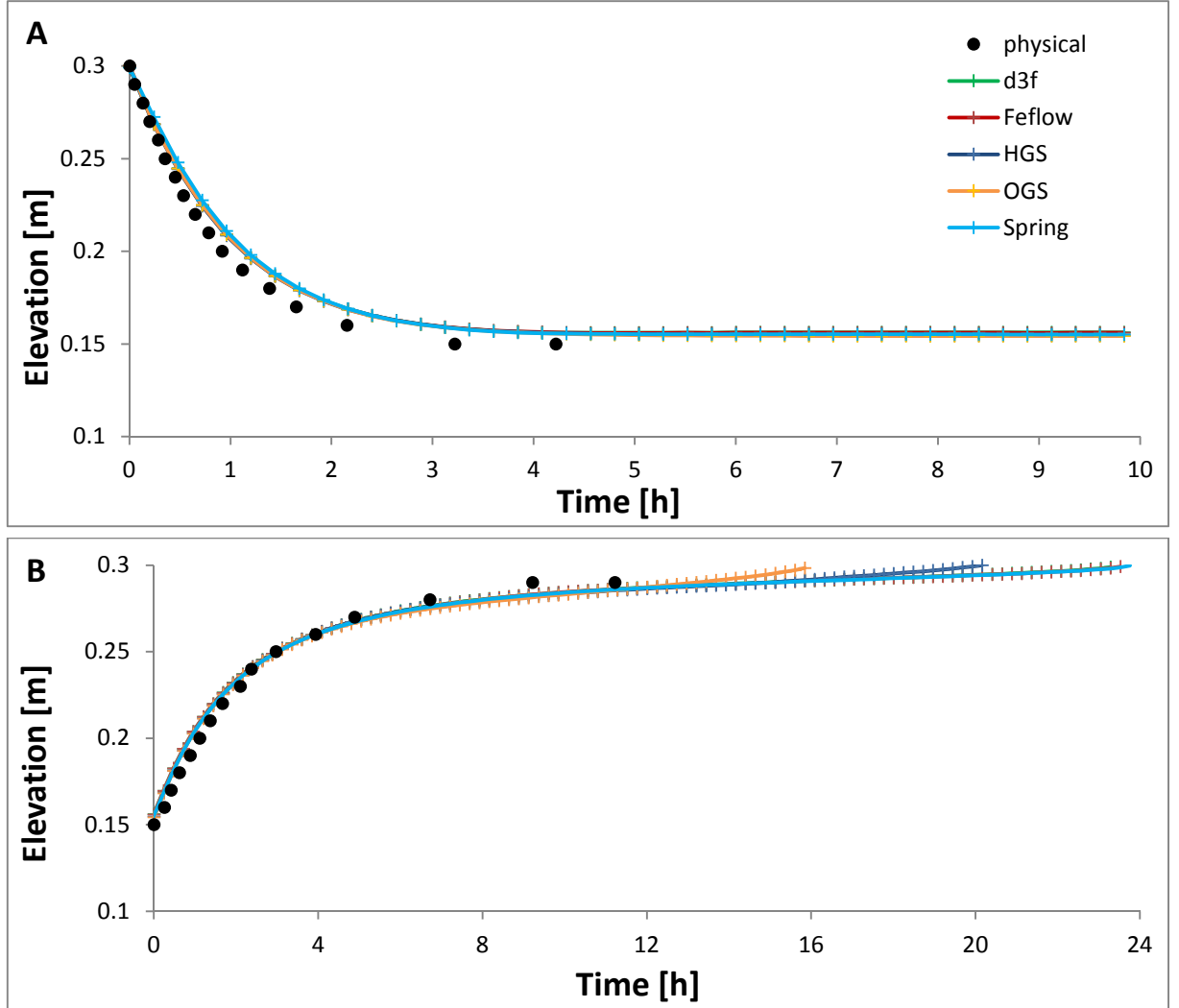
Figure 5-3: Comparison of the propagation of the interface position measured at the centre of the island in the physical experiment (black dots) and at the right vertical boundary (numerical models) during A) lens formation (top) and B) degradation (bottom).
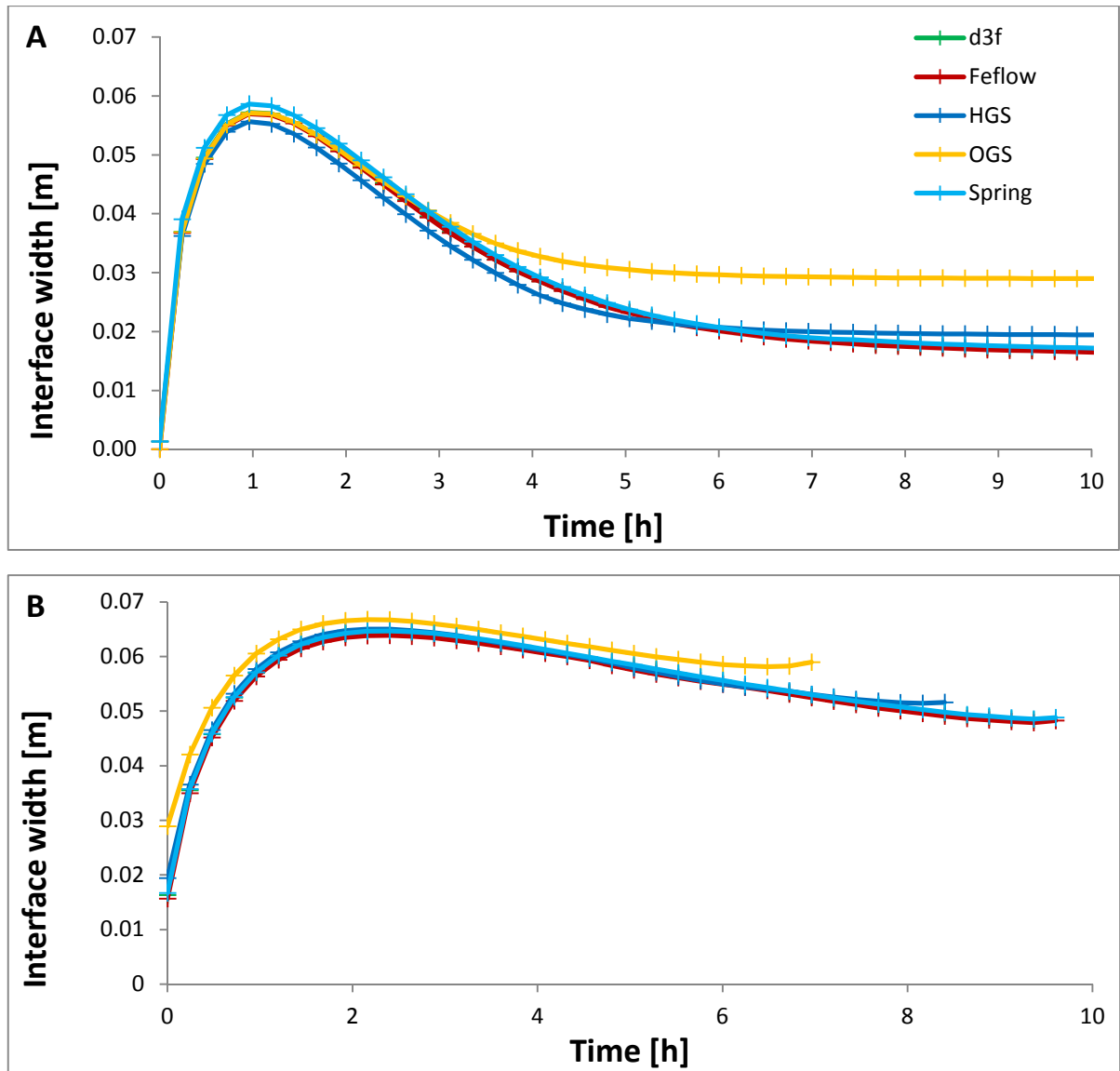
Figure 5-4: Transient development of the interface width ($0.1 < c < 0.9$) at the vertical boundary during A) lens formation (top) and B) degradation (bottom). The green curve by d³f is not visible because plotting exactly behind the red curve by Feflow.

5.3 Discussion

All five different model codes are capable to represent the freshwater lens benchmark to a high degree. The overall identical numerical setups lead to consistent results between all numerical models and the physical experiment. This consistency indicates that all physical processes necessary to simulate the freshwater lens benchmark are properly implemented in all codes.

From steady-state salinity distributions (Figure 5-1) a slightly wider freshwater-saltwater interface is observed by OGS at the vertical boundary, and by HGS close to the outflow

zone, compared to the other models. As basic conditions are kept identical for all numerical models (e.g. transversal and longitudinal dispersivities), it is assumed that technical reasons lead to differences in model output by e.g. the availability of certain solver types. It is remarkable that only d³f and Feflow optically show identical results.

Flow directions along the right vertical boundary indicate, that freshwater from above, and saltwater from below, converge at the interface at steady-state (Figure 5-2). In theory, this causes a "singularity" at that point, where the 0.5 contour intersects the vertical boundary. Here, flow velocities approach zero, which makes this area sensitive for subtle deviations in the calculations of the flow field, as observed when zoomed into the model output results. Clearly, d³f shows the most homogeneous results, followed by Spring. It must be mentioned, that d³f was explicitly developed for variable-density problems and high salinity brines for the field of nuclear waste deposits and therefore performs high accuracy calculations. Because d³f is the only finite volume code compared to the other finite element codes, local mass conservation is given. This might lead to more consistent results of the density-dependent flow directions here as well. Spring uses an upwind scheme by default, which probably leads to smoother results here as well. In Feflow, flow directions change in only a few cells right next to the vertical boundary. The deviations in flow directions around the singularity by HGS and OGS are most apparent. An explanation for the results obtained by OGS might be attributed to the formulation of the mass transport equation in OGS. Here, velocities within the cells are averaged leading to different directions when flow velocities get considerably small. Still, it must be kept in mind that the area where these inconsistencies occur is very limited compared to the extent of the model and flow direction are nearly identical in all other parts.

As observed in the physical experiment, the degradation of the freshwater lens takes much longer than its formation (compare Figure 5-3). Because of the extremely long degradation times (nearly 24 h for the 0.5 concentration contour to disappear), these transient results are more sensitive to small deviations in density: the 0.5 concentration contours at the vertical boundary simulated by OGS and HGS recover quicker than those by d³f, Feflow and Spring. Interestingly, all numerical models show an acceleration of the 0.5 concentration contours during the final stage of the degradation phase (upward bending of the curves in Figure 5-3b). This, however, cannot be explained on a physical basis but is rather assumed to be a numerical artefact. All boundary conditions at that side of the model domain (horizontal top and bottom as well as vertical boundary at the right) are considered Neumann no-flow and Neumann zero-dispersive BCs. Thus, the only fluxes across the model boundaries are present at the left over side of the model (at the sloping boundary on the left) where the Dirichlet constant head BC (plus Dirichlet constant transport BC) are applied. An explanation for this upward bending might be

internal rounding errors, which make the models sensitive to very small concentration gradients as they occur during the final stage of the degradation phase, and when flow velocities become extremely small.

The measurement of the width of the saltwater-freshwater interface shows the strongest deviations between the individual modeling tools applied in this study (Figure 5-4). As longitudinal and transversal dispersivities dominate mixing process of fresh- and saltwater (compare the much smaller molecular diffusion coefficient D_m of 10^{-9} m^2 s^{-1}), the deviations might be caused by different implementations of the dispersivities into the single codes. E.g. a severe error in the implementation of the dispersivities had occurred in one of the models prior to this study, where the freshwater-saltwater interface occurred much broader. This was immediately corrected with the help of the developer team. Still, smaller inaccuracies or differing forms of calculation might lead to the observed effects.

The overall wider interface during the degradation phase obtained by OGS can be explained by slight variations in the steady-state of the recharge phase, resulting in a different initial condition for the subsequent degradation phase.

Similar to the numerically caused acceleration of the 0.5 concentration contour at the end of the degradation phase, an interface widening is caused by the acceleration of the 0.1 concentration contour which was observed in all models. This leads to the upward bending of the curve at the final stage in of the graphs in Figure 5-4B.

Additional numerical test simulations were conducted, invoking the Oberbeck-Boussinesq (OB) approximation, by neglecting all density dependencies in the balance terms, except the buoyancy term in the momentum conservation equation (not shown here). This, however, did not affect the position and transient propagation of the concentration contours. These observations are consistent with Guevara Morel and Graf (submitted), who showed that for small densities (<5% saltwater) the effect of the OB approximations is negligible.

5.4 Conclusions

As benchmarks are important to test numerical codes, this chapter gives the reader an overview of the accuracy of five state-of-the-art variable-density groundwater modeling tools. It was shown that the benchmark of a freshwater lens reveals subtle deviations in the different numerical codes based on physical observations. The results obtained by this study may be reproduced and compared with other modeling software, as the grid and parameters applied are available in this publication and as supplementary material.

76

As the list of variable-density modeling tools is not complete and only one benchmark with certain specifications is investigated here. Due to the small variations within the results, and the fact that every task/project/investigation requires an individual decision for the choice of the model software, it is restrained from giving a recommendation for the selection of a particular software. The goal of this study was to test the accuracies and distinct features of certain numerical model codes. It is thus recommended to use a modeling tool that is able to realistically simulate the processes that are most important for the respective study. For example, if one would be investigating the freshwater discharge zone in combination with the interface location of a coastal aquifer, one would need to take care that the model includes a transport boundary that may be disabled, depending on the flow direction ("constrained boundary condition"), or that the model is versatile enough to incorporate any other relevant features. Computation times might also play a role for large model setups, which were not investigated by this study, instead a constant time-step resolution provided by Stoeckl et al. (2016) was selected. This results in longer computation times but higher calculation accuracy, ensuring maximum comparability of the different modeling tools. Yet, most tools are able to realize automated time control schemes, while some might also reduce computation time by the application of adaptive meshes. As this goes beyond the scope of this study, it is concluded from the results obtained here that the selection of a specific tool should always be carefully thought of depending on the problem definition. Finally, the model choice might very much depend on existing experience and knowledge of the modeler, or be governed by financial resources. Nevertheless, this comparison gives an overview and compares results of five renowned modeling tools for the first time using the freshwater lens benchmark.

6 Synthesis

6.1 Major outcomes

The major objective of this study was to explore flow pattern within freshwater lenses like flow paths, travel times, and age stratification in homogenous, as well as heterogeneous island aquifers in steady-state as well as in transience. To achieve this goal, sand tank experiments and numerical modeling were successfully conducted in order to visualize and measure different aspects of freshwater lenses in the controlled laboratory environment for the first time.

- With the homogeneous model setup, it could be shown, that the depletion of a freshwater lens after a stop in recharge, takes much longer than the lens development, presuming that no pumping is involved and that the other boundary conditions remain constant over time (Stoeckl and Houben, 2012). The fragile equilibrium of these systems and their vulnerability to climate change is demonstrated by their response times: they are easily disturbed by changes in boundary conditions (e.g. droughts), but it takes much longer to re-establish equilibrium, i.e. steady-state.

- Flow paths and age stratification of a freshwater lens were visualized and measured for the first time in a sand tank experiment, showing that all flow paths stay connected with the outflow zones at all times, and that age strata become thinner with depth and over time (Stoeckl and Houben, 2012). Travel times from the physical model setup were successfully compared to numerical model results and validate previously published analytical model solutions, e.g. by Chesnaux and Allen (2008).

- Four non-homogeneous island set-ups with boundary conditions taken from Vacher (1988) were also simulated in the laboratory, and different flow patterns were measured for each set-up. Especially observations for Case C with a lower, more permeable layer deviated from the homogeneous case and lead to a bimodal distribution in travel times and an inversion in age stratification (Stoeckl et al., 2015). The understanding of the different processes in each case can now be used for the development of conceptual models when managing certain island types e.g. for the delineation of groundwater protection zones.

- Comparing the steady-state interface geometries of the different islands in the physical experiments and numerical simulations to the analytical solutions by Vacher (1988) shows, that all geometries are reproducible. Only Case C did not correspond to the analytical solution, thus a correction was elaborated (Appendix, Dose et al., 2014). A correct and validated assessment is now possible when estimating the thickness of freshwater lenses on real islands.

The development of a physically based numerical benchmark formulation was the second objective of this thesis. As the worthiness of the freshwater lens benchmark is demonstrated, it constitutes an alternative to the widely used Henry (1964b) problem (Stoeckl et al., 2016). Compared to previous benchmarks, the newly developed benchmark includes physical aspects of saltwater intrusion which have not been benchmarked before (e.g. sloping beach face, freshwater recharge from the top, flow inside a freshwater lens).

Subsequently, the newly developed benchmark was used to compare five different numerical model codes, revealing deviations, conformities, and potentials of these codes. It could be shown, that all codes are in general capable to reproduce the benchmark. The slight deviations however help developers reviewing their work, and give users the possibility for proper code selection.

6.2 Outlook

The processes and dynamics in freshwater lenses investigated by laboratory experiments are compared to numerical models and analytical solutions based on previously defined homogeneous and heterogeneous cases for real world islands. An up-scaling of the results is thus assumed to be applicable and was partly proven by follow-up studies (e.g. the age stratification by Houben et al., 2014a). However, for the field proof of specific features found in this study, e.g. the inversion of ages found for Case C, more detailed field work is needed. The results presented in this thesis can be used as templates for the delineation of protection zones on islands in future.

Saltwater inundation by storm surge or tsunami is a major risk for an island´s freshwater lens. Saltwater infiltrating into a freshwater aquifer from the top may contaminate the

lens in the long term (Terry and Falkland, 2010). Sand tank experiments would be helpful to better understand infiltration processes and effects of different boundary conditions, which were numerically studied by e.g. Holding and Allen (2015a). The amount of saltwater entering the saturated zone depends on several factors, e.g. inundation time, depth to water table, or porosity, which could be investigated by setting up similar laboratory experiments as presented in this theses. Simulating a storm surge might then be achieved by switching the recharge drippers from fresh- to saltwater for a certain amount of time or by raising the saltwater table above the island.

Regarding the development of benchmarks, variable-density flow is caused by different solute concentrations as it is the case in coastal zones or in the vicinity of salt domes. On the other side, temperature gradients might also influence the density of groundwater and thus lead to variable-density flow and free convection. As outlined in this thesis, the Elder (1967) problem was originally developed using a heat source at the bottom of the model domain. However, no benchmark combining mass and heat effects on the flow of groundwater exists so far. This gap could be closed by constructing a benchmark imitating the original Elder (1967) problem, in combination with e.g. saltwater underlying a freshwater layer as initial condition.

7 Appendix: Experiments and modeling of freshwater lenses in layered aquifers: Steady state interface geometry

The work of this chapter has been published as: Dose, E.J., Stoeckl, L., Houben, G.J., Vacher, L.H., Vassolo, S., Dietrich, J., Himmelsbach, T., 2014. 'Experiments and modeling of freshwater lenses in layered aquifers: Steady state interface geometry'. In: *Journal of Hydrology*, 509: 621–630.

7.1 Experimental methods and materials

7.1.1 Physical model

In a previous paper by Stoeckl and Houben (2012), a series of physical model experiments was performed to study the formation and degradation of lenses in homogeneous (single-layer) aquifers. The experiments addressed the steady-state geometry of the lenses, the groundwater flow paths within them, and the spatial distribution of groundwater age. Results were successfully compared to analytical and numerical models. This paper follows a similar outline but considers inhomogeneous, layered systems, that is, lenses occurring in islands that are partitioned into horizontal layers or vertical columns of differing hydraulic conductivities or into areas of differing groundwater recharge. This study is based on the four geometries of infinite-strip islands for which Vacher (1988) developed analytical models (Figure 7-1A–D), and one more scenario from an earlier equation in Fetter (1972) was added (Figure 7-1E).

Figure 7-1: Investigated cases of inhomogeneous island freshwater lenses: Case A: lateral variation of hydraulic conductivity K (K1 > K2), Case B: lateral variation of recharge R (R1 > R2), Case C: horizontal layering (K1 < K2), Case D: freshwater lens truncated by impermeable base. Case E: horizontal layering (K1 > K2). L = width of island, x = distance from shore, x_1 = distance to interface intersection from shore, A = distance to vertical sector boundary from shore, M = distance to groundwater divide, K = hydraulic conductivity of layer, Q = flow rate, R = recharge of sector. Modified after Vacher (1988).

The experimental set-up was based on the one used by Stoeckl and Houben (2012). A cross-section of an infinite strip island was simulated using an acrylic glass box of 2.0 m length, 0.5 m height and 0.05 m width filled with sand. The sand was slightly compacted by palpitation during this process.

Commercially available coarse and medium filter sands, commonly used for gravel packs of wells, were chosen to represent the aquifer material (Table 7-1). The two sands have a hydraulic conductivity ratio of roughly 10:1. Their grain size distributions were

determined optically using a Camsizer (Retsch Technology, Germany), which has a measurement range between 30 μm and 30 mm. Total porosity was calculated using the bulk and mineral densities measured using a helium pycnometer by Micromeritics (USA). Sorting, skewness and sphericity were analysed following the methods of Folk and Ward (1957). As expected for filter sands, both samples are very well sorted and composed of well-rounded grains. The granulometric data were used to calculate the hydraulic conductivity following the empirical methods of Seelheim, 1880 and Hazen, 1911 and Bialas and Kleczkowski (1970).

Table 7-1: Granulometric properties of sand materials.

Parameter	Unit	Coarse sand	Medium sand
d_{10}	(μm)	1272	440
d_{20}	(μm)	1391	500
d_{60}	(μm)	1802	657
u (=d_{60}/d_{10})	(−)	1.42	1.49
Median	(μm)	1694	618
Sorting	(−)	1.17	1.17
Skewness	(−)	1.00	0.98
Sphericity	(−)	0.82	0.85
Porosity	(−)	0.41	0.45
Hydraulic conductivity K			
SEELHEIM	(m/s)	$1.0 \cdot 10^{-2}$	$1.4 \cdot 10^{-3}$
BIALAS/KLECZKOWSKI	(m/s)	$7.7 \cdot 10^{-3}$	$7.3 \cdot 10^{-4}$
HAZEN	(m/s)	$1.9 \cdot 10^{-2}$	$2.3 \cdot 10^{-3}$

The saturated hydraulic conductivity according to Darcy's law was measured using a constant-head permeameter by Eijkelkamp Agrisearch (Netherlands). Ten experiments were conducted for each type of sand. The results are shown in Table 7-2.

Table 7-2: Mean hydraulic conductivity of sand materials from constant head permeameter tests.

Parameter	Unit	Coarse sand	Medium sand
Number of samples		10	10
Max K	(m/s)	$1.3 \cdot 10^{-2}$	$2.1 \cdot 10^{-3}$
Min K	(m/s)	$3.9 \cdot 10^{-3}$	$7.3 \cdot 10^{-4}$
Average K	(m/s)	$9.7 \cdot 10^{-3}$	$1.4 \cdot 10^{-3}$
Max bulk density	(m/s)	1.53	1.45
Min bulk density	(g/cm^3)	1.43	1.36

The impermeable material used for Case D was pink plasticine (Play-Doh, Hasbro, USA), which proved to be quite effective as no dyed water crossed this barrier.

The density of both fresh and saline water was determined using a density meter DMA 38 by Anton Paar (Austria). Density of freshwater was determined to be 997.4 kg/m^3 and that of saline water to be 1021.2 kg/m^3. Prior to injection, the saltwater was degassed to prevent air entrapment by outgassing. It was injected slowly from the bottom of the model, thereby expelling air and saturating the sand. The temperature of the laboratory was monitored and kept constant throughout the experiment (23 °C).

Recharge was simulated by fifteen freshwater drippers installed above the island surface (0.04 m^2) and supplied by a multi-channel peristaltic pump (Ismatec BVP, Wertheim, Germany). The recharge rate for Cases A, C and D was set to 1.33 m/d, equivalent to 2.46 ml/min per drip. For Case B, the recharge rates were 1.38 and 0.67 m/d for the Sectors I and II, respectively, and for Case B-modified, the two rates were 1.38 and 0.0 m/d, respectively. For Case E, a recharge rate of 1.33 m/d did not result in a penetration of the freshwater-saltwater interface into the second layer. At a rate of 2.66 m/d a small amount of penetration of the freshwater body into the lower sand layer was observed.

For the visualization of flow paths, the fluorescent dyes uranine (yellow), eosine (red) and indigotine (blue) were added to the freshwater as tracers at a concentration of 0.3 g/l. The effects of the different tracers on density and viscosity of the fluid are negligible.

Freshwater that discharged at the outflow zones was continuously skimmed at both sides of the model by an Ismatec BVP peristaltic pump (Ismatec, Germany) set to a rate

equaling total freshwater recharge. The intention of the skimming was to prevent dilution of saltwater and to maintain a constant seawater head. Slight mixing due to diffusion and dispersion was inevitable but had no significant effect on saltwater density, as measurements of saltwater electrical conductivity confirmed.

The height of the freshwater table above the sea level (h) was not measured since it was not possible to visually distinguish the saturated zone from the capillary fringe of the unsaturated zone in the physical model. Hence, only the interface depth (z) was analyzed in both the numerical and analytical models. In the physical model, z was read off a ruler attached to the middle of the model and from video stills.

Unlike in the experiments by Stoeckl and Houben (2012), it was not able to apply the same value of hydraulic conductivity for a given type of sand for different experiments. As all cases implied different spatial arrangements of the sands, the backfilling of layers of different materials led to different degrees of compaction which in turn resulted in differing hydraulic conductivities from experiment to experiment. The range of hydraulic conductivities given in Table 7-1 and Table 7-2 was used as a constraint for fitting the numerical models to the experimental data.

7.1.2 Analytical models

Vacher (1988) derived Dupuit–Ghyben–Herzberg (DGH) analytical models for four common cases of hydrogeological heterogeneities of island freshwater lenses (Figure 7-1). DGH analysis combines the Dupuit assumption of vertical equipotentials (Kirkham, 1967) and the Ghyben–Herzberg assumptions of immiscible freshwater and saltwater (hence sharp freshwater–saltwater interface) and uniformly zero saltwater head. This last assumption reduces the two-term Hubbert equation for the elevation of the interface in terms of freshwater and saltwater heads (Hubbert, 1940, Eq. (198); Reilly and Goodman, 1985, Eq. (3); Vacher, 1988, Eq. (2)) to the well-known simple proportionality between the depth of the interface below sea level and the elevation of the water table above sea level at a given locality (Bear, 1979, Chap. 9; Vacher 1988); the proportionality constant is the density-difference ratio of the Ghyben–Herzberg principle (Badon-Ghyben, 1888 and Herzberg, 1901), and the datum for the freshwater head is sea level. Sectors (indicated by Roman numerals in Figure 7-1) refer to side-by-side strips defined by hydrogeologic boundaries (Case A), a recharge boundary (Case B), or where the interface encounters a contrasting subsurface hydrogeologic unit (Cases C–E). For Cases A and B, the hydrogeologic (A) and recharge (B) boundaries were put in the middle of the model. The variables used are as follows:

$h_{I,II}$ water table elevation above sea level in Sector I or II (m)

h_A water table elevation above sea level at the sector boundary (m)

h_b water table elevation above sea level directly above intersection of interface and hydrogeologic boundary (m)

$K_{1,2}$ hydraulic conductivity for layer 1 or 2 (m/s)

R recharge rate (m/s)

x horizontal coordinate (m)

x_1 horizontal coordinate of the intersection of the interface and a sector boundary (m)

L width of the island cross-section (coast to coast) (m)

a half-width of the island (m)

b_0 thickness of the upper layer, below sea level (m)

M horizontal coordinate of the groundwater divide (m)

A distance to boundary between strips (m)

β Ghyben–Herzberg density ratio (Badon-Ghyben, 1888 and Herzberg, 1901)

ρ_f freshwater density (g/cm^3)

ρ_s saltwater density (g/cm^3)

Case A of Vacher (1988) represents lateral variations of the geological constitution of the island and thus lateral variations in the hydraulic conductivity of the upper saturated zone containing the lens. An example for an island lens within side-by-side strips of different hydraulic conductivity occurs in Bermuda, which, in the area of the main freshwater lens, is composed of two Pleistocene limestones of different ages and hence different amounts of secondary permeability (Vacher, 1978, Vacher and Wallis, 1992 and Vacher and Mylroie, 2002). The DGH water table elevation in the two sectors can be calculated after Vacher (1988) using

$$h_I{}^2 = \left[\frac{R}{K_1\,(\alpha+1)}\right](2Mx - x^2), \tag{7.1}$$

and

$$h_{II}^{2} = h_A{}^{2} + \left[\frac{R}{K_1\,(\alpha+1)}\right][(2M(x - A) - (x^2 - A^2)], \qquad (7.2)$$

with M obtained from

$$M = \frac{\left(\frac{1}{2}\right)[K_1(L^2 - A^2) + K^2 A^2]}{[K_1(L - A) + K_2 A]}. \qquad (7.3)$$

Vacher's (1988) Case B of an island with a nonuniform distribution of recharge can be found, for example, on the Hawaiian Islands (Macdonald et al., 1990). There, precipitation on the mountainous windward side can be ten times as much as that on the leeward side. On some other islands where, in extreme cases, potential evapotranspiration exceeds rainfall, e.g. at ponds and marshes, net recharge may be zero or even negative. The southern Bahamas, e.g. Great Exuma, provide examples of this, with small lenses beneath Pleistocene eolianite ridges; the lenses are separated from each other by saline water underneath ponds and marshes between the ridges (Wallis et al., 1991 and Vacher and Wallis, 1992). Therefore, a Case B-modified was also included where the recharge in the second sector was set to zero. The DGH water table elevation in Sectors I and II can be calculated after Vacher (1988) from

$$h_I{}^{2} = \left[\frac{R_1}{K\,(\alpha+1)}\right](2Mx - x^2), \qquad (7.4)$$

and

$$h_{II}^{2} = h_A{}^{2} + \left[\frac{2R_1}{K(\alpha+1)}\right](M - A)(x - A) - \left[\frac{R_2}{K(\alpha+1)}\right](x - A)^2, \qquad (7.5)$$

after calculating M from

$$M = \frac{[R_2 L^2 + A^2(R_2 - R_1) - 2AL(R_2 - R_1)]}{2R_1 L}. \qquad (7.6)$$

Vacher's (1988) Case C of a highly permeable formation located underneath a less-permeable upper formation ($K_1 < K_2$) is a pattern found on the larger islands of the

Bahamas and on many atolls in the Pacific (Ayers and Vacher, 1986, Budd and Vacher, 1991, Underwood et al., 1992 and Bailey et al., 2009). On the atolls, the upper formation is often a Holocene limestone, and the lower formation is a Pleistocene karstified limestone with a hydraulic conductivity 1–2 orders of magnitude higher than that of the surficial unit (Bailey et al., 2009). The DGH water table elevation in Sector I can be calculated after Vacher (1988) from

$$h_I{}^2 = \left[\frac{R}{K_1\,(\alpha+1)}\right](Lx - x^2). \tag{7.7}$$

The DGH water table elevation in Sector II can be calculated iteratively by solving

$$(\alpha K_1 + K_2)(h_{II}^2 - h_b^2) + 2B_1(K_2 - K_1)(h_{II} - h_b)$$
$$= R[L(x - x_I) - (x^2 - x_I^2)], \tag{7.8}$$

using

$$h_b^2 = \left[\frac{R}{K_1(\alpha+1)}\right](Lx_I - x_I^2), \tag{7.9}$$

after finding x_I by iteration from

$$2Mx_I - x_I^2 = \frac{[K_1(\alpha+1)B_I^2]}{R\alpha^2}, \tag{7.10}$$

Eq. (7.8) corrects a typographical error in Vacher (1988, p. 590). Also, Eq. (7.9), which is needed for Cases C and D, was not included in the original paper.

An example of Vacher's (1988) Case D of a freshwater lens truncated at depth by an impermeable layer (perched lens) can be found on Pingelap Atoll, Micronesia, where a reef-flat plate forms the confining layer (Ayers and Vacher, 1986 and Bailey et al., 2009) and, in a completely different setting, at an inland freshwater lens in the Chaco at Benjamín Aceval, Paraguay (Houben et al., 2012). The solutions after Vacher (1988) for the DGH water table elevation in Sectors I and II are

$$h_I{}^2 = \left[\frac{R}{K(\alpha+1)}\right](Lx - x^2),\tag{7.11}$$

and

$$K(h_{II}^2 - h_b^2) + 2KB_1(h_{II} - h_b) = R[L(x - x_I) - (x^2 - x_I^2)],\tag{7.12}$$

where x_1 and h_b^2 are found as in the previous case (Eqs. (7.10) and (7.9), respectively).

The reverse situation of Case C, a permeable aquifer underlain by a less-permeable formation, was not modeled analytically by Vacher (1988). An analytical model by Fetter (1972), however, exists. The case is thus added here as Case E. An example of this setting is Long Island, New York, and the solution after Fetter (1972) is

$$h^2\left[\frac{1}{2}K_1 + \frac{1}{2}K_2\alpha\right] + h(b_0K_1 - b_0K_2) = R\left(\alpha x - \frac{1}{2}x^2\right).\tag{7.13}$$

All equations were calculated using Microsoft Excel spreadsheets. For some equations it was necessary to use iterative techniques. This was done using Excel's target value function and a macro that allows one to apply this operation for whole columns. The maximum number of iterations was set to 5000 and the maximum permissible difference to $1 \cdot 10^{-12}$ m.

With the calculated value for the water table elevation (h) from the above equations, the depth to the interface (z) for any point along the water table can be calculated using the Ghyben–Herzberg principle

$$z = \left(\frac{\rho_f}{\rho_s - \rho_f}\right)h = \beta h.\tag{7.14}$$

It is z that is the measurable dependent variable in the physical model.

7.1.3 Numerical model

For numerical modeling, the finite-element model code Feflow 6.0 was used (Diersch, 2005). The set-up was based on the one used by Stoeckl and Houben (2012). Parameters and boundary conditions were based on the measured material properties, the setup of the physical model and the analytical model results. The unsaturated zone was not considered. The upper boundary of the mesh was assigned a constant flux (Neumann)

boundary condition with a rate of 1.33 m/d, allowing only freshwater to enter the model. The coastal zones along the island slopes were defined as constant head boundaries (Dirichlet) with a saltwater head of 0.33 m and a solute concentration of 35 kg/m^3.

Considering the cell sizes and potential lengths of flow paths, longitudinal and transversal dispersivities were set to $5 \cdot 10^{-3}$ m and $5 \cdot 10^{-4}$ m, respectively. The aquatic molecular diffusion coefficient was set to $1 \cdot 10^{-9}$ m^2/s, although the elevated flow velocities in our model render diffusion negligible. An automatic control scheme was selected for the time discretization. The initial time-step length was set to 0.00001 d, and the upper boundary for the step size to 0.002 d.

7.2 Results

7.2.1 Flow paths at steady state

The steady state flow paths shown in Figure 7-2 were created by applying different tracer colors in alternating drippers at the same time. The coarse sand generally saw an increase of flow velocity and narrower flow paths. The water divide for the Cases A, B and B-modified (B′) was not located at the sector boundary. For Case A, some water from the left sector (low hydraulic conductivity) flowed towards the right sector. For Cases B and B-modified, water from the sector with higher recharge (left) flowed to the right sector of low or no recharge. In Case B-modified, all water flowing through the right sector (no recharge) of course originated from the left sector. For Case C, water recharged in the middle of the island penetrated into the more-permeable bottom layer, accelerated there and overtook water that passed through only the upper layer. The flow pattern for Case D was axisymmetric, resembling the one for a homogeneous lens (Stoeckl and Houben, 2012), except for the impermeable horizontal bottom. In Case E, only a small proportion of the water, recharged in the very middle of the island, reached the bottom layer; from there, it proceeded to the outflow zone via the upper layer.
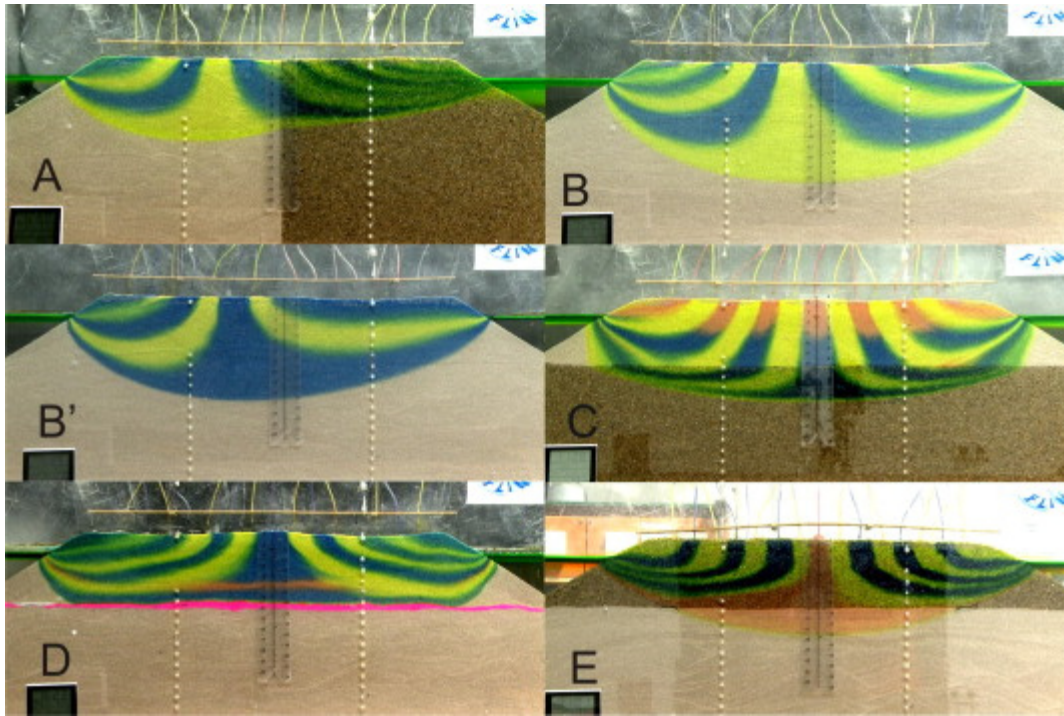
Figure 7-2: Experimental set-up of the physical models showing flow paths at steady state (Cases A, B, B modified, C, D, E).

7.2.2 Comparison of physical, analytical and numerical models

7.2.2.1 Case A

For the Case A of two laterally adjacent sectors of different hydraulic conductivities, both the analytical model by Vacher (1988) and the numerical Feflow model were generally able to simulate the shape of the interface in the physical model experiment quite well using the same parameter set (Figure 7-3). The analytical model, however, does not consider the outflow face. The numerical model significantly overestimated the size of the outflow face for the left sector and underestimated it for the right sector. The hydraulic conductivities shown in Figure 7-3 were used for both the analytical and numerical model.
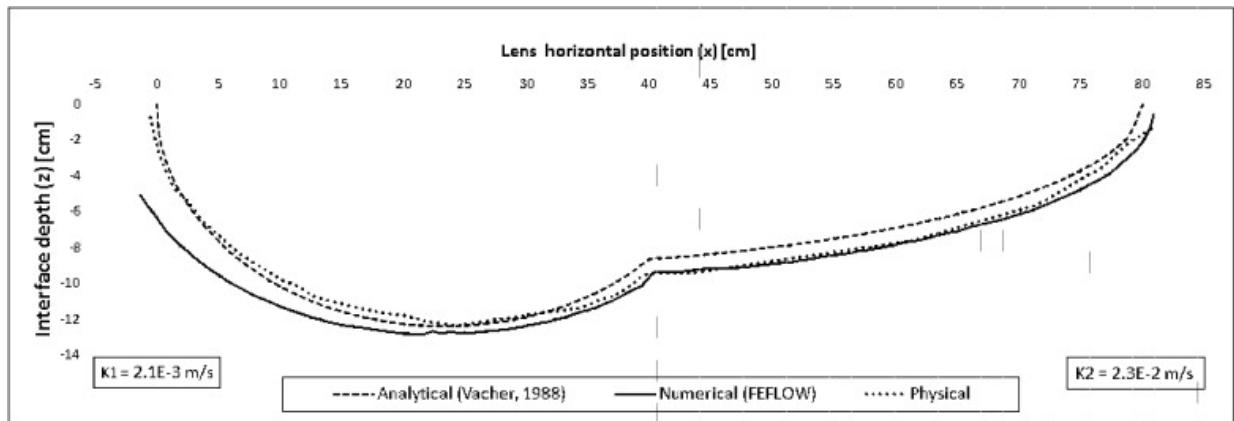
Figure 7-3: Case A interface depth from physical, analytical (Vacher, 1988) and numerical (Feflow) model. The boundary between the two columns of different hydraulic conductivity is located at *x* = 40 cm.

7.2.2.2 Case B

For the Case B of two sectors of identical hydraulic conductivities but differing recharge rate, using the same parameter set, both the analytical model by Vacher (1988) and the numerical Feflow model were generally able to simulate the general shape and position of the interface in the physical model experiment (Figure 7-4), although the former underestimated the interface depth as it neglects the outflow zone. The numerical model overestimated the size of the outflow face, especially at the right side (low recharge).

Figure 7-4: Case B interface depth from physical, analytical (Vacher, 1988) and numerical (Feflow) model. The boundary between the two columns of different recharge is located at *x* = 40 cm.

The fit of the analytical and numerical models with the physical model experiment for Case B-modified was better, especially for the sector which received no recharge (Figure

7-5). The general problems of fitting the left outflow zone were the same as for the unmodified Case B.

Figure 7-5: Modified Case B interface depth from physical, analytical (Vacher, 1988) and numerical (Feflow) model. The boundary between the two columns of different recharge is located at $x = 40$ cm.

7.2.2.3 Case C

For the Case C of two horizontal layers of different hydraulic conductivities, the numerical Feflow model closely fit the shape of the interface in the physical model experiment (Figure 7-6). It even predicted exactly the position of the refraction points but slightly overestimated the size of the outflow zones for both sides. Using the hydraulic conductivity values shown in Fig. 6, the analytical model by Vacher (1988) predicted the general shape and the depth of the refraction points well but failed to emulate the interface depth. It has to be mentioned that a better fit of the analytical model, especially for the interface depth, can be obtained by setting $K_1 = 1.7 \cdot 10^{-3}$ and $K_2 = 5.0 \cdot 10^{-3}$ m/s. These values however would lead to a much worse fit of the numerical model. This is the only case where no common set of hydraulic conductivities could be found that gives a good fit for both the numerical and Vacher's (1988) analytical model.
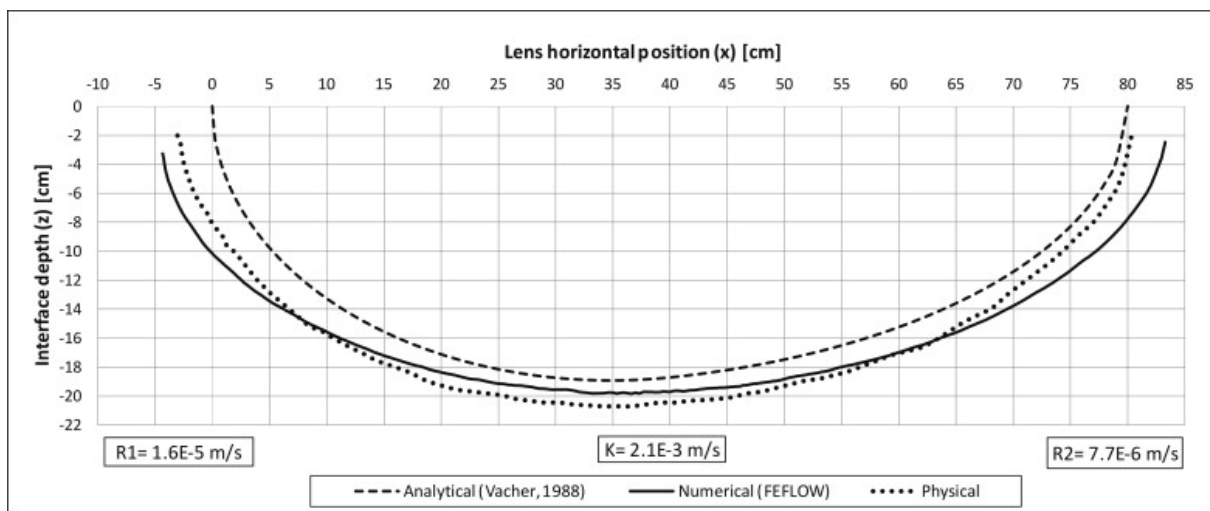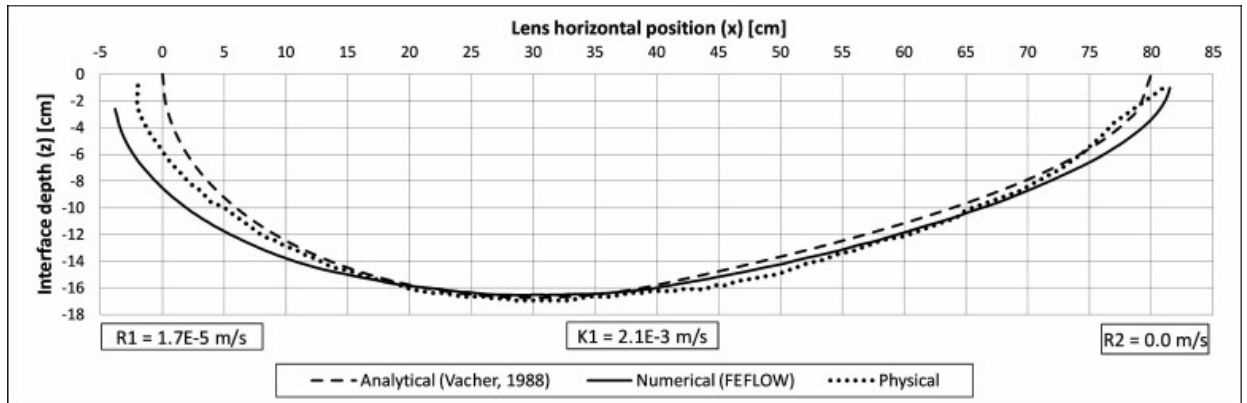
Figure 7-6: Case C interface depth from physical, analytical (Vacher, 1988; Fetter, 1972) and numerical (Feflow) model. The boundary between the two layers of different hydraulic conductivity is located at $z = -10$ cm.

Fetter's (1972) analytical model for a horizontally layered aquifer (Eq. (7.13)) did not provide a good fit with either set of hydraulic conductivities (Figure 7-6). Like Vacher's (1988) analytical model, the Fetter (1972) model does not take into account the outflow face. Unlike Vacher's (1988) model, it does not produce the refraction points representing the discontinuity in the geologic medium that is evident in both the physical and numerical models. The general shape of the lens produced by the Fetter (1972) model is like that of a lens in a single-layer, single-sector medium.

7.2.2.4 Case D

The numerical model gave a very good fit to the physical model geometry of Case D (perched lens), although the outflow face was slightly overestimated (Figure 7-7). The analytical model by Vacher (1988) reproduced the general geometry quite well with the same set of input parameters, with the exception of the outflow face, which it does not take into account.
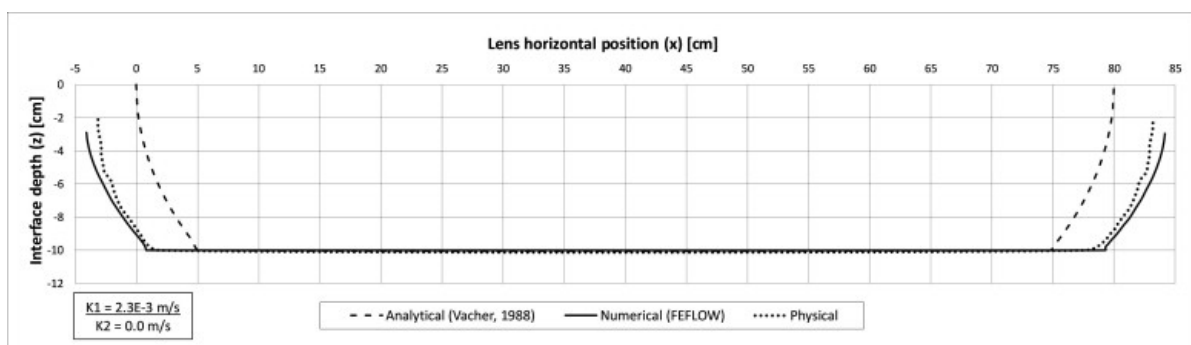
Figure 7-7: Case D interface depth from physical, analytical (Vacher, 1988) and numerical (Feflow) model. The top of the impermeable layer is located at $z = -10$ cm.

96

7.2.2.5 Case E

Fetter's (1972) analytical model for the two-layer case where the deep layer has the lower hydraulic conductivity did not give a satisfactory fit to result of the physical model experiment (Figure 7-8). The numerical model on the other hand gave a reasonably good fit, although the outflow face was slightly overestimated; the refraction point was hardly visible and also slightly off (Figure 7-8).
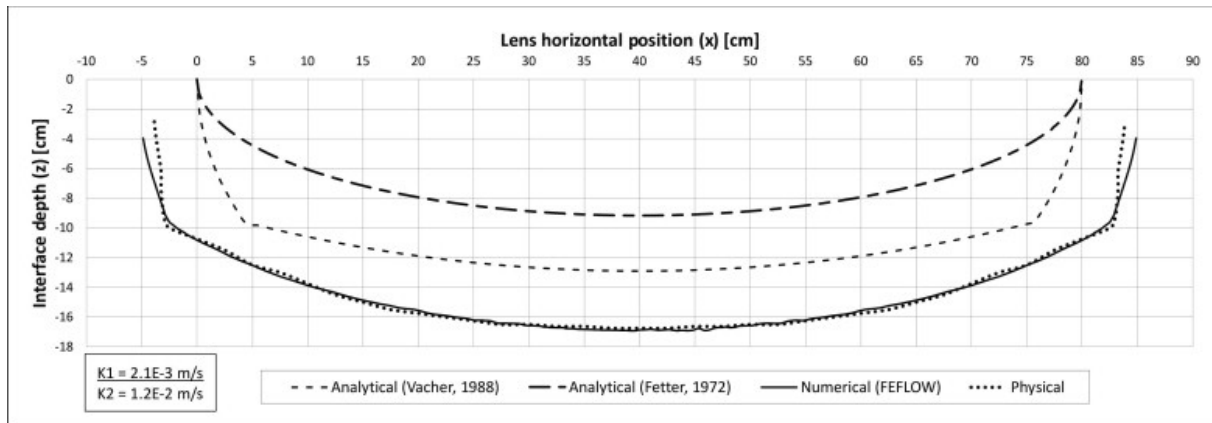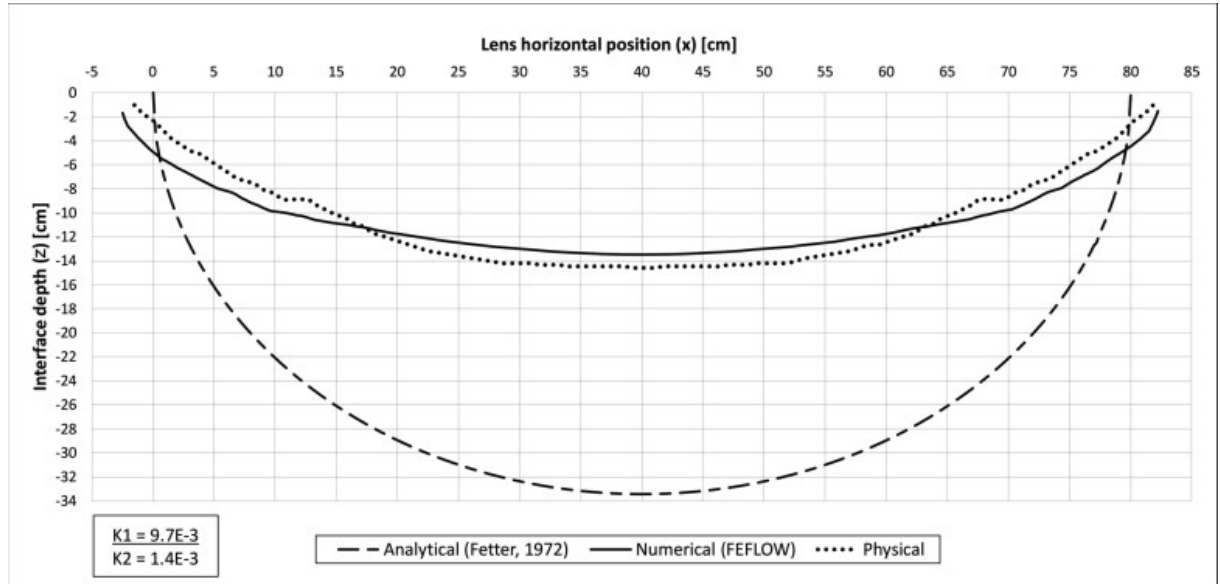

Figure 7-8: Case E interface depth from physical, analytical (Fetter, 1972) and numerical (Feflow) model. The boundary between the two layers of different hydraulic conductivity is located at $z = -9$ cm.

7.3 Discussion

7.3.1 General observations

The shape of the freshwater lens from all the experiments could be reproduced reasonably well by the numerical (Feflow) and DGH analytical (Vacher, 1988) models. With regard to the latter, the best results were obtained in the cases with small outflow faces because the analytical models do not consider them. In unconfined natural islands, though, the width of the outflow face is relatively small compared to the dimensions of the lens. Additionally, freshwater lenses in nature show a predominantly horizontal flow regime due to their thin, pancake-like geometry. In our physical model experiments, the ratio of the thickness of the freshwater lens to the width of the island is rather large, around 1:4 to 1:5; in contrast, ratios between 1:20 and 1:100 are common for real lenses (Vacher, 1988 and Stoeckl and Houben, 2012). Flow processes in our physical model are therefore in an environment with at least fourfold vertical exaggeration relative to freshwater lenses of actual islands. Thus, in general, the experiments with the physical model can be

expected to agree better with the numerical models than with the DGH models because the latter do not take account of either the outflow face or vertical flow components, but given the characteristics of natural lenses, the discrepancies may be exaggerated in the experiments.

It should be noted that the inevitable small fluctuations of the recharge rate during the experiments hardly affected the overall lens geometry, but may have had a significant effect on the width of the small outflow face. This might explain some of the discrepancies between the numerical and physical models at the island boundaries.

7.3.2 Case A

The analytical model by Vacher (1988) correctly predicted an asymmetric trace of the interface as it crosses the island, i.e., a thicker lens in the sector of lower hydraulic conductivity (Sector I, K1); a thinner lens in the sector of higher hydraulic conductivity (Sector II, K2); and an abrupt change in slope of the interface where it crosses the boundary between the two sectors (Figure 7-1 and Figure 7-9). The analytical model by Vacher (1988) matched the general interface geometry of the physical model well.
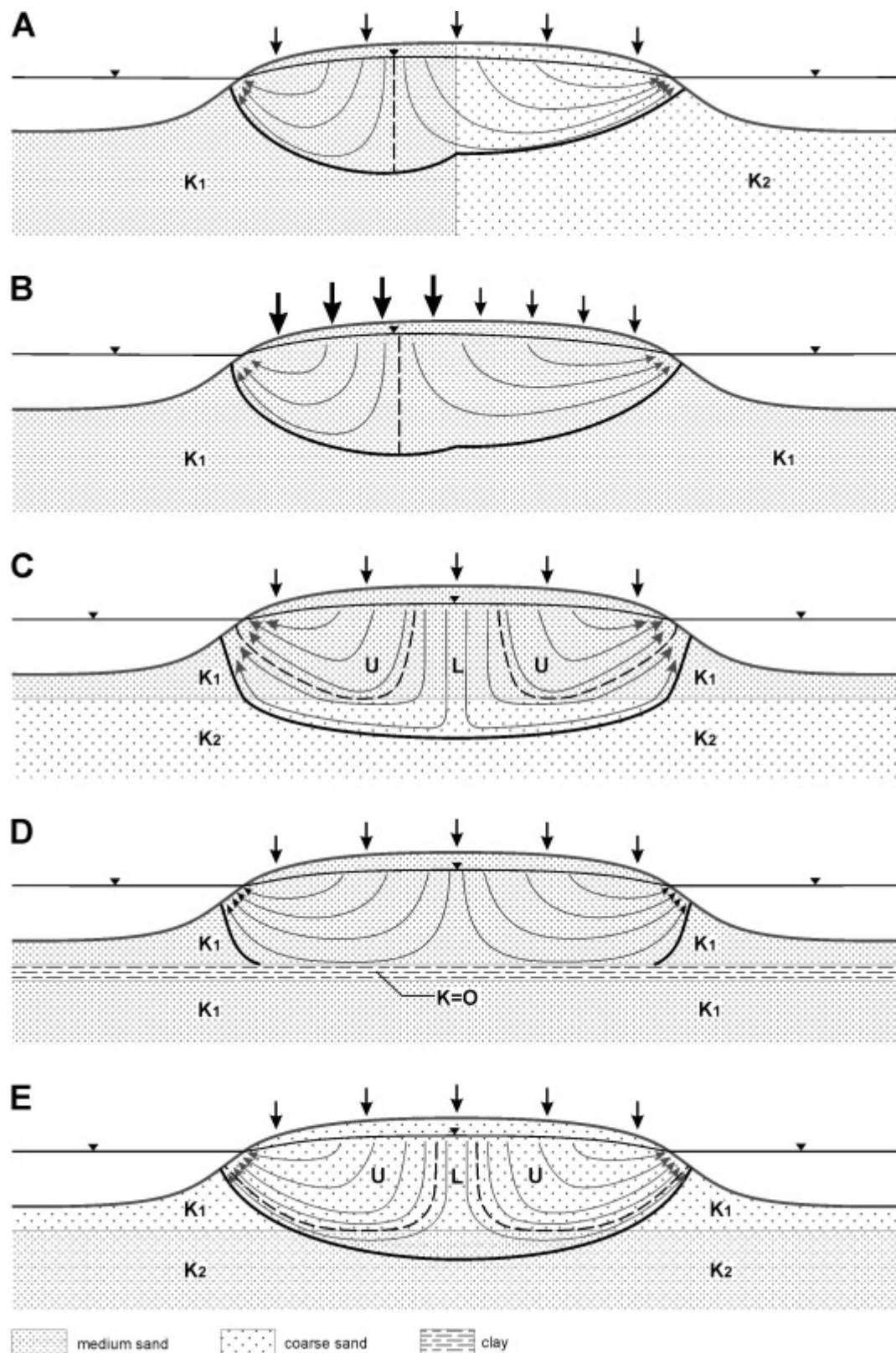
Figure 7-9: Sketch of interface geometry and flow paths for Cases A to E. U = flow passes only through upper layer, L = flow passes through both layers, separation between the two zones indicated by dashed line.

The water divide developed in low-conductivity Sector I, and most of the water flowed in the direction of the outflow zone of Sector II. As a result, a wider outflow face developed in this Sector (Figure 7-9A).

The numerical model also gave good agreement with the physical model experiment. However, the outflow faces of the numerical model showed a wider outflow face in Sector I (fine sand sector) and a thinner outflow face in Sector II (coarse sand sector), opposite to the physical model results. However, the outflow face width was not our primary objective in the model fitting.

7.3.3 Case B

The nonuniform distribution of recharge also resulted in an asymmetric lens (Figure 7-9B), which could be modeled fairly well with both the numerical and DGH analytical model. The location of the water divide between the outflow faces – being the deepest point of the interface – was found shifted a few centimeters towards the left Sector I. Overall, a high similarity of the shape to an interface obtained in the homogeneous case was noted, which was already predicted by Vacher (1988). Comparing Case B to Case A, a sector-to-sector contrast in recharge has a smaller effect on cross-island symmetry than sector-to-sector contrast in hydraulic conductivity has, at least within the range of realistic parameters (Vacher, 1988). As expected, the outflow face for Sector I was wider than the one for Sector II.

In the modified Case B scenario ($R_2 = 0$), an interface and outflow face also developed in Sector II despite the lack of recharge in this sector. It received freshwater from drippers located in Sector I close to the center of the island.

7.3.4 Case C

Under this configuration, two regions with different types of flow paths were evident. In the first (U in Figure 7-9C), flow occurred only in the upper sand. In the second (L in Figure 7-9C), flow crossed through the upper sand, passed laterally within the lower sand, and then exited upward through the upper sand. It had a relatively high velocity while in the lower unit in accordance with the much higher hydraulic conductivity there. The dashed line in Figure 7-9 shows the boundary between the two regions.

With regard to the analytical and numerical models, Case C was the only scenario in which no common set of hydraulic conductivities could be used for both the numerical and the analytical models. Each required a different hydraulic conductivity set to give a reasonable fit to the physical model results. The deviations can probably be attributed to the following causes:

(1) Relatively large outflow zone of 3.6 cm in both sectors.

(2) Significant vertical flow, violating the Dupuit assumption of horizontal flow (Figure 7-2).

(3) Dispersion not considered in analytical model.

The set-up of the physical model itself led to a complication. The deposition of the upper layer of medium sand might have caused a significant compaction of the underlying coarse sand, especially in the upper part. Additionally, grains of the fine sand penetrated into the coarse sand pores at the layer boundary. This might have led to a decrease in hydraulic conductivity of the upper part of the second layer.

The analytical model from Fetter (1972) for Case C generally gave a very poor fit to the physical model. First, it did not consider an outflow face. More importantly, it produced the geometry consistent with that of a lens within a single layer, although it is a two-layer model (Eq. (7.13)). It appears that the mathematics of the model do not properly account for the discontinuity of the porous medium, for there was no break in slope of the interface reflecting an internal boundary condition where the interface crosses the layer boundary. Review of the original paper suggests that the two-layer differential equation – the same as used for Sector II in Vacher's (1988) model (Figure 7-1) – was effectively integrated across the entire half-width of the island (Dirichlet boundary condition to Neumann boundary condition) to produce Eq. (7.13). This apparently has the effect of constructing a kind of weighted average of hydraulic conductivities at each location (x), thus reducing the slope of the interface close to the shoreline boundary and systematically thinning the lens relative to that produced by Vacher's (1988) model (Figure 7-6)

7.3.5 Case D

As expected, the physical model experiment for Case D produced a symmetric lens (Figure 7-9D). Its thickness is determined by the position of the impermeable layer that induces a more horizontally oriented flow than in the other cases. Therefore, the numerical model resulted in very close fit. A relatively long time was needed to reach steady state in this case, twice the time of the other models, which usually reached equilibrium after a few hours. Saltwater can drain only horizontally and therefore the formation of the lens took longer. The fit of the analytical model by Vacher (1988) was again negatively influenced by the lack of an outflow face. The lens produced by the analytical model was similar in shape but smaller in size.

7.3.6 Case E

It was observed through Cases A and C that higher hydraulic conductivities generate more horizontally oriented flow paths. Therefore, it was no surprise that, in constructing the physical model for Case E, it was difficult to generate an interface that could reach down to the medium-sand layer beneath the coarse sand. It was necessary to double the recharge rate from that of Cases A, C and D. Even so, with this recharge configuration, only the dripper from the center of the model recharged the second layer (Figure 7-9E). The discharge of water passing through there was comparably small, and the residence time was large due to the long flow paths and slow flow velocity. The recharge zone for the deep part was much smaller than it was for Case C.

Even with the doubled recharge compared to Case C, the outflow face was much smaller due to the predominance of flow through the coarse layer. Its width was obviously more influenced by the position of layers of different hydraulic conductivities than the recharge rate.

The geometry of the interface at the layer boundary was different from that of Case C. In this experiment, the boundary did not manifest as a discrete bend at the boundary but rather as a two-bend stagger including an intermediate approximately horizontal piece about 2 cm in length along the boundary (Figure 7-9). Overall, the general shape of the interface in this two-layer case was more like that in a single layer than was the two-layer Case C (Figure 7-9).

The analytical model by Fetter (1972) for this case matches neither the numerical model nor the results of the physical model experiment. The aberrantly large thickness from the Fetter (1972) model implicates an overweighting of the hydraulic conductivity of the deeper layer, as was our finding with Case C. The smooth trace of the interface (i.e., no apparent discontinuity in the first derivative) again suggests that the equation essentially blends two layers into one.

7.4 Conclusions

The DGH analytical models for freshwater lenses in layered aquifers from Vacher (1988) were generally able to reproduce the geometry of freshwater lenses in our experiments with the physical model. Since the outflow face is not included in the DGH models, the best fits were obtained for the scenarios with small outflow face widths. It is concluded that the analytical models should achieve an even better fit to the geometry of natural unconfined freshwater lenses where outflow faces are relatively insignificant due to their small size compared to the overall lens dimensions.

The good fit of the DGH analytical models to the results of the physical model experiments is remarkable as the lenses in the physical model have a strong vertical exaggeration compared to lenses in actual islands. Therefore, the model lenses deviate significantly from the Dupuit assumption of vertical equipotentials and horizontal flow. Despite these limitations, the good fit shows that physical models remain useful as benchmarks. Again, the analytical models should achieve an even better fit for natural freshwater lenses, at least for those of limited geological complexity, where flow is much more horizontal.

The fits of Fetter's (1972) analytical model for a two-layer lens to the experiments on two-layer lenses were very poor. Although, like Vacher's (1988) models, Fetter's (1972) model does not include outflow faces, the main problem seems to be that it does not take proper account of the geologic boundary within a lens.

The numerical models (Feflow) generally gave better results than the analytical models as they allow the calculation of outflow faces. However, they overestimated outflow face widths in scenarios with lower hydraulic conductivity (medium sand).

One of the problems encountered in the physical experiments was that the different geometries, especially for horizontal layers, resulted in different degrees of compaction of the backfilled material and thus hydraulic conductivities of the layers. Therefore no standard conductivity value could be used for the materials throughout all experiments.

Bibliography

Abarca, E., Carrera, J., Sánchez-Vila, X., Dentz, M., 2007. Anisotropic dispersive Henry problem. Advances in Water Resources, 30(4): 913-926. DOI:10.1016/j.advwatres.2006.08.005

Abarca, E., Clement, T.P., 2009. A novel approach for characterizing the mixing zone of a saltwater wedge. Geophysical Research Letters, 36(6). DOI:10.1029/2008gl036995

Allen, D., Darling, W.G., Williams, P.J., Stratford, C.J., Robins, N.S., 2014. Understanding the hydrochemical evolution of a coastal dune system in SW England using a multiple tracer technique. Applied Geochemistry, 45: 94-104. DOI:10.1016/j.apgeochem.2013.12.014

Ataie-Ashtiani, B., Rajabi, M.M., Ketabchi, H., 2013. Inverse modelling for freshwater lens in small islands: Kish Island, Persian Gulf. Hydrological Processes, 27(19): 2759-2773. DOI:10.1002/hyp.9411

Ayers, J.F., Vacher, H.L., 1986. Hydrogeology of an Atoll Island: A Conceptual Model from Detailed Study of a Micronesian Example. Ground Water, 24(2): 185 - 198. DOI: DOI: 10.1111/j.1745-6584.1986.tb00994.x

Badon-Ghyben, W., 1888. Nota in Verband met de Voor- genomen Putboring Nabij Amsterdam (Notes on the probable results of well drilling near Amsterdam). Tijdschrift van het Koninklijk Instituut van Ingenieurs, The Hague: 8-22.

Bailey, R.T., Jenson, J.W., Olsen, A.E., 2009. Numerical Modeling of Atoll Island Hydrogeology. Ground Water, 47(2): 184-196.

Bailey, R.T., Jenson, J.W., Taboroši, D., 2012. Estimating the freshwater-lens thickness of atoll islands in the Federated States of Micronesia. Hydrogeology Journal, 21(2): 441-457. DOI:10.1007/s10040-012-0923-6

Barrett, B., Heinson, G., Hatch, M., Telfer, A., 2002. Geophysical methods in saline groundwater studies: locating perched water tables and fresh-water lenses. Exploration Geophysics, 33(2): 115-121. DOI:doi:10.1071/EG02115

Bear, J., 1972. Dynamics of Fluids in Porous Media. Courier Dover Publications, New York, 764 pp.

Bear, J., Cheng, A.-H., Sorek, S., Ouazar, D., Herrera, I., 2010. Seawater Intrusion in Coastal Aquifers Concepts, Methods and Practices. Springer, Berlin, 640 pp.

Beinhorn, M., Dietrich, P., Kolditz, O., 2005. 3-D numerical evaluation of density effects on tracer tests. Journal of Contaminant Hydrology. Journal of Contaminant Hydrology, 81(1-4): 89–105. DOI:10.1016/j.jconhyd.2005.08.001

Bethke, C.M., Johnson, T.M., 2008. Groundwater Age and Groundwater Age Dating. Annual Review of Earth and Planetary Sciences, 36(1): 121-152. DOI:10.1146/annurev.earth.36.031207.124210

Beyer, W., Schweiger, K.H., 1969. Zur Bestimmung des entwässerbaren Porenanteils der Grundwasserleiter. Wasserwirtschaft-Wassertechnik, 19(3): 57–60.

Bialas, Z., Kleczkowski, A.S., 1970. O przydatności niektórych wzorów empirycznych dla określenia współczynnika filtracji k (Empirical suitability of some of the designs for the determination of the coefficient of permeability K). Archiwum Hydrotechniki, 17: 405-417.

Bilke, L., Fischer, T., Helbig, C., Krawczyk, C., Nagel, T., Naumov, D., Paulick, S., Rink, K., Sachse, A., Schelenz, S., Walther, M., Watanabe, N., Zehner, B., Ziesch, J., Kolditz, O., 2014. TESSIN VISLab—laboratory for scientific visualization. Environmental Earth Sciences, 72(10): 3881-3899. DOI:10.1007/s12665-014-3785-5

Budd, D.A., Vacher, H.L., 1991. Predicting the thickness of fresh-water lenses in carbonate paleo-islands. J Sediment Petrol, 61: 43-53.

Buès, M.A., Oltean, C., 2000. Numerical Simulations for Saltwater Intrusion by the Mixed Hybrid Finite Element Method and Discontinuous Finite Element Method. Transport in Porous Media, 40(2): 171-200. DOI:10.1023/a:1006626230029

Chang, S.W., Clement, T.P., 2013. Laboratory and numerical investigation of transport processes occurring above and within a saltwater wedge. J Contam Hydrol, 147: 14-24. DOI:10.1016/j.jconhyd.2013.02.005

Chesnaux, R., Allen, D.M., 2008. Groundwater travel times for unconfined island aquifers bounded by freshwater or seawater. Hydrogeology Journal, 16(3): 437-445. DOI:http://dx.doi.org/10.1007/s10040-007-0241-6

Comte, J.-C., Banton, O., Join, J.-L., Cabioch, G., 2010. Evaluation of effective groundwater recharge of freshwater lens in small islands by the combined modeling of geoelectrical data and water heads. Water Resources Research, 46(6): n/a-n/a. DOI:10.1029/2009wr008058

Cooper, H.H., 1959. A hypothesis concerning the dynamic balance of fresh water and salt water in a coastal aquifer. J. Geophys. Res. , 64(4): 461-467.

Cooper, H.H., Kohout, F.A., Henry, H.R., Glover, R.E., 1964. Seawater in coastal aquifers U.S. Geol. Surv. Water-Supply Pap. 1613-C., 84 pp.

Cremer, C.J.M., Graf, T., 2015. Generation of dense plume fingers in saturated–unsaturated homogeneous porous media. Journal of Contaminant Hydrology, 173(0): 69-82. DOI:http://dx.doi.org/10.1016/j.jconhyd.2014.11.008

Crocombe, R., 2008. A World of Islands: An Island Studies Reader - Edited by Godfrey Baldacchino. Geographical Journal, 174(4): 389-390. DOI:10.1111/j.1475-4959.2008.309_2.x

Crossland, C.J., Kremer, H.H., Lindeboom, H., Crossland, J.I.M., Tissier, M.D.A.L., 2005. Coastal Fluxes in the Anthropocene. The Land-Ocean Interactions in the Coastal Zone Project of the International Geosphere-Biosphere Programme. Springer, Berlin, Heidelberg, 232 pp.

Cupola, F., Tanda, M.G., Zanini, A., 2015. Laboratory Estimation of Dispersivity Coefficients. Procedia Environmental Sciences, 25: 74-81. DOI:http://dx.doi.org/10.1016/j.proenv.2015.04.011

Custodio, E., 2010. Coastal aquifers of Europe: an overview. Hydrogeology Journal, 18(1): 269-280. DOI:10.1007/s10040-009-0496-1

Dagan, G., Bear, J., 1968. Solving The Problem Of Local Interface Upconing In A Coastal Aquifer By The Method Of Small Perturbations. Journal of Hydraulic Research, 6(1): 15-44. DOI:10.1080/00221686809500218

Diersch, H.-J.G., 2005. FEFLOW: Finite element subsurface flow and transport simulation system., Berlin, 292 pp.

Diersch, H.J.G., Kolditz, O., 2002. Variable-density flow and transport in porous media: approaches and challenges. Advances in Water Resources, 25(8): 899-944. DOI:10.1016/s0309-1708(02)00063-5

Diersch, H.J.G., 2014. Feflow: finite element modeling of flow, mass and heat transport in porous and fractured media. Springer Verlag Berlin Heidelberg, 996 pp.

Doherty, J., Brebber, L., Whyte, P., 1994. PEST: model-independent parameter estimation. Watermark Computing Trademarks, Australia.

Dose, E.J., Stoeckl, L., Houben, G.J., Vacher, H.L., Vassolo, S., Dietrich, J., Himmelsbach, T., 2014. Experiments and modeling of freshwater lenses in layered aquifers: Steady state interface geometry. Journal of Hydrology, 509: 621-630. DOI:10.1016/j.jhydrol.2013.10.010

Elder, J.W., 1967. Steady free convection in a porous medium heated from below. Journal of Fluid Mechanics, 27(01): 29-48. DOI:10.1017/s0022112067000023

Fahs, M., Younes, A., Mara, T.A., 2014. A new benchmark semi-analytical solution for density-driven flow in porous media. Advances in Water Resources, 70(0): 24-35. DOI:http://dx.doi.org/10.1016/j.advwatres.2014.04.013

Fein, E., Schneider, A., 1999. d³f – Ein Programmpaket zur Modellierung von Dichteströmungen. FKZ-02 C 0465 379, final report. Gesellschaft für Anlagen- und Reaktorsicherheit (GRS) mbH, GRS-139, Braunschweig.

Fetter, C.W., 1972. Position of the saline water interface beneath oceanic islands. Water Resources Research, 8(5): 1307-1315.

Fischer, T., Naumov, D., Sattler, S., Kolditz, O., Walther, M., 2015. GO2OGS 1.0: a versatile workflow to integrate complex geological information with fault data

into numerical simulation models. Geosci. Model Dev., 8(11): 3681-3694. DOI:10.5194/gmd-8-3681-2015

Flügge, C., Stockmann, M., Schneider, A., Noseck, U, 2013. The impact of climate transitions on the radionuclide transport through a sedimentary aquifer. In: Flügge, C., Adams, S., Dennis, I., Riemann, K. (Ed.), Assessing and Managing Groundwater in Different Environments. International Association of Hydrogeologists selected papers. CRC Press, Taylor and Francis Group, London, UK.

Goswami, R.R., Clement, T.P., 2007. Laboratory-scale investigation of saltwater intrusion dynamics. Water Resour. Res., 43(4): W04418.

Graf, T., Boufadel, M.C., 2011. Effect of viscosity, capillarity and grid spacing on thermal variable-density flow. Journal of Hydrology, 400(1–2): 41-57. DOI:http://dx.doi.org/10.1016/j.jhydrol.2011.01.025

Graf, T., Degener, L., 2011. Grid convergence of variable-density flow simulations in discretely-fractured porous media. Advances in Water Resources, 34(6): 760-769. DOI:http://dx.doi.org/10.1016/j.advwatres.2011.04.002

Greskowiak, J., Roper, T., Post, V.E., 2013. Closed-form approximations for two-dimensional groundwater age patterns in a fresh water lens. Ground Water, 51(4): 629-34. DOI:10.1111/j.1745-6584.2012.00996.x

Guevara Morel, C.R., Graf, T., submitted. Benchmarking variable-density flow in saturated and unsaturated porous media. For submission to Journal of Contaminant Hydrology.

Gupta, A.D., Gaikwad, V.P., 1987. Interface Upconing Due to a Horizontal Well in Unconfined Aquifer. Ground Water, 25(4): 466-474. DOI:10.1111/j.1745-6584.1987.tb02151.x

Hazen, A., 1892. Some physical properties of sands and gravels, with special reference to their use in filtration. Massachusetts State Board of Health, 24th Annual Report, 34: 539-556.

Henderson, A., 2007. ParaView Guide, A Parallel Visualization Application. Kitware Inc., New York.

Henry, H.R., 1964a. Interfaces between salt water and fresh water in coastal aquifers. U.S. Geol. Surv. Water Supply Pap., 1613-C: 35-69.

Henry, H.R., 1964b. Effects of dispersion on salt encroachment in coastal aquifer. U.S. Geol. Surv. Water Supply Pap., 1613-C: C71-C84.

Herzberg, A., 1901. Die Wasserversorgung einiger Nordseebäder. Journal Gasbeleuchtung und Wasserversorgung, 44: 815-819; München.

Hodgkinson, J., Cox, M.E., McLoughlin, S., 2007. Groundwater mixing in a sand-island freshwater lens: density-dependent flow and stratigraphic controls. Australian Journal of Earth Sciences, 54(7): 927-946. DOI:10.1080/08120090701488263

Holding, S., Allen, D.M., 2015a. Wave overwash impact on small islands: Generalised observations of freshwater lens response and recovery for multiple hydrogeological settings. Journal of Hydrology. DOI:http://dx.doi.org/10.1016/j.jhydrol.2015.08.052

Holding, S., Allen, D.M., 2015b. From days to decades: numerical modelling of freshwater lens response to climate change stressors on small low-lying islands. Hydrol. Earth Syst. Sci., 19(2): 933-949. DOI:10.5194/hess-19-933-2015

Houben, G., Koeniger, P., Sültenfuß, J., 2014a. Freshwater lenses as archive of climate, groundwater recharge, and hydrochemical evolution: Insights from depth-specific water isotope analysis and age determination on the island of Langeoog, Germany. Water Resources Research, 50(10): 8227-8239. DOI:10.1002/2014wr015584

Houben, G., Noell, U., Vassolo, S., Grissemann, C., Geyh, M., Stadler, S., Dose, E., Vera, S., 2014b. The freshwater lens of Benjamín Aceval, Chaco, Paraguay: a terrestrial analogue of an oceanic island lens. Hydrogeology Journal, 22(8): 1935-1952. DOI:10.1007/s10040-014-1169-2

Houben, G.J., Hauschild, S., 2011. Numerical Modeling of the Near-Field Hydraulics of Water Wells. Ground Water, 49(4): 570-575. DOI:10.1111/j.1745-6584.2010.00760.x

Igel, J., Günther, T., Kuntzer, M., 2013. Ground-penetrating radar insight into a coastal aquifer: the freshwater lens of Borkum Island. Hydrology and Earth System Sciences, 17(2): 519-531. DOI:10.5194/hess-17-519-2013

Jakovovic, D., Werner, A.D., Simmons, C.T., 2011. Numerical modelling of saltwater up-coning: Comparison with experimental laboratory observations. Journal of Hydrology, 402(3-4): 261-273. DOI:10.1016/j.jhydrol.2011.03.021

Johannsen, K., Kinzelbach, W., Oswald, S., Wittum, G., 2002. The saltpool benchmark problem - numerical simulation of saltwater upconing in a porous medium. Advances in Water Resources, 25(3): 335-348.

Ketabchi, H., Mahmoodzadeh, D., Ataie-Ashtiani, B., Werner, A.D., Simmons, C.T., 2014. Sea-level rise impact on fresh groundwater lenses in two-layer small islands. Hydrological Processes, 28(24): 5938-5953. DOI:10.1002/hyp.10059

Kinzelbach, W., Rausch, R., 1995. Grundwassermodellierung: Eine Einführung mit Übungen. Borntraeger Berlin, Stuttgart, 283 pp.

Kolditz, O., Görke, U.-J., Shao, H., Wang, W., Bauer, S., 2015. Thermo-Hydro-Mechanical-Chemical Processes in Fractured Porous Media: Modelling and Benchmarking. Springer International Publishing Switzerland.

König, C., Becker, M., Diehl, A., Rosen, B., Rüber, O., Seidel, T., Werth, B., Zimmermann, C., 2012. SPRING Benutzerhandbuch, Ausgabe 4.1. delta h Ingenieurgesellschaft mbH; Witten, Germany., 605 pp.

Kuan, W.K., Jin, G., Xin, P., Robinson, C., Gibbes, B., Li, L., 2012. Tidal influence on seawater intrusion in unconfined coastal aquifers. Water Resources Research, 48(2): n/a-n/a. DOI:10.1029/2011wr010678

Lemieux, J.-M., Hassaoui, J., Molson, J., Therrien, R., Therrien, P., Chouteau, M., Ouellet, M., 2015. Simulating the impact of climate change on the groundwater resources of the Magdalen Islands, Québec, Canada. Journal of Hydrology: Regional Studies, 3(0): 400-423. DOI:http://dx.doi.org/10.1016/j.ejrh.2015.02.011

Luyun, R., Jr., Momii, K., Nakagawa, K., 2011. Effects of recharge wells and flow barriers on seawater intrusion. Ground Water, 49(2): 239-49. DOI:10.1111/j.1745-6584.2010.00719.x

Maas, K., 2007. Influence of climate change on a Ghijben–Herzberg lens. Journal of Hydrology, 347(1-2): 223-228. DOI:10.1016/j.jhydrol.2007.09.020

Macdonald, G.A., Abbott, A.T., Peterson, F.L., 1990. Volcanoes in the Sea - The geology of Hawaii, 2nd edition. University of Hawaii Press, Honolulu, 517 pp.

Mahmoodzadeh, D., Ketabchi, H., Ataie-Ashtiani, B., Simmons, C.T., 2014. Conceptualization of a fresh groundwater lens influenced by climate change: A modeling study of an arid-region island in the Persian Gulf, Iran. Journal of Hydrology, 519, Part A(0): 399-413. DOI:http://dx.doi.org/10.1016/j.jhydrol.2014.07.010

Maxwell, R.M., Putti, M., Meyerhoff, S., Delfs, J.-O., Ferguson, I.M., Ivanov, V., Kim, J., Kolditz, O., Kollet, S.J., Kumar, M., Lopez, S., Niu, J., Paniconi, C., Park, Y.-J., Phanikumar, M.S., Shen, C., Sudicky, E.A., Sulis, M., 2014. Surface-subsurface model intercomparison: A first set of benchmark results to diagnose integrated hydrology and feedbacks. Water Resources Research, 50(2): 1531-1549. DOI:10.1002/2013wr013725

Mehdizadeh, S.S., Werner, A.D., Vafaie, F., Badaruddin, S., 2014. Vertical leakage in sharp-interface seawater intrusion models of layered coastal aquifers. Journal of Hydrology, 519, Part A: 1097-1107. DOI:http://dx.doi.org/10.1016/j.jhydrol.2014.08.027

Michael, H.A., Mulligan, A.E., Harvey, C.F., 2005. Seasonal oscillations in water exchange between aquifers and the coastal ocean. Nature, 436(7054): 1145-1148.

Miller, C.T., Gray, W.G., 2002. Hydrogeological Research: Just Getting Started. Ground Water, 40(3): 224-231. DOI:10.1111/j.1745-6584.2002.tb02650.x

Mondal, N.C., Singh, V.S., Saxena, V.K., Prasad, R.K., 2008. Improvement of groundwater quality due to fresh water ingress in Potharlanka Island, Krishna

delta, India. Environmental Geology, 55(3): 595-603. DOI:10.1007/s00254-007-1010-5

Morgan, L.K., Stoeckl, L., Werner, A.D., Post, V.E.A., 2013. An assessment of seawater intrusion overshoot using physical and numerical modeling. Water Resources Research, 49(10): 6522-6526. DOI:10.1002/wrcr.20526

Morgan, L.K., Werner, A.D., 2014. Seawater intrusion vulnerability indicators for freshwater lenses in strip islands. Journal of Hydrology, 508: 322-327. DOI:10.1016/j.jhydrol.2013.11.002

Nash, J.E., Sutcliffe, J.V., 1970. River flow forecasting through conceptual models part I — A discussion of principles. Journal of Hydrology, 10(3): 282-290.

Naumann, K., 2005. Eine hydrogeologische Systemanalyse von Süßwasserlinsen als Grundlage einer umweltschonenden Grundwasserbewirtschaftung. Dissertation Thesis, Technische Universität Carolo-Wilhelmina zu Braunschweig, 132 pp.

Oswald, S., 1998. Dichteströmungen in porösen Medien: Dreidimensionale Experimente und Modellierung. Ph.D. Thesis, ETH Zürich.

Oswald, S., Kinzelbach, W., 2004. Three-dimensional physical benchmark experiments to test variable-density flow models. Journal of Hydrology, 290(1–2): 22-42. DOI:http://dx.doi.org/10.1016/j.jhydrol.2003.11.037

Oude Essink, G.H.P., 1996. Impacts of sea level rise on groundwater flow regimes; a sensitivity analysis for the Netherlands, PhD Thesis Technical Univ. Delft, Netherlands, 411 pp.

Oude Essink, G.H.P., van Baaren, E.S., de Louw, P.G.B., 2010. Effects of climate change on coastal groundwater systems: A modeling study in the Netherlands. Water Resources Research, 46(10): n/a-n/a. DOI:10.1029/2009wr008719

Pennink, J.M.K., 1915. Grondwater Stroombanen. Stadsdrukkery Amsterdam. http://citg.tudelft.nl/index.php?id=19739&L=1.

Post, V.E.A., Vandenbohede, A., Werner, A.D., Maimun, Teubner, M.D., 2013. Groundwater ages in coastal aquifers. Advances in Water Resources, 57: 1-11. DOI:10.1016/j.advwatres.2013.03.011

Rausch, R., Schäfer, W., Therrien, R., Wagner, C., 2005. Solute transport modelling - an introduction to models and solution strategies. Borntraeger Berlin, Stuttgart.

Reilly, T.E., Goodman, A.S., 1985. Quantitative analysis of saltwater-freshwater relationships in groundwater systems--A historical perspective. Journal of Hydrology, 80(1-2): 125-160.

Robins, N.S., 2013. A review of small island hydrogeology: progress (and setbacks) during the recent past. Quarterly Journal of Engineering Geology and Hydrogeology, 46(2): 157-165. DOI:10.1144/qjegh2012-063

Robinson, G., Hamill, G.A., Ahmed, A.A., 2015. Automated image analysis for experimental investigations of salt water intrusion in coastal aquifers. Journal of Hydrology, 530: 350-360. DOI:http://dx.doi.org/10.1016/j.jhydrol.2015.09.046

Rolle, M., Eberhardt, C., Chiogna, G., Cirpka, O.A., Grathwohl, P., 2009. Enhancement of dilution and transverse reactive mixing in porous media: Experiments and model-based interpretation. Journal of Contaminant Hydrology, 110(3–4): 130-142. DOI:http://dx.doi.org/10.1016/j.jconhyd.2009.10.003

Röper, T., Kröger, K.F., Meyer, H., Sültenfuss, J., Greskowiak, J., Massmann, G., 2012. Groundwater ages, recharge conditions and hydrochemical evolution of a barrier island freshwater lens (Spiekeroog, Northern Germany). Journal of Hydrology, 454-455: 173-186. DOI:10.1016/j.jhydrol.2012.06.011

Röper, T., Greskowiak, J., Freund, H., Massmann, G., 2013. Freshwater lens formation below juvenile dunes on a barrier island (Spiekeroog, Northwest Germany). Estuarine, Coastal and Shelf Science, 121-122: 40-50. DOI:10.1016/j.ecss.2013.02.004

Rozell, D., Wong, T.-f., 2010. Effects of climate change on groundwater resources at Shelter Island, New York State, USA. Hydrogeology Journal, 18(7): 1657-1665. DOI:10.1007/s10040-010-0615-z

Sanford, W., 2011. Calibration of models using groundwater age. Hydrogeology Journal, 19(1): 13-16. DOI:10.1007/s10040-010-0637-6

Scanlon, B., Healy, R., Cook, P., 2002. Choosing appropriate techniques for quantifying groundwater recharge. Hydrogeology Journal, 10(1): 18-39. DOI:10.1007/s10040-001-0176-2

Scheidegger, A.E., 1961. General theory of dispersion in porous media. Journal of Geophysical Research, 66(10): 3273-3278. DOI:10.1029/JZ066i010p03273

Schincariol, R.A., Schwartz, F.W., 1990. An experimental investigation of variable density flow and mixing in homogeneous and heterogeneous media. Water Resources Research, 26(10): 2317-2329. DOI:10.1029/WR026i010p02317

Schincariol, R.A., Schwartz, F.W., Mendoza, C.A., 1994. On the generation of instabilities in variable density flow. Water Resources Research, 30(4): 913-927. DOI:10.1029/93wr02951

Schmork, S., Mercado, A., 1969. Upconing of Fresh Water—Sea Water Interface Below Pumping Wells, Field Study. Water Resources Research, 5(6): 1290-1311. DOI:10.1029/WR005i006p01290

Schneider, J.C., Kruse, S.E., 2003. A comparison of controls on freshwater lens morphology of small carbonate and siliciclastic islands: examples from barrier islands in Florida, USA. Journal of Hydrology, 284(1-4): 253-269. DOI:10.1016/j.jhydrol.2003.08.002

Schneider, J.C., Kruse, S.E., 2005. Assessing selected natural and anthropogenic impacts on freshwater lens morphology on small barrier Islands: Dog Island and St. George Island, Florida, USA. Hydrogeology Journal, 14(1-2): 131-145. DOI:10.1007/s10040-005-0442-9

Seelheim, F., 1980. Methoden zur Bestimmung der Durchlässigkeit des Bodens (Methods to determine the conductivity of soil). Fresenius J. Anal. Chem., 19(1): 387–418.

Segol, G., 1994. Classic groundwater simulations: proving and improving numerical models. Prentice Hall Inc., Englewood Cliffs, New Jersey.

Shankar, V., Eckert, P., Ojha, C., König, C., 2009. Transient 3-D Modeling of Riverbank Filtration at Grind Well Field. Hydrogeology Journal, 17: 321-326.

Shewchuk, J., 1996. Triangle: Engineering a 2D quality mesh generator and Delaunay triangulator. In: Lin, M., Manocha, D. (Eds.), Applied Computational Geometry Towards Geometric Engineering. Lecture Notes in Computer Science. Springer Berlin Heidelberg, pp. 203-222. DOI:10.1007/BFb0014497

Siemon, B., Christiansen, A.V., Auken, E., 2009. A review of helicopter-borne electromagnetic methods for groundwater exploration. Near Surface Geophysics, 7: 629-646.

Simmons, C.T., Narayan, K.A., Wooding, R.A., 1999. On a test case for density-dependent groundwater flow and solute transport models: The Salt Lake Problem. Water Resources Research, 35(12): 3607-3620. DOI:10.1029/1999wr900254

Simmons, C.T., Pierini, M.L., Hutson, J.L., 2002. Laboratory Investigation of Variable-Density Flow and Solute Transport in Unsaturated–Saturated Porous Media. Transport in Porous Media, 47(2): 215-244. DOI:10.1023/a:1015568724369

Simmons, C.T., 2005. Variable density groundwater flow: From current challenges to future possibilities. Hydrogeology Journal, 13(1): 116-119. DOI:10.1007/s10040-004-0408-3

Simpson, M.J., Clement, T.P., 2003. Theoretical analysis of the worthiness of Henry and Elder problems as benchmarks of density-dependent groundwater flow models. Advances in Water Resources, 26(1): 17-31. DOI:10.1016/s0309-1708(02)00085-4

Simpson, M.J., Clement, T.P., 2004. Improving the worthiness of the Henry problem as a benchmark for density-dependent groundwater flow models. Water Resources Research, 40(1): W01504. DOI:10.1029/2003wr002199

Stoeckl, L., Houben, G., 2012. Flow dynamics and age stratification of freshwater lenses: Experiments and modeling. Journal of Hydrology, 458–459(0): 9-15. DOI:http://dx.doi.org/10.1016/j.jhydrol.2012.05.070graf

Stoeckl, L., Houben, G.J., Dose, E.J., 2015. Experiments and modeling of flow processes in freshwater lenses in layered island aquifers: Analysis of age stratification, travel

times and interface propagation. Journal of Hydrology, 529, Part 1: 159-168. DOI:http://dx.doi.org/10.1016/j.jhydrol.2015.07.019

Stoeckl, L., Walther, M., Graf, T., 2016. A new numerical benchmark of a freshwater lens. Water Resources Research, 52(4): 2474–2489. DOI:10.1002/2015WR017989

Strack, O.D.L., Ausk, B.K., 2015. A formulation for vertically integrated groundwater flow in a stratified coastal aquifer. Water Resources Research, 51(8): 6756-6775. DOI:10.1002/2015wr016887

Stuyfzand, P.J., 1993. Hydrochemistry and hydrology of the costal dune area of the Western Netherlands, Ph.D Thesis Vrije Univ. Amsterdam, published by KIWA, 366 pp.

Stuyfzand, P.J., Bruggeman, G.A., 1994. Analytical approximations for fresh water lenses in coastal dunes. In: Barrocu, G. (Ed.), Proc. 13th Salt Water Intrusion Meeting. Univ. Cagliari, Fac. Engineering, Cagliari Italy, pp. 15-33.

Sulzbacher, H., Wiederhold, H., Siemon, B., Grinat, M., Igel, J., Burschil, T., Günther, T., Hinsby, K., 2012. Numerical modelling of climate change impacts on freshwater lenses on the North Sea Island of Borkum using hydrological and geophysical methods. Hydrology and Earth System Sciences, 16(10): 3621-3643. DOI:10.5194/hess-16-3621-2012

Terry, J., Falkland, A., 2010. Responses of atoll freshwater lenses to storm-surge overwash in the Northern Cook Islands. Hydrogeology Journal, 18(3): 749-759. DOI:10.1007/s10040-009-0544-x

Therrien, R., McLaren, R.G. and Sudicky, E.A. (2007), 2007. HydroGeoSphere - a three-dimensional numerical model describing fully integrated subsurface and surface flow and solute transport (Draft ed.). Groundwater Simulations Group, University of Waterloo. http://www.science.uwaterloo.ca/~mclaren/public/hydrosphere.pdf.

Thorenz, C., Kosakowski, G., Kolditz, O., Berkowitz, B., 2002. An experimental and numerical investigation of saltwater movement in coupled saturated–partially saturated systems. Water Resources Research, 38(6): 5-1-5-11. DOI:10.1029/2001wr000364

Tronicke, J., Blindow, N., Groß, R., Lange, M.A., 1999. Joint application of surface electrical resistivity- and GPR-measurements for groundwater exploration on the island of Spiekeroog—northern Germany. Journal of Hydrology, 223(1–2): 44-53. DOI:http://dx.doi.org/10.1016/S0022-1694(99)00111-0

Underwood, M.R., Peterson, F.L., Voss, C.I., 1992. Groundwater lens dynamics of Atoll Islands. Water Resources Research, 28(11): 2889-2902. DOI:10.1029/92wr01723

Vacher, H.L., 1978. Hydrogeology of Bermuda - Significance of an across-the-island variation in permeability. Journal of Hydrology, 39(3-4): 207-226.

Vacher, H.L., Ayers, J.F., 1980. Hydrology of small oceanic islands -- Utility of an estimate of recharge inferred from the chloride concentration of the freshwater lenses. Journal of Hydrology, 45(1-2): 21-37.

Vacher, H.L., 1988. Dupuit-Ghyben-Herzberg analysis of strip-island lenses. Geological Society of America Bulletin, 100(4): 580-591. DOI:10.1130/0016-7606(1988)100<0580:dghaos>2.3.co;2

Vacher, H.L., Bengtsson, T.O., Plummer, L.N., 1990. Hydrology of meteoric diagenesis: Residence time of meteoric ground water in island fresh-water lenses with application to aragonite-calcite stabilization rate in Bermuda. Geological Society of America Bulletin, 102(2): 223-232. DOI:10.1130/0016-7606(1990)102<0223:homdrt>2.3.co;2

Vacher, H.L., Wallis, T.N., 1992. Comparative hydrogeology of Bermuda and Great Exuma Island, Bahamas. Ground Water, 30: 15-20.

van der Veer, P., 1977. Analytical solution for a two-fluid flow in a coastal aquifer involving a phreatic surface with precipitation. Journal of Hydrology, 35(3): 271-278. DOI:http://dx.doi.org/10.1016/0022-1694(77)90006-3

van Ginkel, M., 2015. Aquifer design for freshwater storage and recovery in artificial islands and coastal expansions. Hydrogeology Journal, 23(4): 615-618. DOI:10.1007/s10040-015-1245-2

Vandenbohede, Lebbe, 2002. Numerical modelling and hydrochemical characterisation of a fresh-water lens in the Belgian coastal plain. Hydrogeology Journal, 10(5): 576-586.

Vogel, J.C., 1967. Investigation of groundwater flow with radiocarbon, Proc. symp. Isotopes Hydrol. IAEA, Vienna, pp. 355-369.

Vogel, J.C., 1970. Carbon-14 dating of groundwater, Proc. symp. Isotopes Hydrol. IAEA, Vienna, pp. 255-239.

Voss, C.I., Souza, W.R., 1987. Variable density flow and solute transport simulation of regional aquifers containing a narrow freshwater-saltwater transition zone. Water Resources Research, 23(10): 1851-1866. DOI:10.1029/WR023i010p01851

Voss, C.I., Wood, W.W., 1994. Synthesis of geochemical, isotopic and groundwater modeling analysis to explain regional flow in a coastal aquifer of southern Oahu, Hawaii. In: Mathematical models and their applications to isotope studies in groundwater hydrology, international atomic energy agency (IAEA), Vienna, Austria.

Voss, C.I., Simmons, C.T., Robinson, N., 2010. Three-dimensional benchmark for variable-density flow and transport simulation: matching semi-analytic stability modes for steady unstable convection in an inclined porous box. Hydrogeology Journal, 18(1): 5-23. DOI:10.1007/s10040-009-0556-6

Wallis, T.N., Vacher, H.L., TStewart, M.T., 1991. Hydrogeology of freshwater lens beneath a Holocene strandplain, Great Exuma, Bahamas. Journal of Hydrology, 125: 93-109.

Walther M., L.B., J.-O. Delfs, T. Graf, J. Grundmann, O. Kolditz, R. Liedl, 2014. Assessing the saltwater remediation potential of a three-dimensional, heterogeneous, coastal aquifer system. Model verification, application and visualization for transient density-driven seawater intrusion. Environmental Earth Science., 72: 3827-3837. DOI:DOI: 10.1007/s12665-014-3253-2

Weatherill, D., Simmons, C.T., Voss, C.I., Robinson, N.I., 2004. Testing density-dependent groundwater models: two-dimensional steady state unstable convection in infinite, finite and inclined porous layers. Advances in Water Resources, 27(5): 547-562. DOI:http://dx.doi.org/10.1016/j.advwatres.2004.01.003

Werner, A.D., Jakovovic, D., Simmons, C.T., 2009. Experimental observations of saltwater up-coning. Journal of Hydrology, 373(1-2): 230-241.

Werner, A.D., Bakker, M., Post, V.E.A., Vandenbohede, A., Lu, C., Ataie-Ashtiani, B., Simmons, C.T., Barry, D.A., 2013. Seawater intrusion processes, investigation and management: Recent advances and future challenges. Advances in Water Resources, 51(0): 3-26. DOI:http://dx.doi.org/10.1016/j.advwatres.2012.03.004

White, I., Falkland, T., Perez, P., Dray, A., Metutera, T., Metai, E., Overmars, M., 2007. Challenges in freshwater management in low coral atolls. Journal of Cleaner Production, 15(16): 1522-1528. DOI:http://dx.doi.org/10.1016/j.jclepro.2006.07.051

White, I., Falkland, T., 2009. Management of freshwater lenses on small Pacific islands. Hydrogeology Journal, 18(1): 227-246. DOI:10.1007/s10040-009-0525-0

Wooding, R.A., Tyler, S.W., White, I., 1997a. Convection in groundwater below an evaporating Salt Lake: 1. Onset of instability. Water Resources Research, 33(6): 1199-1217. DOI:10.1029/96wr03533

Wooding, R.A., Tyler, S.W., White, I., Anderson, P.A., 1997b. Convection in groundwater below an evaporating Salt Lake: 2. Evolution of fingers or plumes. Water Resources Research, 33(6): 1219-1228. DOI:10.1029/96wr03534

Xie, Y., Graf, T., Simmons, C.T., Diersch, H.J.G., 2014. The Effect of Porous Medium Storage on Unstable Density-Driven Solute Transport. Ground Water, 13: 806-809. DOI:doi: 10.1111/gwat.12285

Yang, J., Graf, T., Herold, M., Ptak, T., 2013. Modelling the effects of tides and storm surges on coastal aquifers using a coupled surface-subsurface approach. J Contam Hydrol, 149: 61-75. DOI:10.1016/j.jconhyd.2013.03.002

Zhang, Q., Volker, R.E., Lockington, D.A., 2002. Experimental investigation of contaminant transport in coastal groundwater. Advances in Environmental Research, 6(3): 229-237. DOI:http://dx.doi.org/10.1016/S1093-0191(01)00054-5

Zhou, Q., Bear, J., Bensabat, J., 2005. Saltwater Upconing and Decay Beneath a Well Pumping Above an Interface Zone. Transport in Porous Media, 61(3): 337-363. DOI:10.1007/s11242-005-0261-4

Zuber, A., Różański, K., Kania, J., Purtschert, R., 2011. On some methodological problems in the use of environmental tracers to estimate hydrogeologic parameters and to calibrate flow and transport models. Hydrogeology Journal, 19(1): 53-69. DOI:10.1007/s10040-010-0655-4

Lebenslauf

Leonard Stöckl

geboren am 19.07.1982

in Hamburg

03/ 2011 bis heute	Wissenschaftlicher Angestellter im Fachbereich B2.3 Grundwasserressourcen – Beschaffenheit und Dynamik an der Bundesanstalt für Geowissenschaften und Rohstoffe (BGR)
10/ 2013 – 05/ 2016	Promotionsstudent am Institut für Strömungsmechanik und Umweltphysik im Bauwesen der Gottfried Wilhelm Leibniz Universität Hannover
08/ 2010 – 02/ 2011	Wissenschaftlicher Assistent an der Albert-Ludwigs-Universität Freiburg, Institut für Hydrologie im DFG-Projekt „Rain on Snow"
03/ 2009 – 08/ 2009	Junior-Hydrogeologe bei Bittner Water Consult (BIWAC), Windhuk, Namibia
12/ 2006 – 10/ 2008	Studentische Hilfskraft am Institut für Bodenkunde und Waldernährungslehre der Albert-Ludwigs-Universität Freiburg
10/ 2004 – 07/ 2010	Student der Hydrologie an der Albert-Ludwigs-Universität Freiburg; Vertiefungsrichtung: Meteorologie, Geologie und Bodenkunde
10/ 2003 – 10/ 2004	Student der Geologie an der Georg-August-Universität Göttingen
10/ 2002 – 08/ 2003	Zivildienstleistender beim Turn- und Sportverein (TSG) Bergedorf, Hamburg
06/ 2002	Abitur am Hansa-Gymnasium Bergedorf, Hamburg